

WANL-TNR-192

December 31, 1964



**Westinghouse
Astronuclear Laboratory**

INFORMATION CATEGORY

UNCLASSIFIED

Prepared By:

R. N. Pinchok

R. N. Pinchok

J. M. Bridges

J. M. Bridges

Approved By:

John E. Faulkner

**J. E. Faulkner,
Manager
Safeguards
Engineering**

Edna H. Hemmle 1/25/65
Authorized Classifier Date

**An Experimental Investigation
Of The Re-Entry Behavior
Of Metals And Alloys**

TABLE OF CONTENTS

	<u>Page</u>
<u>SUMMARY</u>	xi
1.0 <u>INTRODUCTION</u>	1
2.0 <u>BACKGROUND INFORMATION</u>	2
2.1 <u>Reactions of Metals and Alloys</u>	2
2.1.1 <u>Physical Changes</u>	2
2.1.2 <u>Chemical Changes</u>	4
2.1.2.1 <u>Theory</u>	4
2.1.2.2 <u>Summary of Oxidation Data</u>	7
2.1.2.2.1 <u>Aluminum</u>	7
2.1.2.2.2 <u>Titanium</u>	8
2.1.2.2.3 <u>Stainless Steel</u>	9
2.1.2.2.4 <u>Inconel X</u>	9
2.1.2.2.5 <u>Nickel</u>	10
2.1.2.2.6 <u>Beryllium</u>	10
2.1.2.3 <u>Summary of Nitrification Data</u>	11
2.1.2.3.1 <u>Aluminum</u>	11
2.1.2.3.2 <u>Titanium</u>	11
2.1.2.3.3 <u>Stainless Steel</u>	12

TABLE OF CONTENTS (Continued)

	<u>Page</u>
2.1.2.3.4 <u>Inconel</u>	12
2.1.2.3.5 <u>Beryllium</u>	12
2.1.2.4 <u>Possible Influence of Oxides on Ablation Process</u>	12
2.2 <u>Re-Entry Heat Considerations</u>	13
2.2.1 <u>Glossary of Aerodynamic Symbols</u>	13
2.2.2 <u>Aerodynamic Heating - Stagnation Point</u>	15
2.2.2.1 <u>High Reynolds Number Heating</u>	15
2.2.2.2 <u>Low Reynolds Number Heating</u>	16
2.2.2.2.1 <u>Probstein and Kemp</u>	16
2.2.2.2.2 <u>Ferri, Zakkay, and Ting</u>	17
2.2.2.3 <u>Comparison of Theories</u>	17
2.2.3 <u>Average Aerodynamic Heating</u>	18
2.2.4 <u>Other Heat Transfer Considerations</u>	18
2.3 <u>Heat Balance for Ablation</u>	19
3.0 <u>AERODYNAMIC HEATING STUDIES</u>	21
3.1 <u>Experimental</u>	21
3.1.1 <u>Facility Description</u>	21
3.1.2 <u>Stagnation Pressure Measurements</u>	22
3.1.3 <u>Stagnation Enthalpy Measurements</u>	22

TABLE OF CONTENTS (Continued)

	<u>Page</u>
3.1.4 <u>Calorimetric Measurements</u>	23
3.1.4.1 <u>Stagnation Point Calorimeter</u>	23
3.1.4.2 <u>Average Heat Flux Calorimeter</u>	25
3.2 <u>Results</u>	26
3.3 <u>Comparison of Results with Theory</u>	26
4.0 <u>METALS ABLATION</u>	28
4.1 <u>Experimental</u>	28
4.1.1 <u>Apparatus</u>	28
4.1.2 <u>Stagnation Pressure Measurements</u>	28
4.1.3 <u>Stagnation Enthalpy Measurements</u>	28
4.1.4 <u>Sample Temperature Measurements</u>	28
4.1.5 <u>Materials</u>	28
4.1.6 <u>Procedure</u>	29
4.2 <u>Results</u>	30
4.2.1 <u>Titanium</u>	30
4.2.1.1 <u>Non-Ablative Phenomena</u>	30
4.2.1.1.1 <u>Steady State</u>	30
4.2.1.1.2 <u>Oxidation</u>	31

TABLE OF CONTENTS (Continued)

	<u>Page</u>
4.2.1.2 <u>Ablation</u>	31
4.2.1.3 <u>Effect of Oxide Coat on Ablation</u>	33
4.2.2 <u>Aluminum</u>	33
4.2.2.1 <u>Non-Ablative Phenomena</u>	33
4.2.2.1.1 <u>Steady State</u>	33
4.2.2.1.2 <u>Oxidation</u>	33
4.2.2.2 <u>Ablation</u>	34
4.2.3 <u>Aluminum Alloy</u>	36
4.2.3.1 <u>Non-Ablative Phenomena</u>	36
4.2.3.1.1 <u>Steady State</u>	36
4.2.3.1.2 <u>Oxidation</u>	36
4.2.3.2 <u>Ablation</u>	36
4.2.4 <u>Stainless Steel</u>	37
4.2.4.1 <u>Non-Ablative Phenomena</u>	37
4.2.4.1.1 <u>Steady State</u>	37
4.2.4.1.2 <u>Oxidation</u>	37
4.2.4.2 <u>Ablation</u>	37
4.2.4.3 <u>Incomplete Ablation</u>	38
4.2.4.4 <u>Experimental Examination of Incomplete Ablation</u>	39

TABLE OF CONTENTS (Continued)

	<u>Page</u>
4.2.4.4.1 <u>Effect of Oxide Coat on Ablation</u>	39
4.2.4.4.2 <u>Effect of Sample Geometry</u>	40
4.2.5 <u>Inconel X</u>	41
4.2.5.1 <u>Non-Ablative Phenomena</u>	41
4.2.5.1.1 <u>Steady State</u>	41
4.2.5.1.2 <u>Oxidation</u>	42
4.2.5.2 <u>Ablation</u>	42
4.2.5.3 <u>Incomplete Ablation</u>	42
4.2.5.4 <u>Experimental Examination of Incomplete Ablation</u>	43
4.2.5.4.1 <u>Effect of Oxide Coat on Ablation</u>	43
4.2.5.4.2 <u>Effect of Sample Geometry</u>	43
4.2.6 <u>Beryllium</u>	44
4.2.6.1 <u>Non-Ablative Phenomena</u>	44
4.2.6.1.1 <u>Steady State</u>	44
4.2.6.1.2 <u>Oxidation</u>	44
4.2.6.2 <u>Ablation</u>	45
5.0 <u>CONCLUSIONS</u>	48
<u>BIBLIOGRAPHY</u>	50
Appendix I <u>LIST OF TABLES</u>	I-1
Appendix II <u>LIST OF FIGURES</u>	II-1

LIST OF TABLES

<u>Number</u>	<u>Title</u>	<u>Page</u>
2.1	Sublimation Rate of Typical Solids at Their Melting Points	I-1
2.2	Thermodynamic Heat Data of Typical Solids	I-2
2.3	Some Thermal Properties of Oxides Formed During Re-entry	I-3
2.4	Emissivities of Typical Solids	I-4
3.1	Summary of Stagnation Point Heat Transfer Data (One-inch Calorimeter)	I-5
3.2	Summary of Total Heat Transfer Data (One-half inch Calorimeter)	I-6
4.1	Composition of Metals and Alloys	I-7
4.2	Summary of Titanium Test Points	I-8
4.3	Summary of Titanium Steady State Data	I-9
4.4	Summary of Titanium Oxidation Data	I-10
4.5	Summary of Titanium Ablation Data	I-11
4.6	Effect of Oxide Coat on Time for Complete Ablation of Titanium Samples	I-12
4.7	Summary of Aluminum Test Points	I-13
4.8	Summary of Aluminum Ablation Data	I-14
4.9	Summary of Aluminum Alloy Test Points	I-15
4.10	Summary of Aluminum Alloy Ablation Data	I-16
4.11	Summary of Stainless Steel Test Points	I-17
4.12	Summary of Stainless Steel Steady State Data	I-18
4.13	Summary of Stainless Steel Ablation Data	I-19
4.14	Summary of Stainless Steel Incomplete Ablation Data	I-20
4.15	Effect of Oxide Coat on Time for Complete Ablation of Stainless Steel Samples	I-21
4.16	Ablation of Stainless Steel Samples of Cylindrical Geometry vs Regular Hemispheres	I-22
4.17	Effects of Sample Position on Ablation of Stainless Steel Samples	I-23

List of Tables (Continued)

<u>Number</u>	<u>Title</u>	
4.18	Summary of Inconel Test Points	I-24
4.19	Summary of Inconel Steady State Data	I-25
4.20	Summary of Inconel Ablation Data	I-26
4.21	Summary of Inconel Incomplete Ablation Data	I-27
4.22	Effect of Oxide Coat on Time for Complete Ablation of Inconel Samples	I-28
4.23	Ablation of Inconel Samples of Cylindrical Shape vs Hemispherical Shape	I-29
4.24	Effects of Sample Position on Ablation of Inconel Samples	I-30
4.25	Summary of Beryllium Test Points	I-31
4.26	Summary of Beryllium Steady State Data	I-32
4.27	Summary of Beryllium Ablation Data	I-33
4.28	Summary of Beryllium Initial Melt Data	I-34

LIST OF FIGURES

<u>Number</u>	<u>Title</u>	<u>Page</u>
2.1	Theoretical Stanton Number as a Function of Reynolds Number	II-1
3.1	Stagnation Point Heat Flux Probe	II-2
3.2	Schematic Diagram of Stagnation Point Calorimeter Probe	II-3
3.3	Heat Flux as Function of Coolant Flow Rate	II-4
3.4	Experimental and Theoretical Stanton Numbers as Function of Reynolds Number	II-5
3.5	Average Heating Rate as a Function of Stagnation Heating Rate	II-6
4.1	Support for Model in a Plasmajet Facility	II-7
4.2	Steady State Temperature Profiles for Titanium Samples	II-8
4.3	Typical Linear Oxidation Plot for Titanium at 1000°C	II-9
4.4	Typical Parabolic Oxidation Plot for Titanium at 1500°C	II-10
4.5	Typical Parabolic Oxidation Plot for Titanium at 1600°C	II-11
4.6	Ablation Sequence of Titanium Samples	II-12
4.7	Frontal View - Tear Away Ablation Sequence of Aluminum Samples	II-13
4.8	Lateral View - Tear Away Ablation Sequence of Aluminum Samples	II-14
4.9	Particles from Tear Away Ablation of Aluminum Samples	II-15
4.10	Frontal View - Flowing Ablation Sequence of Aluminum Samples	II-16
4.11	Lateral View - Flowing Ablation Sequence of Aluminum Samples	II-17
4.12	Particles from Flowing Ablation of Aluminum Samples	II-18
4.13	Plot of Aluminum Ablation Data	II-19
4.14	Plot of Aluminum Alloy Ablation Data	II-20
4.15	Steady State Temperature Profiles for Stainless Steel Samples	II-21

LIST OF FIGURES (Continued)

<u>Number</u>	<u>Title</u>	<u>Page</u>
4.16	Typical Oxidation Plot for Stainless Steel at 1300°C	II-22
4.17	Typical Oxidation Plot for Stainless Steel at 1400°C	II-23
4.18	Frontal View - Complete Ablation of Stainless Steel Samples	II-24
4.19	Lateral View - Complete Ablation of Stainless Steel Samples	II-25
4.20	Frontal View - Incomplete Ablation of Stainless Steel Samples	II-26
4.21	Lateral View - Incomplete Ablation of Stainless Steel Samples	II-27
4.22	Types of Oxide Formed on Stainless Steel Samples	II-28
4.23	Schematic Diagram of Samples of Variable Geometry	II-29
4.24	Steady State Temperature Profiles for Inconel Samples	II-30
4.25	Typical Oxidation Plot for Inconel at 1350°C	II-31
4.26	Frontal View - Complete Ablation of Inconel Samples	II-32
4.27	Lateral View - Complete Ablation of Inconel Samples	II-33
4.28	Frontal View - Incomplete Ablation of Inconel Samples	II-34
4.29	Lateral View - Incomplete Ablation of Inconel Samples	II-35
4.30	Steady State Temperature Profiles for Beryllium Samples	II-36
4.31	Frontal View - Ablation Sequence of Beryllium Samples	II-37
4.32	Lateral View - Ablation Sequence of Beryllium Samples	II-38
4.33	Frontal View - Ablation Sequence of Beryllium Samples	II-39
4.34	Lateral View - Ablation Sequence of Beryllium Samples	II-40
4.35	Plot of Beryllium Ablation Data	II-41
4.36	Plot of Initial Melt Data of Beryllium Samples	II-42

Acknowledgment

The authors wish to express their grateful appreciation for the generosity and help extended to them by Mr. Dan O' Hara of Thermal Dynamics Corporation, New Hampshire. Mr. O' Hara designed both heat flux calorimeters and prepared part of chapter 3 of this report. The authors also wish to express their appreciation for the assistance and help given by Dr. M. R. Trammell, Messrs. L. Grob, M. Korposh, and J. Sunday.

Summary

26246

This report describes an experimental investigation of the re-entry behavior of a series of metals and alloys currently envisioned as being important structural components in the NERVA reactor. In this investigation the re-entry behavior of one-half inch models was examined in a plasmajet facility. The materials studied were aluminum 6061-T6, aluminum alloy 2219-T852, titanium A 110-At, stainless steel 304-A, Inconel-X750, and beryllium.

As a result of this study the following conclusions can be made:

- (1) The ablation of aluminum, aluminum alloy, and titanium is determined entirely by the melting process.
- (2) In the case of titanium and stainless steel, the presence of a thick, tenacious oxide coat on the samples surface inhibits ablation. However, on pre-oxidized stainless steel samples, where cracks and spalling of the oxide layer were evident the ablation process is accelerated.
- (3) Rates of oxidation of all materials studied in the plasmajet system, appear, at least in a qualitative sense, to be similar to those obtained by investigators using static systems.
- (4) The ablation of Inconel-X and stainless steel at high heating rates is similar to that of aluminum, aluminum alloy, and titanium.

In addition, the following observations were made:

- (1) At low heating rates, Inconel-X and stainless steel underwent a phenomenon which was termed "incomplete ablation". Incomplete ablation was attributed to (a) a change in sample geometry which changed the total heating rate to the sample and (b) a change in position of the stagnation point which diminished the heating rate to the sample.
- (2) The ablation of beryllium required more heat than was theoretically predicted. The reasons advanced for this phenomenon were: (a) the heating rate to

the sample was lowered as a result of a change in sample geometry during early ablation and a change in position of the stagnation point (see (1) above) and

(b) a phase change may have occurred in the temperature range 1240-1260°C.

(3) Experimental aerodynamic stagnation point heat transfer data were obtained and agreed best with the theory of Ferri, et al. However, at Reynolds numbers less than 50, the experimental data deviated considerably from all aerodynamic theories considered in this study.

1.0 INTRODUCTION

One of the basic technical problems associated with the flight operation of nuclear powered rockets involves evaluating the ablation of reactor components and hardware during re-entry through the earth's atmosphere. This problem is important for three different reasons. First, reactor hardware may be activated during reactor operation. If in the event of reactor failure components re-enter intact, these components may constitute a nuclear hazard. Secondly, many components involved in nuclear reactors for space application are quite massive. If during random re-entry these fail to ablate, they might impact in a populated area and thus constitute a non-nuclear hazard. Thirdly, in the event that passive disassembly is utilized as a countermeasure, i. e., the reactor is allowed to re-enter intact, then it is necessary to evaluate the ablation characteristics of such components as the pressure vessel in order to ascertain if the reactor will disassemble during re-entry.

In order to evaluate the re-entry ablation characteristics of NERVA metallic components, an experimental study of metals and alloys which are important constituents of NERVA was performed. In this study the re-entry behavior of one-half inch models was examined in a plasmajet facility. The materials studied were aluminum 6061-T6, aluminum alloy 2219-T852, titanium A110-At, stainless steel 304-A, Inconel X-750, and beryllium. The following is a report on the results of this investigation.

2.0 BACKGROUND INFORMATION

When an object re-enters the earth's atmosphere at orbital or superorbital velocities, it will be subjected to enormous heat transfer rates as it undergoes deceleration from hypersonic to subsonic velocities. As a result of this deposition of thermal energy it is to be expected that the re-entering body may undergo both physical and chemical changes. For example, the body may melt, vaporize, or, if it is of an appropriate chemical composition, undergo chemical reactions with environmental gaseous species (e.g., oxidation) at the gas-surface interface. If, in the process of undergoing either physical or chemical change, the re-entering object loses mass, the process involved is termed ablation. Obviously, an investigation of re-entry behavior involves a consideration of (1) the energy deposition to a re-entering body and (2) the chemical and physical processes which a body may undergo under the thermal and environmental conditions encountered during re-entry.

The present paper is concerned with an experimental investigation of the re-entry behavior of a series of metals and alloys currently envisioned as being important structural components in the NERVA reactor. In order to understand this behavior, it is necessary first to examine the physical and chemical characteristics of these materials and the thermal effects to which they will be subjected during re-entry.

2.1 REACTIONS OF METALS AND ALLOYS

2.1.1 Physical Changes

A solid may undergo two physical changes when subjected to high temperatures: sublimation and liquification. Of these two, the latter is by far the more important. In general, the sublimation of metals proceeds at relatively slow rates which are strongly temperature dependent. At temperatures below the melting point, the sublimation rates of solid metals and alloys will be extremely low. As an illustration of this statement, see Table 2.1. It can be seen from an examination of the data in this table that the maximal rate of sublimation of a listed solid at its melting point is approximately

$10^{-4} \text{ g/cm}^2\text{-sec}$. Thus, it would take one of these solids with an external surface area of one cm^2 , 10^4 sec to lose one g of weight at its melting point, via the sublimation process. Since during re-entry high temperatures will be achieved only for periods of approximately a hundred seconds⁽¹⁾, the maximal mass loss obtainable via sublimation will be only of the order of 0.01 g/cm^2 . Thus, it appears reasonable to eliminate sublimation as an important process in the investigation of the ablation of re-entering metals.

With the elimination of sublimation as an important process in metal ablation, only melting need be considered in the broad category of physical changes. In fact, melting is probably the most significant process involved in metal ablation. In contrast to sublimation, the melting of a pure metal takes place only at one temperature, called the melting point. This temperature is rather invariant for any pure solid being only weakly dependent on pressure. In addition, melting may be considered as a first approximation to occur instantaneously at the melting point when sufficient heat is supplied for the solid to undergo phase transformation*.

The total heat required to melt a sample is given by the following equation:

$$\bar{Q}_m = \left\{ \int_{T_i}^{T_m} C_p dT + \Delta H_m \right\} W \quad (2-1)$$

where

- \bar{Q}_m = total heat required to melt a particular sample, cal
- C_p = specific heat of sample, cal/deg-g
- T = temperature, °K
- ΔH_m = heat of melting, cal/g
- W = sample weight, g.

* This statement is not intended to imply that the physical changes associated with a phase transformation are actually independent of time. It is well known that in the cases of fusion of liquids and liquification of vapors that the processes are time dependent. (For a discussion of time dependence of phase changes, see References (2) and (3)). Unfortunately the time dependence of melting has not received sufficient theoretical or experimental attention to warrant inclusion of this aspect of melting in this report. Therefore, in this study the assumption will be made that melting occurs instantaneously when an aggregate of solid receives sufficient heat to accomplish transformation of the solid to the liquid phase at the melting point.

Specific heat data, heats of melting and values of density are reported in Table 2.2 for those metals examined in this study.

2.1.2 Chemical Changes

During re-entry, metals may undergo two chemical reactions: oxidation and nitrification. In most cases the oxides and nitrides thus formed are solid materials which adhere to the metal surface. Thus, chemical reaction adds little to the ablation process but may in fact be inhibitory to the ultimate ablation of the solid.

2.1.2.1 Theory

Every metal will undergo oxidation under appropriate conditions of temperature and pressure. As a result an oxide layer forms over the external surface of the metal. As the oxide coating forms, the gas-metal interface disappears, and instead there exists a gas-oxide interface. For subsequent oxidation to occur the metal atoms in the metallic phase must diffuse through this oxide coating to the gas interface where they will then undergo reaction, or conversely, oxygen atoms or molecules must diffuse through the oxide layer to the metal phase where reaction will occur. The oxide layer may then be considered protective, and the rate of reaction will be dependent upon the rate of diffusion of reactant species through the oxide layer. The appearance of cracks in this film will, of course, alter the protective nature of the oxide coating, and diffusion will no longer be rate controlling. At high temperatures cracks quite frequently appear and a phenomenon known as "breakaway" oxidation occurs. "Breakaway" oxidation refers to a fast oxidation process during which the oxide coat is no longer protective. Under these conditions a thick oxide coat forms.

In general, most quantitative studies of metal oxidation have been conducted in the low temperature diffusion controlled regime. This is an unfortunate fact from the point-of-view of re-entry oxidation, since relatively high temperatures will be encountered during re-entry. However, during the early phases of re-entry, surface temperatures will be low, and diffusion controlled oxidation should prevail.

Since a complete description of the nature of the metal surface will be required for an analytical description of re-entry oxidation and ablation, it is worth examining diffusion controlled oxidation. It has been found empirically that the rates of metal oxidation reactions follow the following simple relationships⁽⁵⁾.

$$\text{Linear} \quad \Delta m = k_i t \quad (2-2)$$

$$\text{Parabolic} \quad (\Delta m)^2 = k_p t + C \quad (2-3)$$

$$\text{Cubic} \quad (\Delta m)^3 = k_c t \quad (2-4)$$

$$\text{Logarithmic} \quad \Delta m = k_e \log (at + 1) \quad (2-5)$$

where:

- Δm = the increase in the weight of the solid, g/cm²
- k_i = rate constant (units are a function of reaction rate order as defined via equations 2-2 through 2-5)
- t = time, sec
- C & a = arbitrary constants

An attempt will be made now to show the physical significance of the above empirical equations.

(1) Linear Relationship

A linear relationship will apply only in those cases in which the metal oxide is non-protective. An example of this behavior would be the formation of a highly porous or cracked oxide. In such a case reaction at the surface would be rate controlling. Assuming no dependence on the gas partial pressure, the following differential rate law would be valid:

$$\frac{d(MO)}{dt} = k_l \quad (2-6)$$

where

(MO) = the concentration of metal oxide on the solid surface.

Upon integration of the above equation a linear equation of type (2-2) would result.

(2) Parabolic Relationship

When the oxide surface is highly protective, the reaction rate is diffusion rate controlled. If the layer is sufficiently thick, steady state conditions may be assumed. Fick's first law is then valid and the following differential equation may be written:

$$\frac{d(MO)}{dt} = k D_m \left(\frac{\partial M}{\partial \chi} \right)_{ss} \quad (2-7)$$

where D_m is the diffusion constant of M across the metal oxide layer and $(\partial M / \partial \chi)_{ss}$ is the steady state concentration gradient of metal atoms across the oxide layer of thickness χ . This gradient is simply $(M_o) / \chi$ where (M_o) is the metal concentration at the oxide-metal interface and is hence, constant.

Since χ is proportional to (MO) , the mass of oxide on the surface, the following equation may be written:

$$\frac{d[\chi]}{dt} = \frac{k_p}{\chi} \quad (2-8)$$

which upon integration gives rise to the parabolic equation. In general, the parabolic law is the one most frequently followed in the case of metal oxidation.

(3-4) Logarithmic and Cubic

No accepted explanation has been offered for oxidation behavior following the logarithmic and cubic equations. In general, it would appear best to consider these equations simply as empirical means of representing rate data.

In all the rate equations one finds a rate constant, k , which is a function of temperature. The temperature relationship is given by the Arrhenius equation:

$$k = Ae^{-E/RT} \quad (2-9)$$

where

A = the frequency factor, (units are a function of reaction rate order)

E = the activation energy, cal/mole

R = the gas constant, cal/°K-mole

T = the temperature, °K

With a knowledge of rate law behavior and of the temperature dependence of the rate constant, it should be possible to predict the extent of oxidation during re-entry.

2.1.2.2 Summary of Oxidation Data

2.1.2.2.1 Aluminum

Gulbransen⁽⁶⁾ was the first to study the oxidation of aluminum in detail. He investigated the reaction in the temperature region 350 - 450°C and at a pressure of 76 torr. His results indicated that the reaction followed a parabolic rate law. The activation energy was found to be 22.8 k cal/mole, and the frequency factor was $10^{-7} \text{ g}^2 \text{ cm}^{-4} \text{ sec}^{-1}$. Later, Smeltzer⁽⁷⁾ extended these studies to 600°C. Below 500°C, he confirmed Gulbransen's finding that the reaction rate was parabolic. However, at about 500°C, the oxidation was observed to follow a linear rate law until the weight increased to $35 \mu\text{g/cm}^2$. Oxidation then ceased. The activation energy was 37.9 k cal/mole, and the frequency factor was $1.6 \times 10^{-3} \text{ g}^2 \text{ cm}^{-4} \text{ sec}^{-1}$. Aylmore, Gregg, and Jepson⁽⁸⁾ repeated Smeltzer's experiments and completely confirmed his results. Recent experiments of Cochran and Sleppy⁽⁹⁾ have also confirmed the earlier investigation except they found a maximum weight increase of approximately $6 \mu\text{g/cm}^2$.

The author ascribed these differences in oxidation levels to differences in surface roughness (BET surface area). No attempt has been made to evaluate the effect of surface roughness on oxidation rate.

2.1.2.2.2 Titanium

The oxidation of titanium appears to obey a relatively complex reaction mechanism. At temperatures below 350°C, Alexander and Pidgeon⁽¹⁰⁾ observed that titanium oxidation followed a logarithmic rate law. These results were later confirmed by Waber⁽¹¹⁾. In neither of these investigations was any attempt made to determine temperature dependence in terms of the Arrhenius parameters.

Oxidation in the temperature region 400 - 600°C was examined by Gulbransen and Andrews⁽¹²⁾. In these studies the oxygen partial pressure was 76 mm. It was found that the reaction followed a parabolic rate law and that the rate increased slightly with pressure. The frequency factor was found to be equal to $5.3 \times 10^{-6} \text{ g}^2 \text{ cm}^{-4} \text{ sec}^{-1}$; the activation energy was equal to 2.93 k cal/mole.

Davies and Birchenall⁽¹³⁾ studied the oxidation of titanium (99.5% purity) in a higher temperature region (650 - 950°C) and at higher pressures (760 torr, O₂). It was found that the oxidation rate was linear after an initial induction period. A change in Arrhenius parameters was noted at 830°C. Above this temperature the frequency factor equalled $400 \text{ g cm}^{-2} \text{ sec}^{-1}$ and the activation energy equalled 47 k cal/mole. Below this temperature the frequency factor decreased to $5 \text{ g cm}^{-2} \text{ sec}^{-1}$, and the activation energy decreased to 40 k cal/mole.

Jenkins⁽¹⁴⁾ also examined the oxidation of titanium in this high temperature region. His results were in accord with those of Davies and Birchenall in that he also observed linear rate law behavior after an initial induction period. However, the Arrhenius parameters are considerably different from those obtained earlier. Both parameters were constant over the entire temperature region studied, with E equal to 30.5 k cal/mole and A equal to $4 \times 10^{-2} \text{ g cm}^{-2} \text{ sec}^{-1}$. It is worth noting that at 925°C oxygen absorption of 36 mg cm^{-2} was observed. This value is considerably higher than observed in the case of aluminum oxidation and is indicative of the non-protective nature of the titanium oxide films.

Kofstad and Hauffe⁽¹⁵⁾ have examined the results in detail and have concluded that the high oxidation rate for titanium is the result of the high solubility of oxygen in titanium oxides.

2.1.2.2.3 Stainless Steel

In the case of alloy oxidation the problem of defining reaction rates is formidable. As will be noted in the case of nickel, traces of impurities may have a profound influence on oxidation behavior. Very little quantitative work which would be of use in a re-entry study is noted in the literature.

McCullough⁽¹⁶⁾ examined the oxidation behavior of types 410 and 304 stainless between 850 and 1200°C. He found that type 304 was more resistant to oxidation. He also observed that the extent of oxidation was dependent on oxygen partial pressure.

Campbell and Thomas⁽¹⁷⁾ studied the oxidation of type 302 stainless steel between 104 and 302°C. They found the reaction to follow a logarithmic rate law. Caplan and Cohen⁽¹⁸⁾ studied types 302, 309, and 330 stainless between 850 and 1100°C in dry air at one atmosphere pressure. They found type 309 to be the most oxidation resistant and type 302 to be the least resistant. In the case of the latter material, breakaway oxidation occurred at 1100°C. The maximum weight gain at 970°C ranged from 2 to 5 mg/cm². McCullough, Fontana and Beck⁽¹⁹⁾ studied types 304, 430 and 410 stainless in the temperature region 800 - 950°C. Oxidation in all cases followed the equation $W^n = kt$ during early stages with n varying from 0.88 to 1.46. The rate of oxidation was then found to increase abruptly because of rupture of the oxide scale. The length of time required for breakaway oxidation was found to decrease with increasing oxygen partial pressure and increasing temperature.

2.1.2.2.4 Inconel X

The oxidation of inconel X has not been studied.

2.1.2.2.5 Nickel

It appears that the most consistent oxidation results have been obtained in the case of nickel oxidation. Kubachewski and Goldbeck⁽²⁰⁾ studied the reaction between 750 - 1240°C. Their rate data fitted a parabolic law; the activation energy was 45 k cal/mole; and the frequency factor was $3.2 \times 10^{-2} \text{ g}^2 \text{ cm}^{-4} \text{ sec}^{-1}$. Frederick and Cornet⁽²¹⁾ extended these tests to 1400°C and obtained essentially the same results. The activation energy was found to be 50 k cal/mole. Zima's⁽²²⁾ studies at 1100°C were in accord with this. Gulbransen and Andrews⁽²³⁾ measured an activation energy of 45.1 k cal/mole. Their results indicated, however, that above 900°C some breakaway oxidation occurred. The amount of breakaway oxidation was hardly detectable, but it did cause a slight increase in the activation energy as a function of increasing temperature.

The most interesting observation in all the foregoing investigations was that the presence of impurities had a profound effect upon oxidation rates. Kubachewski⁽²⁰⁾ found that the presence of 0.48 wt. % Fe, 0.18 wt. % Mn, and 0.17 wt. % Si increased the reaction rate ten fold. Zima⁽²²⁾ found that the addition of 2.0 wt % Cr would increase the rate nine fold. Frederick⁽²¹⁾ found that 3.6 wt % cobalt was required for a ten fold increase in oxidation rate.

2.1.2.2.6 Beryllium

Gulbransen and Andrews⁽²⁴⁾ studied the oxidation of beryllium over the temperature range 350 - 950°C and at pressures ranging from 7.6 to 38 mm O₂. Rate data were found to fit a parabolic rate law, but the temperature dependence of the reaction rate was complex. Between 300 and 700°C, the activation energy and the frequency factor were equal to 8.5 k cal/mole and $1.8 \times 10^{-12} \text{ g}^2 \text{ cm}^{-4} \text{ sec}^{-1}$, respectively. In the temperature region 700 to 950°C the activation energy increased to 50.3 k cal/mole and the frequency factor increased to $3.5 \times 10^{-3} \text{ g}^2 \text{ cm}^{-4} \text{ sec}^{-1}$. It was also observed that the reaction rate increased slightly with an increase in oxygen pressure. These results, however, were not amenable to interpretation nor did they appear significant.

Cubicciotti's⁽⁴²⁾ studies, in the temperature region 840 to 870°C, also indicated parabolic rate behavior. However, he found an activation energy of 62 k cal/mole and a frequency factor of $0.22 \text{ g}^2 \text{ cm}^{-4} \text{ sec}^{-1}$. The reaction rate was found to be independent of oxygen partial pressure.

Recently, Aylmore, Gregg and Jepson⁽⁴³⁾ re-examined the oxidation in the temperature range 500 to 750°C. The major difference between these investigations and the earlier ones was that the more recent study involved time periods ranging up to 300 hours whereas the earlier ones involved studies of only two hours duration. It appeared in these studies that the oxidation was protective at temperatures below 700°C. The rate data fit the logarithmic rate equation rather than a parabolic equation. The authors concluded that this variation was not significant but was rather the result of the presence of impurities in the beryllium samples. At 750°C breakaway oxidation occurred, and a linear rate law was obeyed. The authors theorized that this change in reaction rate behavior was caused by the development of cracks in the oxide layer. Later, the same authors examined the oxidation behavior in water saturated oxygen and observed breakaway oxidation at 650°C.

2.1.2.3 Summary of Nitrification Data

In comparison with the amount of experimental work performed in the field of oxidation, the amount of information available regarding nitrification is small.

2.1.2.3.1 Aluminum

No information was found in the literature.

2.1.2.3.2 Titanium

Gulbransen and Andrews⁽²⁵⁾ examined the reaction between nitrogen and titanium in the temperature range 550-850°C and found that a parabolic rate law was obeyed. The temperature dependence of the rate constant was found to fit the following equation,

$$k_p = 3.8 \times 10^{-5} \exp(-36,300/RT) \text{ g}^2 \text{ cm}^{-4} \text{ sec}^{-1}$$

2.1.2.3.3 Stainless Steel

No information was found in the literature.

2.1.2.3.4 Inconel

No information was found in the literature.

2.1.2.3.5 Beryllium

Gulbransen and Andrews⁽²⁶⁾ investigated the beryllium-nitrogen reaction at 7.6 cm Hg pressure of purified nitrogen over the temperature range 650-925°C using the vacuum microbalance technique of their oxygen investigation. A stable and insoluble nitride film was formed. Its molecular volume was greater than that of the metal, and the film was protective below 875°C. Parabolic rate law plots ((weight gain)² vs time) were substantially straight up to this temperature, but above it the slope increased steadily after 60 min indicating that the layer was no longer protective. This "breakaway" corrosion was accompanied by a change in the appearance of the nitride film. The nitriding rate was slightly lower than the oxidation rate. Parabolic rate law constants were evaluated from data in the time ranges 60-120 min up to 875°C and 0-60 min at 900 and 925°C. An activation energy of 75 k cal/mole was obtained for the temperature range 725-925°C. This is even higher than the oxidation activation energy, but positive values of the entropy of activation reduced the free energy to values close to those of the oxygen reaction.

2.1.2.4 Possible Influence of Oxides on the Ablation Process

Table 2.3 lists some thermal data for the oxides which will probably be formed during the re-entry of the materials examined in this study. Two facts are apparent from an examination of these data:

- (1) The oxides of all metals and alloys studied in this investigation melt at higher temperatures than do the metals and alloys themselves.

- (2) The heats of dissociation of these oxides are excessively large.

These two facts suggest a possible deleterious effect resulting from metal oxidation during re-entry. If a thick oxide coat forms early in the re-entry process, this coat may actually inhibit the ablation of a re-entering body when it is subjected to maximal heat fluxes in the latter stages of re-entry. First, the oxide coat will have lower thermal conductivity than the metal will. Thus, heat transfer from the oxide surface to the metal may be quite low. Secondly, since the metal oxide has a higher melting point than does the metal, the body's surface will have to reach a higher temperature for the oxide to melt, than would be required if the metal alone were under consideration. Thirdly, the high energies required for the oxides to dissociate indicate that these oxides might act as heat shields during re-entry with much of the aerodynamic heating being absorbed in the dissociation process.

An experimental examination of the role of oxidation in ablation will be given in Section 4.2.1.3.

2.2 Re-Entry Heat Considerations

2.2.1 Glossary of Aerodynamic Symbols

The following list of aerodynamic symbols will be used in evaluating re-entry heat transfer.

\bar{c}_p	= mean specific heat of a gas mixture, cal/deg -g
D	= the diffusion coefficient, cm^2/sec
$\left(\frac{d U_e}{dx}\right)_s$	= stagnation point velocity gradient, sec^{-1}
	= $1/R \ 2(P_s - P_\infty) / \rho_s$
$(g_b')_{Pr=1}$	= a constant obtained from appropriate boundary layer solutions
h_D	= average atomic dissociation energy times atom mass fraction in external flow, cal/g
h_s	= gas stagnation enthalpy in external flow, cal/g

h_w	= sample enthalpy at wall, cal/g
k	= thermal conductivity of a gas, cal/cm - deg-sec
h_{se}	= reference stagnation enthalpy, cal/g (see Reference 29)
L	= dimensionless Lewis number, $D\bar{c}_p/k$
P_s	= pressure at stagnation point in external flow, g/cm-sec ²
P_∞	= free stream pressure, g/cm-sec ²
Pr	= the dimensionless Prandtl number, $\bar{c}_p\mu/k$
\dot{q}_{FM}	= stagnation point heat flux in the free molecular flow regime, cal/cm ² -sec
\dot{q}_θ	= heat flux at some position θ on the surface of a hemisphere, cal/cm ² -sec
\dot{q}_s	= stagnation point heat flux, cal/cm ² -sec
\dot{q}_t	= heating rate to a surface = $\dot{q}_w A$, cal/sec
\dot{q}_w	= average heat flux to a surface, cal/cm ² -sec
$(\dot{q}_w)_{VORT}$	= heat flux at the wall in the presence of vorticity, cal/cm ² -sec
$(\dot{q}_w)_{VORT=0}$	= heat flux at the wall as predicted by boundary layer equations, cal/cm ² -sec
R	= sample radius, cm
Re_s	= shock Reynolds number $\rho_\infty R_s U/\mu_s$
R_s	= radius of shock, cm
U	= free stream velocity, cm/sec
U_e	= velocity component tangential to the body surface as defined by boundary layer considerations, cm/sec
U_o	= velocity component tangential to the wall for inviscid flow, cm/sec (see reference 29)

$\left(\frac{1}{U} \frac{dq_\theta}{d\theta} \right)_s$	= the stagnation point velocity gradient which for a sphere equals $(3 \epsilon)^{1/2}$
ϵ	= density ratio across the shock ρ_∞ / ρ_s
θ	= angular location of point on the surface of a sphere
μ	= absolute coefficient of viscosity at the stagnation point, g/cm-sec
μ_w	= absolute viscosity at the wall of a body, g/cm-sec
ρ_s	= mass density at the stagnation point in external flow, g/cm ³
ρ_w	= absolute density at the wall of a body, g/cm ³
ρ_∞	= free stream density, g/cm ³

2.2.2 Aerodynamic Heating - Stagnation Point

The problem of defining heat transfer rates under hypersonic re-entry conditions has received considerable attention during the past few years. Numerous theories have been developed some of which will be discussed briefly here.

2.2.2.1 High Reynolds Number Heating

Probably the theory most frequently used to evaluate re-entry heating is that developed by Fay and Riddell⁽²⁷⁾. This theory applies to the case of viscous hypersonic flow. As a result it is applicable only at high Reynolds numbers ($Re > 5000$) since only under these conditions is a well defined boundary layer produced. Using the boundary layer equations, Fay and Riddell have derived the following stagnation point heat transfer equation for the case of the equilibrium boundary layer:

$$\dot{q}_s = 0.76 Pr^{-0.6} (\rho_w \mu_w)^{0.1} (\rho_s \mu_s)^{0.4} \times \left\{ 1 + (L^{0.52} - 1) h_d/h_s \right\} (h_s - h_w) \sqrt{(dU_e/dx)_s} \quad (2-10)$$

This equation has been subjected to considerable experimental verification, and its validity is generally well accepted. Unfortunately, in the performance of arc plasmajet experiments on the ablation of small samples, it is not always possible to achieve Reynolds numbers sufficiently high to allow its use. It is, therefore, necessary to consider those theories which have been developed to predict heat transfer in the low Reynolds number regime.

2.2.2.2 Low Reynolds Number Heating

2.2.2.2.1 Probstein and Kemp

In this analysis of aerodynamic heating, Probstein and Kemp⁽²⁸⁾ solved the Navier-Stokes equations for two sets of boundary conditions:

- (1) A "viscous layer" class in which a thin shock wave exists, but in which the region between the shock and the blunt body is fully viscous and
- (2) A "merged layer" class for more highly rarified flow which applies to Reynolds numbers less than 100.

For the viscous layer solution the following equation was derived for stagnation point heating of a sphere:

$$\dot{q}_s = \frac{\dot{q}_{FM}}{Re_s} \left[(1/U) \left(\frac{dq_\theta}{d\theta} \right) \right]_s^{1/2} \left(\frac{R_s}{R} \right)^{1/2} \times \left(\frac{Re_s}{\epsilon} \right)^{1/2} [Pr]^{-0.6} (g_b')_{Pr=1} \quad (2-11)$$

For the merged layer, the shock wave is considered not to be thin, and the Navier-Stokes equations are used to provide a solution which includes the structure and which uses free stream conditions as outer boundary conditions. The equations for the incipient merged layer will not be reported herein for the sake of brevity. Rather a numerical comparison of the heat transfer values predicted by various theories will be discussed in Section 2.2.2.3. For a complete discussion of the incipient merged layer regime see reference 26.

2.2.2.2.2 Ferri, Zakkay, and Ting

In the analysis of Ferri, Zakkay, and Ting⁽²⁹⁾

the boundary layer concept is retained and modified. It is shown that the effects of viscosity and conductivity in the flow outside the boundary layer modify the heat transfer rate at the wall in the region between the stagnation point and the sonic point by less than 5% for Reynolds numbers as low as 30. These investigators indicate that at low Reynolds numbers the shear produced in the boundary layer by shock-induced vorticity becomes of the same order as the shear stress at the wall. Hence, they include the effect of vorticity in the boundary layer analysis. Using this approach, the following equation is derived for heat transfer in the low Reynolds number regime:

$$(\dot{q}_w)_{\text{VORT}} = (\dot{q}_w)_{\text{VORT} = 0} \sqrt{U_e/U_o} \left(h_{se}/h_s \right) \quad (2-12)$$

2.2.2.3 Comparison of Theories

Because of the complexity of the aforementioned equations it is difficult to compare them on a strictly analytical basis. Therefore a comparison of the heat transfer rates as predicted by these theories is shown in Figure 2.1. Here the dimensionless Stanton number, C_H , is plotted as a function of Reynolds number, where the Stanton number is defined as,

$$C_H = \frac{\dot{q}_s}{\rho_\infty U h_s}$$

It is obvious from a comparison of all theories that those concerned with the low Reynolds number regime predict higher heat transfer rates than are predicted from boundary-layer consideration. Because of the importance of accurate aerodynamic heating data in predicting ablation and in view of (1) the divergences of theoretical predictions and (2) the lack of experimentally determined plasmajet heat flux data in the low Reynolds number regime, an experimental program was undertaken to determine the rate of heat transfer in this regime. This study is reported in Section 3.0.

2.2.3 Average Aerodynamic Heating

The equations which have just been considered are in general applicable only to stagnation point heating. In order to evaluate re-entry heating to hemispherically shaped samples, it is necessary to consider not only the heating at the stagnation point but also the average heating rate over the sample. It is true in the case of both free molecular flow and boundary layer flow⁽³⁰⁾ that the concept of a Newtonian pressure distribution over the surface of a sphere appears to be valid. This concept gives rise to the following equation,

$$\dot{q}_\theta = \dot{q}_s \cos \theta \quad (2-13)$$

which on integration indicates that the average heat flux to a hemisphere \dot{q}_w is as follows

$$\dot{q}_w = 0.5 \dot{q}_s \quad (2-14)$$

Since this equation is valid from both free molecular and boundary layer considerations, it would seem in the case of the low Reynolds number regime that it should also apply. Nevertheless, it did not appear in the course of this study that such a conclusion is valid, a priori. Therefore, an experimental investigation was undertaken to evaluate \dot{q}_w . The results are reported in Section 3.0.

2.2.4 Other Heat Transfer Considerations

In the testing of ablative materials one must take into account those means by which the samples tested lose heat. The two primary mechanisms involved in heat loss are radiation and conduction. The radiation loss term is readily evaluated from the Stefan Boltzman equation,

$$\dot{q}_{\text{rad}} = \epsilon \sigma AT^4 \quad (2-15)$$

where	\dot{q}_{rad}	= the rate of heat energy loss, cal/sec
	σ	= the Stefan Boltzman constant, 1.36×10^{-12} cal/cm ² - sec - °K ⁴
	A	= total surface area, cm ²
	T	= temperature, °K
	ϵ	= sample emissivity

A list of emissivities for the samples tested in this study are given in Table 2.4.

The problem of heat loss to the sample holder is a much more difficult one to evaluate. The difficulty arises from the fact that the holder itself receives heat input from the shock during testing. Therefore, calorimetric techniques may not be used for heat loss consideration. In the course of these studies, every attempt was made to minimize such loss via such techniques as using a boron nitride holder and cutting down surface contact between sample and holder (see Section 4.1.6). Nevertheless, heat losses to the holder do warrant consideration and will be considered in terms of the test results for individual samples.

Finally, a word about heat transfer within the sample. One of the basic problems of concern in the high temperature behavior of any material is that of thermal conductivity within the sample. However, because of the nature of the materials considered in this study (i.e. all were metals and alloys of reasonably high thermal conductivity) and because of the smallness of the samples tested (one half inch diameter hemispheres), it was felt that thermal gradients within the samples should be absent. Therefore, when the experimental data were interpreted, no attention was paid to the problem of sample heat transfer.

2.3 HEAT BALANCE FOR ABLATION

In view of the aerodynamic heating and heat loss considerations just discussed and assuming that melting represents the primary means of sample ablation, the following equation may be written to express the total energy required to ablate a sample at a fixed re-entry point:

$$\begin{aligned}
 W \left[\Delta H_m + \int_{T=T_i}^{T=T_m} C_p dT \right] &= \dot{q}_w \times t_m \times A - \int_{t=0}^{t=t_m} \dot{q}_{rad} dt \\
 &- \int_{t=0}^{t=t_m} \dot{q}_{cond} dt
 \end{aligned}
 \tag{2-16}$$

where

W	= weight of sample, g
ΔH_m	= heat of melting, cal/g
C_p	= specific heat of sample, cal/deg-g
T_i	= sample temperature at start of run, °C
T_m	= melting point, °C
\dot{q}_w	= average re-entry heat flux, cal/cm ² -sec
A	= surface area of sample, cm ²
t_m	= time at which sample has completely ablated (total time of test), sec
\dot{q}_{rad}	= heat loss rate via radiation, cal/sec
\dot{q}_{cond}	= heat loss rate via conduction to sample holder, cal/sec

Equation (2-16) will be utilized in Section 4.2 to explain the ablation phenomena observed in the experimental testing program. When anomalies to this equation are observed, these will be noted, and possible hypotheses will be advanced to explain these anomalies.

3.0 AERODYNAMIC HEATING STUDIES

As has been noted, considerable uncertainty exists in predicting the aerodynamic heating of objects in the low Reynolds number regime. In order to evaluate the extent of this heating, an experimental study was performed.

3.1 EXPERIMENTAL

3.1.1 Facility Description

The experimental data for this report were collected at a hyperthermal wind tunnel facility, located at Thermal Dynamics Corp., Lebanon, New Hampshire.

The arc heater used in this hyperthermal tunnel is a standard Thermal Dynamics F-80 plasma torch. The torch utilizes water cooled electrodes, a thoriated tungsten cathode and a copper anode. Electrode configurations were both standard Thermal Dynamics design, and some special configurations were designed for low mass flow rates.

The dc electrical power for the operation of this plasma generator was supplied by four selenium rectifiers of 24 kW capacity each. Each of the power supplies has a 70 volt open circuit potential, and most of the work done used a series parallel connection for 140 volts open circuit. Suitable control circuitry was provided to regulate the power output level of the rectifiers. The input power to the gas was determined by measuring the potential across the electrodes and the amperage.

The arc heater or plasma torch was operated using pre-purified nitrogen as the plasma gas. The nitrogen plasma was exhausted from the anode of the torch into a plenum chamber where pre-purified oxygen was added to make simulated or tailored air. The gas mixture used was 3.34 parts of nitrogen to one part of oxygen by weight. The configuration of the plenum chamber was such that uniform gas mixing could be expected to occur over the ranges of flow used to achieve the required test conditions.

The gas supply system of this tunnel consisted of standard gas cylinders of pre-purified nitrogen and oxygen with pressure regulators at the cylinders to provide a metering pressure of from 30 to 80 PSIG. The gas metering system consisted of a bank of various sized rotameters (variable area flowmeters) with pressure gauges attached at the rotameters and needle valves downstream for the regulation of gas flow.

The air plasma was exhausted from the plenum chamber into a low pressure environment through a supersonic nozzle. This nozzle consists of a simple conical expanding section designed for Mach 3 flow at 10,000 Btu/lb enthalpy and 0.1 atmosphere chamber pressure. In order to achieve this, the entire plasma torch and nozzle plenum assembly were mounted inside a large vacuum chamber.

The vacuum chamber used was 32" in diameter by 72" long. This chamber was evacuated by means of a Roots-type blower with 3,600 cubic ft/min capacity at 1 torr, backed by a mechanical pump. An 80 kW heat exchanger was used to cool the gas between the vacuum tank and the inlet of the blower in order to protect the blower and increase its efficiency.

3.1.2 Stagnation Pressure Measurements

The stagnation pressures associated with each run were measured with a water cooled total head probe. The pitot pressure probe was a flat faced probe with an outside diameter of 1/2" and 1/6" sensing hole in the center. This probe was inserted into the stream centerline prior to each test run.

3.1.3 Stagnation Enthalpy Measurements

The total enthalpy of the air plasma issuing from the supersonic nozzle was determined by performing a heat balance calculation on the plasma generator. The measurement of the electrical power into the generator was made on the basis of the volt-meter and ammeter readings. The amount of power lost to the plasma generator was determined on the basis of a coolant flow rate and temperature rise. Subtracting this from the input power level gives the power input to the gas, and knowing the gas mass flow, the total gas enthalpy is calculated.

3.1.4 Calorimetric Measurements

3.1.4.1 Stagnation Point Calorimeter

The measurements of stagnation point heat transfer rates were made with a steady state probe one inch in diameter. The probe designed and built for this experiment is shown in Figure 3.1. The desired function of this probe is to measure the exact amount of heat input into a small sensing area on the front face of the probe where the enthalpy and pressure are known.

The theory of operation of this probe is to supply a separate stream of cooling water to a small area at the tip of the probe. The mass flow of coolant to this section and the temperature rise of the coolant can then be measured, and the heat input to the sensing area calculated on this basis. Using the area of the probe surface cooled by the sensing water, the stagnation point heat flux may be determined.

A schematic diagram of the probe is shown in Figure 3.2. There are two complete loops that the cooling water may take, the inner (sensing element) loop or the outer (sheath) loop. The water connections are made such that the cold water flow is on the inside of the outer loop and the outside of the inner loop. This is done to eliminate any heat transfer between these two streams through the metal wall separating them. The outgoing flow of sheath cooling water is separated from the incoming water by a plastic tube in order to minimize the heat flow from the outer stream into the central part where it would be transferred into the sensing element coolant and thereby affect the results.

The cooling water in the sensing loop cools only the small sensing area at the nose of the probe. The temperature of this water is measured by a thermocouple in the outgoing tube of the sensing loop about 1/4" from the end of this tube. This measurement is made near the end of the tube to minimize the effect of any heat transferring in and out of this coolant stream in the rest of the probe structure. The coolant flow through the sensing loop is measured by a rotameter.

In operation, the probe is placed beside the plasma stream with the coolant flow turned on to the desired value. The temperature of the coolant water as measured by the sensing thermocouple is monitored and recorded on a strip chart. When the probe is inserted into the plasma stream, the temperature rise of the coolant water is measured and recorded. This value of ΔT plus the coolant flow rate provides enough information to calculate the heat flux to the sensing area (stagnation point).

The heat flux probe is considered to give a reasonably reliable measurement of the heat flux. Probably the weakest point of this probe is the assumption regarding the surface area of the sensing element. This area is figured to cover the surface of the hemisphere in the area defined by the center of the wall separating the sensing flow from the sheath water flow. This would be correct if the wall of the dividing partition was known to be cooled equally by the water on each side of the partition. However, this is not necessarily the case.

At some of the low enthalpy, low pressure points it was found to be rather difficult to have a ΔT measurement large enough to show up accurately on the strip chart recorder. In order to overcome this difficulty, the water flow to the cooling element was decreased in several low enthalpy runs. One of the assumptions made in the design of the probe is that all of the heat from the sensing face of the probe goes into the sensing coolant stream. If this assumption were correct, the temperature rise in the coolant stream should be inversely proportional to the coolant flow, becoming infinite at zero flow. This is not the case because as the flow is decreased in the sensing loop, the relative cooling effect of that water compared to the sheath coolant water decreases. This happens because the water velocity becomes so much lower. It has been experimentally verified that with no coolant flow to the sensing area the probe will not melt. Adequate cooling is available from the sheath coolant to protect the entire probe. In this case the sheath cooling water is carrying away all of the heat to the sensing area.

This probe cannot, therefore, be used at zero flow. It should be expected that the probe would not be reliable at very low flows because some proportion of the heat to the sensing element would go to the sheath coolant. This

theory was experimentally checked out at several test points, and a graph of the measured heat flux at different flow rates at test Point 11 is shown in Figure 3.3. These data bear out the theory that the probe would be expected to become more accurate as the coolant flow through the sensing area is increased. Accordingly, all of the tabulated data to be presented here was obtained at the maximum coolant flow rate consistent with a readable ΔT .

3.1.4.2 Average Heat Flux Calorimeter

The probe discussed in the foregoing section was intended to measure the heat flux at the stagnation point only. It was desirable to measure the heat flux to a 1/2" diameter hemispherical sample in order to calculate the heat input to one of the samples under test. It was also of interest to measure the heat input to the sides of the sample if a 1/2" diameter hemisphere was mounted on a variable length cylindrical section of the same material.

The probe fabricated for these tests was similar in some respects to the one inch diameter probe; however, the construction allowed for a change in the configuration of the sensing area. For this probe the sheath coolant passed through an entirely separate sheath section which was slipped over the sensing element which comprised the main structure of the probe. This coolant sheath avoided any heat transfer to the side walls of the probe, and, therefore, only one water coolant stream to the probe itself was required. The sheath could be slipped up and down the probe to vary the amount of side wall exposed to the plasma during a given test.

One disadvantage of this probe, due primarily to difficulties in fabricating the probe, is that the copper construction of the nose section of the probe is too thick. The effect of this is to decrease the temperature rise rate of the coolant stream.

The operation of the half-inch calorimeter probe was very similar to that of the one-inch probe. A thermocouple located in the outlet coolant stream of the main probe was monitored before placing the probe in the plasma stream. When the probe was placed in the plasma stream, the temperature increase was recorded on the strip chart recorder. One major difference between the operation of the two probes

was that the one-inch probe reached a steady temperature after about five seconds; whereas, the half-inch probe took about sixty seconds or in some cases longer to reach a steady state.

The instrumentation used on this probe was exactly the same as that used on the larger calorimeter.

The probe was run in four different configurations at each of the test points of interest. The first is with the sheath slid up so that only the half-inch hemispherical nose of the probe was exposed to the plasma stream. The second was with the sheath slid back one-half inch from the former position so that the hemisphere plus one-half inch of cylindrical wall were exposed to the plasma stream. The third configuration was with the sheath back one inch, and the fourth with the sheath back to the maximum rearward position, one and three-eighths inches behind the end of the hemisphere. In all cases the plasma flow direction was parallel to the axis of the probe, directly head on to the hemisphere and along the side of the cylindrical section.

3.2 RESULTS

The results for stagnation point heat transfer, \dot{q}_s , to the one inch calorimeter probe are given in Table 3.1 along with the experimentally measured stagnation enthalpies and pressures. The calculated value of the Reynolds number for a one inch diameter hemisphere at each test point is also included.

The results for total heating rate, \dot{q}_t , to the one-half inch calorimeters are given in Table 3.2.

3.3 COMPARISON OF RESULTS WITH THEORY

In Figure 3.4 plots of the theoretically predicted Stanton number as a function of Reynolds number for the theories of Fay-Riddell,⁽²⁷⁾ Probstein and Kemp⁽²⁸⁾, and Ferri⁽²⁹⁾ are shown. Also included in this figure are the experimentally determined Stanton numbers. It is apparent from an examination of these data that in the Reynolds number regime from 60 to ~1500 that boundary layer considerations predict excessively low heat fluxes. It would appear that Ferri's theory offers the best prediction for heat

flux in this regime. However, it does appear that even this theory is somewhat low in the Reynolds number region between 500 and 1000. At low Reynolds numbers (< 50), however, the experimental values show a definite tendency for the Stanton numbers to decrease with decreasing Reynolds numbers. None of the theories presented in this report predict such a phenomenon. Since it is believed that this tendency is real (i.e. outside the limits of experimental uncertainty), it is suggested that this phenomenon is worthy of future theoretical attention.

In Figure 3.5 a plot of \dot{q}_t as reported in Table 3.2 versus \dot{q}_s times the surface area of a one-half inch hemisphere is shown. In these plots the value for \dot{q}_s was corrected according to the following equation:

$$\dot{q}_s (1/2") = \dot{q}_s (1") \left(\frac{h_s (1/2")}{h_s (1")} \right) \left(\sqrt{\frac{R (1")}{R (1/2")}} \right)$$

where

$\dot{q}_s (1/2")$	= corrected stagnation point heat transfer to a 1/2 inch diameter hemisphere, $\text{cal/cm}^2\text{-sec}$
$\dot{q}_s (1")$	= experimental stagnation point heat transfer to a one inch diameter hemisphere, $\text{cals/cm}^2\text{-sec}$
$h_s (1/2")$	= stagnation enthalpy to 1/2 inch calorimeter, Btu/lb
$h_s (1")$	= stagnation enthalpy to 1 inch calorimeter, Btu/lb
$R(1")$	= radius of 1 inch calorimeter
$R(1/2")$	= radius of 1/2 inch calorimeter

This correction equation was necessary to take into account the difference in radii of the two calorimeters and also the slight difference which exists in stagnation enthalpies.

It is seen in this plot that the average heat transfer rate to a hemisphere is 0.34 times the stagnation point heat transfer rate. This is somewhat less than predicted by Newtonian theory according to equation (2-14). Here the theoretically predicted value is 0.5. This difference is not surprising in that there is no reason to anticipate a Newtonian pressure distribution in the low Reynolds number regime. The decrease in slope to 0.06 at high heat fluxes is surprising. No explanation can be offered for this phenomenon at present.

4.0 METALS ABLATION

4.1 EXPERIMENTAL

While it is not possible in performing plasmajet tests to duplicate all of the environmental conditions encountered during re-entry, it is possible to reproduce those properties which exist at the surface of a re-entering object, namely, stagnation pressure and enthalpy. Since the oxidation and ablation rates of a material depend not on free stream properties but rather on surface properties and since the designation of both stagnation enthalpy and pressure will define both the altitude and velocity of a re-entering particle, it is possible to study experimentally the oxidation and ablation of re-entering objects with a high degree of certainty.

4.1.1 Apparatus

The experimental tests were run in a plasmajet facility at the Thermal Dynamics Corporation, Lebanon, New Hampshire as described in Section 3.1.1.

4.1.2 Stagnation Pressure Measurements

See Section 3.1.2

4.1.3 Stagnation Enthalpy Measurements

See Section 3.1.3

4.1.4 Sample Temperature Measurements

Model surface temperatures were read with a single wave length (650 microns) optical pyrometer and were recorded automatically on a Varian recorder during the entire exposure time. Emissivity corrections were applied to the readings obtained with the pyrometer.

4.1.5 Materials

The materials studied were aluminum 6061-T6, aluminum alloy 2219-T852,

titanium A110-At, stainless steel 304-A, Inconel X-750 and beryllium. Table 4.1 lists the compositions of these materials.

4.1.6 Procedure

The metals and alloys were machined into hemispherical models, one-half inch in diameter.

The models were held by a boron nitride sting support, which in turn was attached to a water cooled support. The low thermal conductivity and the excellent tooling qualities of boron nitride made it a suitable material for use as a sample holder. A vacuum was applied to the holder to maintain the samples in place. The only point of thermal contact between the sample and the boron nitride holder was at the lip of the holder and the back of the hemisphere. The stem of the sample did not make thermal contact with the holder. The sample holding system is shown in Figure 4.1.

At the beginning of each run the water cooled pitot tube was inserted into the stream centerline to measure the total pressure behind the normal shock. In addition, the gas enthalpy was computed for each run by the energy-balance method. Oxygen and nitrogen flow rates were also recorded.

After all the necessary parameters had been measured, each test sample was quickly inserted into the flow. Visual observations were made through the tunnel window. At each test point, four or five exposure times were examined for each material. Each model was weighed before and after exposure using a Mettler balance capable of weighing to ± 0.0001 grams. Exposure times were taken from the Varian recorder plots and are within an accuracy of ± 0.1 sec.

Samples were studied throughout the ablation process as will be shown by a series of pictures to follow in Section 4.2. Complete ablation, as defined in this study, was taken to occur at that time when at least half of the total hemispherical mass of the sample was removed. An attempt was made to isolate the exact moment at which all the mass of the sample had been removed, but in very fast runs (running times less than 30 seconds) it was not always possible to isolate this point exactly. Obviously the subjective aspect of measuring ablation time introduces some uncertainty in this measurement.

However, as a result of running duplicate test points and of using different observers, it is believed that the uncertainty in ablation time was within $\pm 10\%$.

In the pictures which follow in Section 4.2 the presence of streamers on the sides of the samples will be observed. These streamers represent ablated material which had adhered to the cool sample holder. No attempt was made to remove this material from the sample when photographs were taken.

4.2 RESULTS

4.2.1 Titanium

The test points examined in the investigation of titanium are listed in Table 4.2 in terms of experimentally measured stagnation pressures and enthalpies as well as simulated altitudes and velocities. The significant reactions observed are also listed.

4.2.1.1 Non-Ablative Phenomena

4.2.1.1.1 Steady State

A number of samples did not ablate but rather achieved a steady state temperature at some temperature below the melting point. Figure 4.2 shows the surface temperatures for a number of these test points for a variety of different heating rates. An attempt was made to calculate these steady state temperatures using the following equation:

$$\dot{q}_f (\text{exp}) = \epsilon \sigma T^4 A \quad (4-1)$$

where all terms have been defined in Section 2.2.1. Table 4.3 lists all the calculated steady state surface temperatures along with those of actually measured temperatures. The calculated values are in agreement within 10%. This agreement is considered good since the optical pyrometer utilized in making the surface temperature measurements is accurate to only this amount.* This temperature agreement appears to support the assumption that the heat lost to the boron nitride holder is negligible.

* Pyrometer errors were due to uncertainties in emissivity values and pyrometer sightings.

4.2.1.1.2 Oxidation

Table 4.4 summarizes the oxidation characteristics of titanium over a range of surface temperatures and heating rates. As expected the oxidation rates were found to be temperature dependent. It was observed that the oxidation rate followed a linear rate law at surface temperatures below 1300°C. These results are in accord with those of Jenkins⁽¹⁴⁾ and Davies and Birchenall,⁽¹³⁾ who also observed linear rate law behavior in this temperature region. Figure 4.3 shows a typical oxidation plot at these lower temperatures.

At surface temperatures higher than 1500°C parabolic rate behavior was observed. Figures 4.4 and 4.5 show typical oxidation plots for two heating rates in the high temperature region.

4.2.1.2 Ablation

Table 4.5 lists the experimental times for complete ablation and the corrected heating rate values at each test run. Also listed are the integrated values of total re-entry heat input, \bar{Q}_t , the integrated heat lost to radiation, \bar{Q}_{rad} , and the experimental heat required to melt the sample, \bar{Q}_m .

The heating rate was evaluated from the experimentally determined heating rate measurements listed in Table 3.2. These values were corrected for changes in stagnation point enthalpies and wall enthalpies according to the following equation.

$$\dot{q}_t (\text{exp}) = \dot{q}_t (\text{ref}) \times \frac{(h_s - h_w) (\text{exp})}{(h_s - h_w) (\text{ref})} \quad (4-2)$$

where

$$\begin{aligned} \dot{q}_t (\text{exp}) &= \text{the heating rate at the test conditions, (cal/sec)} \\ \dot{q}_t (\text{ref}) &= \text{the heating rate at the reference conditions as listed} \\ &\quad \text{in Table 3.2, (cal/sec)} \end{aligned}$$

$(h_s - h_w) \text{ (ref)}$ = the difference between stagnation point enthalpy and sample wall enthalpy at the reference conditions in Table 3.2, (Btu/lb)

$(h_s - h_w) \text{ (exp)}$ = the difference between stagnation enthalpy and wall enthalpy at the test conditions, (Btu/lb)

In all cases the wall enthalpy at the test conditions was calculated for the sample at the melting point temperature. The integrated heating values, \bar{Q}_t , was taken equal to the product of $\dot{q}_t \text{ (exp)}$ and the time required to ablate the sample, t_m .

The integrated radiation heat loss values were calculated by integrating eq. (2-15), i. e.

$$\bar{Q}_{\text{rad}} = \int_{t=0}^{t=t_m} \epsilon \sigma T^4 A dt \quad (4-3)$$

where

$\epsilon = 0.8$ for titanium at the melting point

$A = 5.67 \text{ cm}^2$ (this value represented the total surface area of the sample—both back and front)

The value of temperature as a function of time was taken from the optical pyrometer chart measurement. The temperature-time data from these charts were fitted to linear graphs of the form

$$T = a + bt$$

When integrated a general equation of the following form resulted

$$\bar{Q}_{\text{rad}} = \frac{\epsilon \sigma A}{5b} \left[(a + bt_m)^5 - a^5 \right] \quad (4-4)$$

The net heat required to melt, \bar{Q}_m , was taken as the difference of \bar{Q}_t and \bar{Q}_{rad} . These values are listed in Table 4.5, and an average value of 1531 cal is reported. This compares well with a theoretical value of 1448 as calculated by equation (2-1) using the data of Table 2.2.

No attempt was made to ascertain the heat lost to the boron nitride sample holder. However, because of the relatively high heating rates employed in the study, heat losses to the sample holder should not be significant.

Figure 4.6 shows the features of the surface melting phenomena on a series of titanium samples at a heating rate of 183.4 cal/sec, and the times of significant events are indicated.

4.2.1.3 Effect of Oxide Coat on Ablation

It was observed in the course of these studies that the titanium oxide coating afforded a protective layer against titanium ablation. Varying amounts of oxide were formed on titanium samples under non-ablative conditions. These samples were tested in the plasmajet facility, and the ablation times, t_m , were compared with those of fresh (non-oxidized) samples. Table 4.6 lists these data. It is obvious that with an increase in oxide weight an increase in ablation time resulted as compared with the time required to ablate a non-oxidized sample.

4.2.2 Aluminum

The test points examined in the investigation of aluminum are listed in Table 4.7 in terms of experimentally measured stagnation pressures and enthalpies as well as simulated altitudes and velocities. The significant reactions observed are also listed.

4.2.2.1 Non-Ablative Phenomena

4.2.2.1.1 Steady State

Surface temperatures obtained for aluminum were far below the limitations of the optical pyrometer; therefore, steady state information was unobtainable.

4.2.2.1.2 Oxidation

The oxidation of aluminum was not a significant process, and no rate data were obtained. The maximum weight increase was 119 mg/cm^2 which is higher than found by Gulbransen⁽⁶⁾.

4.2.2.2 Ablation

All of the aluminum samples tested in this study underwent complete ablation. Over the range of heating rates there were two distinct types of ablation encountered by aluminum. The ablation of aluminum was found to be pressure dependent.

(1) At high stagnation pressures of 0.1 atmosphere or greater, the ablation is a severe tear away type. Figure 4.7 and 4.8 show the melting phenomena of a typical aluminum sample at these pressures. Figure 4.9 shows the type of particles collected from the ablating material.

(2) At a low stagnation pressure of 8.0×10^{-3} atmospheres a slow flowing type of ablation was observed. Figures 4.10 and 4.11 show the melting phenomena of a typical aluminum sample at these lower pressures. Figure 4.12 shows the type of particles collected from the ablating material.

The procedure used to calculate the heat of melting was identical with that used in the case of titanium (see Section 4.2.1.2). However, one basic experimental difficulty existed in the study of aluminum ablation, i. e., the recorded temperatures were well below the minimal temperature which can be measured by an optical pyrometer. Therefore, in estimating the heat losses of the sample due to radiation, it was not possible to use the experimental time-temperature plots as was done with titanium. It was, therefore, assumed that the integrated radiated heat loss could be approximated by assuming that the sample was at the melting temperature throughout the entire course of the run. Thus, the radiative heat loss was calculated by the following equation,

$$\bar{Q}_{\text{rad}} = \epsilon \sigma T^4 A t_m \quad (4-5)$$

The values of \bar{Q}_T , \bar{Q}_{rad} , and \bar{Q}_m are listed in Table 4.8. An examination of these data indicates that the heats of melting are not constant and in fact

appear to increase with increasing time of exposure. In all cases they are greater than the value theoretically predicted by equation (2-2). This value is 770 cal. The fact that the value of \bar{Q}_m increases with ablation time suggests one possible explanation. In the case of titanium, it was noted that because of the high heating rates involved (115 - 187 cal/sec) the heat lost to the boron nitride holder should be insignificant. This situation is not true with aluminum. Here heating rates range from 13.8 to 122.5 cal/sec. It is quite possible in this case, particularly in the lower heating rate range, that the heat losses to the holder contribute to the overall thermal balance. To test this hypothesis a plot was made of \bar{Q}_m/t_m vs $1/t_m$ (as defined in Table 4.8).

The basis for making such a plot involves a re-examination of equation 2-16, which is now repeated:

$$\begin{aligned}
 W \left[\Delta H_m + \int_{T=T_i}^{T=T_m} C_p dT \right] &= \dot{q}_w \times t_m \times A \\
 &- \int_{t=0}^{t=t_m} \dot{q}_{rad} dt - \int_{t=0}^{t=t_m} \dot{q}_{cond} dt
 \end{aligned} \tag{2-16}$$

If one assumes that the last term of this equation, $\dot{q}_{cond} dt$, may be approximately integrated as $B t_m$, then equation 2-16 may be rewritten as,

$$\frac{W \left[\Delta H_m + \int_{T=T_i}^{T=T_m} C_p dt \right]}{t_m} = \frac{\dot{q}_w + t_m \times A}{t_m} - \int_{t=0}^{t=t_m} \dot{q}_{rad} dt - B$$

Thus, a plot of \bar{Q}_m/t_m vs $1/t_m$ should give a straight line the slope of which should be equal to the net heat required to melt the sample, and the intercept of which should be equal to the heating loss rate to the holder. An examination of the data shown in Figure 4.13 indicates a reasonably linear fit of experimental data points and a slope of

838 cal which is in reasonably good agreement with the theoretically calculated value of 770 cal. The intercept value of 10 cal/sec would appear to represent the heating rate to the holder.

4.2.3 Aluminum Alloy

The test points examined in the investigation of aluminum alloy are listed in Table 4.9 in terms of experimentally measured stagnation pressures and enthalpies as well as simulated altitudes and velocities. The significant reactions observed are listed.

4.2.3.1 Non-Ablative Phenomena

4.2.3.1.1 Steady State

Surface temperatures encountered for aluminum alloy were far below the limitations of the optical pyrometer, and, therefore, steady state information was unobtainable.

4.2.3.1.2 Oxidation

The oxidation of aluminum alloy was not a significant process, and no rate data were obtained. The maximum weight increase was 119 mg/cm^2 , a value which is higher than that found by Gulbranson⁽⁶⁾.

4.2.3.2 Ablation

All of the aluminum alloy samples tested in this study underwent complete ablation. The ablation of aluminum alloy was also found to be pressure dependent as described in Section 4.2.2.2. The procedure used to calculate the heat of melting was the same as that described in this section. The values obtained are listed in Table 4.10. As in the case of aluminum, it is to be noted that the values of \bar{Q}_m increase with increasing ablation time. Therefore, once again \bar{Q}_m/t_m was plotted versus $1/t_m$. An examination of the data shown in Figure 4.14 indicates the data do not fit nearly as well as in the case of aluminum; however, the slope of 905 cal is in reasonably good agreement with the theoretical value of 770 cal.

4.2.4 Stainless Steel

The test points examined in the investigation of stainless steel are listed in Table 4.11 in terms of experimentally measured stagnation pressures and enthalpies as well as simulated altitudes and velocities. The significant reactions observed are listed.

4.2.4.1 Non-Ablative Phenomena

4.2.4.1.1 Steady State

Figure 4.15 shows the surface temperatures for a series of test points with varying heating rates. Table 4.12 lists all the calculated steady state surface temperatures (calculated according to equation 4-1) and the experimentally measured values. The calculated and actual temperatures were evaluated using a total hemispherical emissivity value of 0.85.

4.2.4.1.2 Oxidation

Oxidation rates for stainless steel are rather difficult to obtain due to spalling of the oxide coat. Figures 4.16 and 4.17 show typical oxidation vs time curves obtained for stainless steel at two heating rates. The initial oxidation rates appear to be parabolic, i.e., the rate is governed by the diffusion of vacancies in the oxide coat. Then the surface oxide layer appears to be subject to cracking and spalling as evidenced by sudden weight losses. Following this the weight of the sample increases, and the oxidation rate appears linear.

McCullough⁽¹⁶⁾ et. al., also found an initial parabolic rate which abruptly increased after a certain time. It was demonstrated that this increase was due to rupture of the initial layer. It was demonstrated in this study that an oxide consisting mainly of Fe_2O_3 grew fairly rapidly through the cracks in the spinel layer initially formed in the oxidation process.

4.2.4.2 Ablation

Table 4.13 lists the experimental ablation times and corrected heating rate values at each test run. Also listed are the integrated values of total re-entry

heat, \bar{Q}_r , and heat lost to radiation, \bar{Q}_{rad} . These values were used to determine the experimental heat needed to melt a sample, \bar{Q}_m . (For a discussion of the calculational procedures used in evaluating these quantities see Section 4.2.1.2). The average experimental value of 2200 cal agrees with the theoretical value of 2230 cal. Figures 4.18 and 4.19 show the features of the surface melting phenomena on a series of stainless steel samples at a heating rate of 122 cal/sec. The times required to achieve significant events are indicated.

4.2.4.3 Incomplete Ablation

It is interesting to note that in the case of stainless steel there is a heating rate range where incomplete ablation occurred. The term incomplete ablation refers to a partial melting of the hemisphere in the stagnation point region followed by a static period of long duration during which time no additional ablation or melting occurred. Following this long static period the sample underwent complete ablation.

Table 4.14 lists the experimental times and corrected heating rate values at each test run. Also listed are the integrated values of the total re-entry heat input, \bar{Q}_r , the integrated heat lost to radiation, \bar{Q}_{rad} , which values were used to determine the experimental heat needed to melt a sample, \bar{Q}_m . In all cases there was more than sufficient heat to ablate the sample, yet in all cases only the stagnation point area was melted, and the rest of the sample remained in the initial form for long time periods. Figures 4.20 and 4.21 show the features of the surface melting phenomena for incomplete ablation for a series of stainless steel samples at a heating rate of 102 cal/sec. The times of significant events are indicated.

Two observations may be made regarding those samples undergoing incomplete ablation. First, a rather thick rough layer appeared at the molten interface once melting began. This coating may be the result of a rapid oxidation of the molten layer. As has been noted (Section 2.1.2.4), the oxides of most metals melt at higher temperatures than do their metallic constituents. In addition, the thermal conductivities of oxides are lower than are those of metals. As a result heat transfer from the oxide surface to the metal may be sufficiently retarded to delay the melting of the metallic phase once oxidation has occurred.

Secondly, it can be noted in these figures that at the beginning of ablation a basic change occurred in sample geometry. The samples ceased to be hemispherical once ablation began and assumed an almost cylindrical shape. With this change in geometry there may very well be a change in the total heating rate of the sample. If the heating rate is diminished, then it is quite possible that the melting process will be delayed. To determine, if either of these two effects were important in influencing incomplete ablation, a series of experiments on both pre-oxidized samples and samples of cylindrical geometry were performed. The results of these tests follow.

4.2.4.4 Experimental Examination of Incomplete Ablation

4.2.4.4.1 Effect of Oxide Coat on Ablation

A number of stainless steel samples were pre-oxidized in a static system. Varying amounts of oxide were formed on the metallic surface. It was observed in the pretreatment experiments that two types of oxide coatings were formed:

- (1) Samples free of ruptures in the initial layer and tenacious in nature;
- (2) Samples where the oxide layer showed evidences of cracking and spalling.

Both types can be seen in Figure 4.22. Samples 16 and 12 are of Type II, and Sample 11 is of Type I.

The samples were then placed in the plasmajet facility, and the ablation times were compared with those of fresh, non-oxidized stainless steel samples tested under identical conditions. The results of these tests for three test points are shown in Table 4.15 in terms of type of oxide coating formed, oxide weight, and times for complete ablation.

It is evident from an examination of the data in Table 4.15 that, when the oxide coat is free from cracks and of a tenacious nature, (Type I), ablation is inhibited. Thus, as sample oxide weight increases, ablation time increases. In the case of oxide coatings of a Type II nature, the ablation process may in fact, be accelerated. This may be the result of spallation of the oxide coating.

4.2.4.4.2 Effect of Sample Geometry on Ablation

In this series of tests the ablation times of two types of sample geometry were compared: (1) the regular one-half inch hemisphere and (2) a one-half inch cylinder. Figure 4.23 shows both geometries tested. The weights of the samples were equal in both cases (7.83 grams). Samples of both geometries were placed in the plasmajet facility and were tested under identical conditions, and the ablation times were compared. The results of these tests are shown in Table 4.16, in terms of experimental ablation times and corrected heating rate values. Also listed are the integrated values of heat input, \bar{Q}_t , the integrated heat lost to radiation, \bar{Q}_{rad} , and the experimental heat needed to melt the sample, \bar{Q}_m .

At high heating rates (≈ 190 – 120 cal/sec) where complete ablation was previously found, geometry does have an effect on the ablation of stainless steel samples. The average experimental value of 3482 cal for cylindrical samples (special geometry) is higher than the average experimental value obtained for a hemisphere which is 2200 cal. At the lower heating rates (≈ 120 – 90 cal/sec), where incomplete ablation was previously found, there is no effect due to sample geometry. In both cases, there is a value of 4070 cal when the theoretical prediction is 2230 cal.

Since those test points resulting in complete ablation of hemispherical samples were the ones affected by changing geometry, it would appear that the heat flux to a cylindrical model is lower than that to a hemispherical model. On the other hand, in the case of those samples undergoing incomplete ablation, the samples were deformed to a cylindrical shape early in the melting process. (See Figure 4.20 and 4.21). Thus, it would appear that both the deformed hemispheres and the cylinders were being heated at the same rate and would require the same time for ablation to occur. The rate controlling step in the ablation of these samples was heat transfer to the cylindrical body. Thus to evaluate correctly the heat required to ablate the samples in the low heat flux region, it would be necessary to take into account the new heat flux resulting from changed geometry.

There does exist the possibility that a change in position of the stagnation point will change the heat required to melt the samples. By moving the sample a short distance back from the stagnation point the heating rate may be diminished, and the melting process delayed.

To check this effect, the cylindrically shaped samples were tested at two distances from the exit of the nozzle. The first distance is 0.56 inches which is the distance at which a hemisphere normally is located, and the second distance is 0.69 inches from the nozzle exit. The second distance is approximately that distance that a hemispherically shaped sample would be from the nozzle exit after it has undergone initial melting at the stagnation point area.

Table 4. 17 lists the experimental ablation times and corrected heating rate values at each test run. Also listed are the integrated values of heat input, \bar{Q}_t , the integrated heat lost to radiation, \bar{Q}_{rad} , and the experimental heat needed to melt a sample, \bar{Q}_m . The average experimental value for a distance of 0.69 inches is 3816 cal and is higher than the average experimental value obtained for the distance of 0.56 inches which is 3482 cal.

It is evident that the effect of change in position of the stagnation point is small in the case of stainless steel, but it should be considered in any exact analysis of experimental plasmajet data.

4.2.5 Inconel

The test points examined in the investigation of inconel are listed in Table 4. 18 in terms of experimentally measured stagnation pressures and enthalpies as well as simulated altitudes and velocities. The significant reactions observed are also listed.

4.2.5.1 Non-Ablative Phenomena

4.2.5.1.1 Steady State

Figure 4.24 shows the surface temperatures for a series of test points with varying heating rates. Table 4. 19 compares all the calculated steady state surface temperatures with those of actually measured temperatures. The calculated

and actual temperatures were corrected using a total hemispherical emissivity value of 0.95.

4.2.5.1.2 Oxidation

The oxidation rates of inconel were very low as would be expected. It is still not clear according to Kubaschewski and Hopkins⁽⁵⁾ as to what exactly determines the good oxidation resistance of nickel-chromium alloys. In all cases a maximum rate of 1.0×10^{-5} gram/sec is the extent of oxidation on the sample. Figure 4.25 is a typical oxidation curve, showing weight increase as a function of time. It was obtained at a heating rate of 60 cal/sec.

4.2.5.2 Ablation

Table 4.20 lists the experimental ablation times and corrected heating rate values at each test run. Also listed are the integrated values of heat input, \bar{Q}_t , the integrated heat losses to radiation, \bar{Q}_{rad} , and the experimental heat needed to melt a sample, \bar{Q}_m .

The average experimental value of 2130 cal is in agreement with the theoretical value of 1916 cal. Figures 4.26 and 4.27 show the features of the surface melting phenomena on a series of Inconel-X samples tested at a heating rate of 167 cal/sec. The times of significant events are indicated.

4.2.5.3 Incomplete Ablation

What was noted in the study of stainless steel was also observed in the case of Inconel-X, i.e., incomplete ablation was observed. Figures 4.28 and 4.29 show the features of the surface melting phenomena for incomplete ablation for a series of Inconel-X samples tested at a heating rate of 96 cal/sec. The times of significant events are noted.

In all cases there was more than sufficient heat to ablate the sample (Table 4.21 lists these data), yet the samples were initially deformed and ablation occurred only after considerable time had elapsed. The reasons proposed for this phenomenon are the same as those discussed in the case of stainless steel.

4.2.5.4 Experimental Examination of Incomplete Ablation

The same observations made in the examination of incomplete ablation of stainless steel may also be made in the case of Inconel-X ablation, i.e. both oxidation and changing geometry may be inhibiting the ablation process. To check these hypotheses a series of tests were performed.

4.2.5.4.1 Effect of Oxide Coat on Ablation

An attempt was made to pre-oxidize Inconel-X samples as was described in Section 4.2.4.4.1 for stainless steel. Due to the fact that Inconel-X is oxidation resistant, samples with small amounts of oxide weight were tested. In all cases, as is evident from the data in Table 4.22, no protection against ablation was afforded by the oxide coat.

4.2.5.4.2 Effect of Sample Geometry

The ablation times of cylindrical samples were compared with those of hemispherical ones as was done in the study of stainless steel (Section 4.2.4.4.2).

Table 4.23 lists the experimental ablation times and the corrected heating rate values at each run. Also listed are the integrated values of heat input, \bar{Q}_i , the integrated heat lost to radiation, \bar{Q}_{rad} , and the experimental heat needed to melt a sample, \bar{Q}_m .

What was noted in the study of stainless steel was also observed in the case of Inconel-X. At higher heating rates ($\approx 190 - 120$ cal/s) where complete ablation was previously found, geometry played an effect in the ablation of Inconel-X samples. The average experimental value of 4583 cal (cylindrical sample) is higher than the average experimental value obtained for a hemisphere which is 1920 cal.

At the lower heating rates ($\approx 120-100$ cal/sec) where incomplete ablation was previously found, there is no effect due to sample geometry in Inconel-X ablation. It is evident from the data in Table 4.23 that both samples tested at lower heat fluxes need the same amount of heat for complete ablation

to occur and that the heating process is the same in both cases. These results are completely in accord with those for stainless steel. Thus, it is suggested in the case of Inconel-X that initial deformation of the sample into a cylindrical shape results in a lowering of the heat flux to the sample and consequently an increase in time for complete ablation.

It was also observed that a change in the position of the stagnation point delayed the melting process. Table 4.24 lists pertinent experimental data obtained from tests on cylindrical Inconel-X samples at the two distances from the exit nozzle as described in Section 4.2.4.4.2. The average experimental value for samples set back a short distance is 4861 cal/s, which is higher than the average experimental value obtained for samples set at the regular distance, which is 4583 cal/s. These results are in accord with those for stainless steel. Thus, a change in position of the stagnation point causes a small change in heating rates.

4.2.6 Beryllium

The test points examined in the investigation of beryllium are listed in Table 4.25 in terms of experimentally measured stagnation pressures and enthalpies as well as simulated altitudes and velocities. The significant reactions are also listed.

4.2.6.1 Non-Ablative Phenomena

4.2.6.1.1 Steady State

Figure 4.30 shows the surface temperatures for a series of test points with varying heating rates. Table 4.26 lists all the calculated steady state temperatures (calculated according to equation 4.1) and the experimentally measured values. The calculated and actual temperatures were evaluated using a total hemispherical emissivity of 0.80.

4.2.6.1.2 Oxidation

The oxidation of beryllium was not a significant process and no oxidation - time curves are reported. In all cases a maximum rate of

1.0×10^{-5} grams/sec was observed.

4.2.6.2 Ablation

Figures 4.31 and 4.32 show the melting process of beryllium at a stagnation pressure of 0.150 atms. Figures 4.33 and 4.34 show the melting process of beryllium at a lower stagnation pressure of 0.025 atms.

Table 4.27 lists the experimental times for ablation and the corrected heating rate values at each test run. Also listed are the integrated values of total re-entry heat input, \bar{Q}_t , the integrated heat lost to radiation, \bar{Q}_{rad} , and the experimental heat required to melt the sample, \bar{Q}_m . (For a discussion of the calculational procedures used in evaluating these quantities see Section 4.2.1.1).

An examination of these data indicates that the heats of melting are not constant and in fact appear to increase with time of exposure. In all cases where the stagnation pressures are low ($\approx .027$ atms.), they are greater than the value theoretically predicted by equation (2.2). This value is 1755 cal/s. In the two cases where the stagnation pressure is high ($\approx .15$ atms.) the values are much closer to the theoretical value predicted. The fact that the value of \bar{Q}_m increases with increasing ablation time suggests heat loss to the boron nitride holder as in the case of aluminum and aluminum alloy. (For a discussion of the calculation procedures to be used in evaluating these quantities, see Section 4.2.2.1.)

A plot of \bar{Q}_m/t_m vs. $1/t_m$ was made (Figure 4.35). According to Section 4.2.2.1, this plot should result in a straight line, the slope of which should be equal to the net heat required to melt the sample and the intercept of which should be equal to the heating loss to the holder. An examination of the data shown in Figure 4.35 indicates a reasonably linear fit of experimental data points and a slope of 4220 cal/s which is higher than the theoretical value of 1755 cal/s. The intercept value of 25 cal/sec would appear to represent the heating rate to the holder.

Considering the intercept value of 25 cal/sec as the heat lost to the holder, the average value for \bar{Q}_m at the higher stagnation pressure (≈ 0.150

atms) is 1507 cal. This value for \bar{Q}_m is in agreement with the theoretical value of 1755 cal.

Since the values for \bar{Q}_m are high, the following experiment was carried out. In order to rule out the possibility of the existence of a protective oxide coating as in the case of titanium and stainless steel or the effect of changing geometry as in the case of Inconel-X and stainless steel, another plot was made. In this plot initial melting times were considered. Initial melting is considered to be that time when visual melting appears at the stagnation point. Samples Be 1 and Be 19 in Figures 4.32 and 4.34 are examples of samples undergoing initial melting. The pertinent experimental data obtained for initial melting are listed in Table 4.28. Once again \bar{Q}_{mi}/t_{mi} was plotted versus $1/t_{mi}$. An examination of the initial melt data shown in Figure 4.36 indicates the data do not fit nearly so well as in the case of Figure 4.35; however, the slope of 2650 cal is closer to agreement with the theoretical value of 1530 cal. From an examination of the data in Table 4.28 the average \bar{Q}_{mi} value of 1629 cal for samples tested at high stagnation pressures is in closer agreement with the theoretical value of 1530 cal. The high values for \bar{Q}_{mi} , therefore, cannot be attributed to the protective oxide or the special geometry effect which was found in the ablation of titanium, Inconel-X and stainless steel.

Since the protective oxide coating and special geometry effect have been ruled out as possible answers to the high \bar{Q}_m value, one other possibility exists. The history of beryllium metallurgy has been clouded by numerous and conflicting reports of phase changes in the temperature region of 1240-1260°C. Kuro, Jackson, Udy, and Eastwood⁽³⁷⁾ found no arrests in heating curve from the melting point to room temperature. On the other hand, Gold⁽³⁸⁾ has shown a heating curve, which has a pronounced step at just above 1240°C, but he attributed this to the presence of impurities. Buzzard⁽³⁹⁾ also found a pronounced arrest at $1250 \pm 10^\circ\text{C}$, which he thought indicated a phase change. The weight of evidence from most of the literature is definitely in favor of the existence of a phase change in the region 1240-1260°C. This phase change may offer one explanation for the high \bar{Q}_m values obtained in the tests. It is not possible to present a clear answer to exactly how much this phase change has contributed to the

excess heat required in the initial melting process. Much more work is needed before anything positive can be said about the allotrope effect on the ablation process of beryllium.

The high values for \bar{Q}_m for complete ablation can be explained much like the incomplete ablation found in the tests of stainless steel and Inconel-X. The beryllium undergoes a change in geometry over the range of heating rates. The samples become flat-faced and then become essentially cylindrical in shape. As with Inconel-X and stainless steel, the change in geometry changes the heating rate process by changing the total heat to the sample. Thus, the experimental value for \bar{Q}_m will be higher than the theoretical value predicted for beryllium ablation.

With the change in geometry, there is also a change in position of the stagnation point. It has been proven from previous tests with Inconel-X and stainless steel that a delay in the melting process occurs. Though it may be small it must be considered as another possible explanation for the high \bar{Q}_m values obtained in the ablation of beryllium.

5.0 CONCLUSIONS

As a result of the experimental findings of this investigation the following conclusions may be drawn:

- 1) In the case of the ablation of aluminum, aluminum alloy, and titanium the process of ablation is determined entirely by the melting process, i.e., the energy required to ablate is simply equal to

$$\bar{Q}_m = W \left(\int C_p dT + \Delta H_m \right)$$

\bar{Q}_m = the heat required to ablate a material, cal

W = the weight of the sample, g

C_p = the heat capacity function, cal/°C-g

T = temperature, °C

ΔH_m = the heat of melting, cal/g

- 2) The oxidation of all materials studied appears at least in a qualitative sense to be similar to that obtained by investigators in static systems.
- 3) In the case of titanium and stainless steel, the presence of a thick tenacious oxide coat on the sample's surface will inhibit ablation. In the case of stainless steel, the ablation process may be accelerated if the oxide coating shows evidences of cracks and spallation.
- 4) Inconel-X and stainless steel behave similarly to aluminum, aluminum alloy, and titanium at high heating rates. At low heating rates, however, these materials undergo a phenomena which has been termed "incomplete ablation."

In addition, it was also noted in the case of the ablation of beryllium, much more heat was required for ablation to occur than was theoretically predicted.

BIBLIOGRAPHY

- (1) W. S. Brown, "WANL Source Term Program Status Report - Volume I of II" - WANL-TME-796, May 1964 (CRD).
- (2) S. W. Benson, The Foundations of Chemical Kinetics, McGraw Hill Book Company, Inc., New York, (1960).
- (3) F. Seitz, The Physics of Metals, McGraw-Hill Book Company, New York, (1943).
- (4) S. Dushman, Scientific Foundations of Vacuum Technique, John Wiley and Sons, Inc., New York, (1962).
- (5) O. Kubaschewski and B. E. Hopkins, "Oxidation of Metals and Alloys", Academic Press, Inc., London (1962).
- (6) E. A. Gulbransen and W. S. Wyson, J. Phys. Chem. 51, 1087 (1947).
- (7) W. W. Smeltzer, J. Electrochem. Soc, 103, 209 (1956).
- (8) D. W. Aylmore, S. J. Gregg and W. B. Jepson, J. Institute of Metals 88, 205 (1959)
- (9) C. N. Cochran and W. C. Sleppy, J. Electrochem. Soc. 108, 323 (1961).
- (10) W. A. Alexander and L. M. Pidgeon, Canadian J. of Research 28B, 60 (1950).
- (11) J. T. Waber, G. E. Sturdy, and E. N. Wise, J. Am. Chem. Soc. 75, 2269 (1953).
- (12) E. A. Gulbransen and K. F. Andrews, J. Electrochem. Soc. 98, 241 (1951).
- (13) M. H. Davies and C. E. Birchenall, J. Metals, N. Y. 3, 877 (1951).
- (14) A. E. Jenkins, J. Inst. Metals 82, 213 (1953).
- (15) P. Kofstad and K. Hauffe, Werkstoffe u Corrosion 7, 642-9 (1956).

- (16) H. M. McCullough, Ohio State University Engineering Experiment Station News, 16, 38 (1947).
- (17) W. E. Campbell and A. B. Thomas, Trans. Electrochem. Soc. 91, 623 (1947).
- (18) D. Caplan and M. Cohen, Corrosion 15, 141t (1959).
- (19) H. M. McCullough, M. G. Fontana, and F. H. Beck, Trans. of Am. Soc. for Metals 43, 404-425 (1951).
- (20) O. Kubaschewski and O. von Goldbeck, Z. Metallk. 39, 158 (1948).
- (21) S. F. Frederick and I. Cornet, J. Electrochem. Soc. 102, 285 (1955).
- (22) G. E. Zima, Trans. Amer. Soc. for Metals 49, 924, (1957).
- (23) E. A. Gulbransen and K. F. Andrews, J. Electrochem. Soc. 104, 451 (1957).
- (24) E. A. Gulbransen and K. F. Andrews, J. Electrochem. Soc. 97, 323, (1950).
- (25) E. A. Gulbransen and K. F. Andrew, J. Metals, New York 1, 515 (1949).
- (26) E. A. Gulbransen and K. F. Andrews, Trans. Electrochem. Soc., 97, 383, (1950).
- (27) J. A. Fay and F. R. Riddell, J. Aeronautical Sciences 25, 73, (1958).
- (28) R. F. Probstein and N. H. Kemp, J. Aeronautical and Space Science, (March 1960) 174.
- (29) A. Ferri, V. Zakkay and L. Ting, J. of Aerospace Sciences, (December 1961) 962.
- (30) N. H. Kemp, P. H. Rose, and R. W. Detra, J. of Aerospace Sciences, (July 1959) 421
- (31) American Society for Testing Materials, Batelle M. I.
- (32) M. R. Trammell, Private Communications, WANL

- (33) Handbook of Chemistry and Physics, 44th Edition, Chemical Rubber Publishing Company, Cleveland, Ohio (1963).
- (34) W. R. Wade, "Measurements of Total Hemispherical Emissivity of Various Oxidized Metals at High Temperatures", NACA-TN-4206, March 1958.
- (35) W. J. O' Sullivan and W. R. Wade, "Theory and Apparatus for Measurements of Emissivity for Radiative Cooling of Hypersonic Aircraft with Data for Inconel, Inconel - X, Stainless Steel 303, and Titanium Alloys RS-120", NASA-TR-R-90, 1961.
- (36) D. W. White, Jr. and J. E. Burke, The Metal Beryllium, American Society for Metals, Cleveland, Ohio, (1955).
- (37) J. G. Kura, J. H. Jackson, M. C. Udy, and L. W. Eastwood, Trans. Amer. Inst. Min. (metall.) Engrs., 185, 769, (1949).
- (38) L. Gold, U. S. Atom. En. Comm. Rep. No. AECD-2643 (1949).
- (39) R. W. Buzzard, J. Res. nat. Bur. Stand., 50, 63, (1953)
- (40) American Society for Metals, Metals Handbook Volume 1, 8th Edition, Metals Park Ohio, (1961).
- (41) U. S. Atomic Energy Commission Report ANL-5750.
- (42) D. Cubicciotti, J. Am. Chem. Soc. 72, 2084 (1950).
- (43) D. W. Aylmore, S. J. Gregg, and W. P. Jepson, J. Nuclear Materials 2, 169 (1960).

TABLE 2.1
SUBLIMATION RATES OF TYPICAL SOLIDS
AT THEIR MELTING POINTS

Solid	Melting Point (°C)	Sublimation Rate (g/cm ² -sec)*
Al	659	< 10 ⁻⁸
Ti	1670	~ 10 ⁻⁴
Fe	1539	~ 10 ⁻⁴
Ni	1452	~ 10 ⁻⁴
Be	1285	~ 10 ⁻⁴

* These data represent approximate values of sublimation rates as reported in Table 10.1 of Reference (4). For a comprehensive report on sublimation, the reader is referred to this volume.

TABLE 2.2
THERMODYNAMIC HEAT DATA OF TYPICAL SOLIDS

Materials	Melting Point (°C)	$T \int_{T_i}^T C_p dT$ (cals/g)	ΔH_m (cals/g)	Density (g/cc 20°C)
Aluminum	659 ⁽⁴⁰⁾	210 ⁽⁴¹⁾	94 ⁽³³⁾	2.70 ⁽⁴⁰⁾
*Aluminum Alloy	643 ⁽⁴⁰⁾	210 ⁽⁴¹⁾	94 ⁽³³⁾	2.82 ⁽⁴⁰⁾
Stainless Steel	1450 ⁽⁴⁰⁾	254 ⁽⁴¹⁾	65 ⁽⁴⁰⁾	7.90 ⁽⁴⁰⁾
Inconel X	1410-1450 ⁽⁴⁰⁾	195 ⁽⁴¹⁾	68 ⁽³³⁾ **	8.51 ⁽⁴⁰⁾
***Titanium Alloy	1670 ⁽⁴⁰⁾	284 ⁽⁴¹⁾	104 ⁽³³⁾	4.46 ⁽⁴⁰⁾
Beryllium	1285 ⁽³⁶⁾		250/275 ⁽³⁶⁾	1.85 ⁽³⁶⁾

*The information obtained is for an Aluminum Alloy with a composition of 6% Cu and 93% Al.

**The information obtained is for an Inconel Alloy with a composition of 76% Ni, 16% Cu and 8% Fe.

***The information obtained is for Titanium Alloy with a composition of 5% Al, 2.5% Sn and 72.5% Titanium.

****The heat of fusion of Inconel was calculated based on the relative values of ΔH_m of the components of the alloy.

TABLE 2.3
 SOME THERMAL PROPERTIES OF OXIDES
 FORMED DURING RE-ENTRY

Material	Probable Oxides Formed	ΔH (Decomposition) (kcal/mole)	Melting Point (°C)
Aluminum	Al_2O_3	266.8	2030
Titanium	Ti_5O_9 (rutile)	176.2	1920
Stainless Steel	$FeCr_2O_4$	8.2	2180
	FeO	126.5	1424
	Cr_2O_3	180.0	2400
Inconel	$NiCr_2O_4$	2.0	----
	NiO	115.0	1960
	Cr_2O_3	180.0	2400
Beryllium	BeO	286.2	2530

All data were taken from Reference (5).

TABLE 2.4
EMISSIONS OF TYPICAL SOLIDS

Material	Total Hemispherical Emissivity*							
	Fresh Sample	Temperature (°C)						
		316	445	555	820	1000	1200	1400
Aluminum	0.34	0.39	0.395	0.40	----	----	----	----
Titanium	0.26	0.54	0.54	0.54	0.60	0.67	0.69	0.71
Stainless Steel (300 Series)	0.30	0.69	0.71	0.74	0.78	0.82	0.83	0.85
Inconel-X	0.30	0.89	0.89	0.895	0.91	0.92	0.925	0.95
Titanium Alloy (RS-120)	0.26	0.66	0.68	0.69	0.71	----	----	----
Stainless Steel	0.30	0.75	0.775	0.80	0.85	0.87	0.87	0.87
Inconel	0.30	0.75	0.775	0.80	0.84	0.86	0.86	0.86
Beryllium	0.35	0.55	0.55	0.55	0.67	0.71	0.82	0.85

* Measurements of total normal emissivity were made on specimens oxidized for 30 minutes or longer to insure a stable surface condition. Total hemispherical emissivity = total emissivity measured in all directions from surface over the entire solid angle of a hemisphere.

All data were taken from References (34) and (35).

TABLE 3.1
 SUMMARY OF STAGNATION POINT HEAT TRANSFER DATA
 (ONE INCH CALORIMETER)

Test Point	Enthalpy (Btu/lb)	Pressure (atms)	q_{s2} (cal/cm ² sec)	Reynolds Number
1	2,500	0.0308	49.4	210
2	9,300	0.0325	139	98.4
4	6,680	0.0149	71.8	57.8
5	12,550	0.0299	180	88.2
7	12,250	0.0129	80.0	36.5
8	12,300	0.00712	36.85	20.9
9	12,350	0.00423	14.65	10.4
10	6,490	0.0109	44.15	37.9
11	12,450	0.0208	179	56.6
12	805	0.0560	5.24	971
13	790	0.0106	2.12	194
14	1,160	0.0125	10.75	117
15	1,325	0.0960	37.65	954
17	2,070	0.146	81.0	1040
18	2,020	0.0194	25.9	141
19	2,470	0.00800	3.78	51.9
20	3,070	0.150	107	917
21	2,820	0.0623	68.5	588
22	1,305	0.177	67.7	1390
23	1,775	0.0720	49.0	602
24	2,090	0.0790	54.1	600
25	2,220	0.0856	67.7	641

TABLE 3.2
SUMMARY OF TOTAL HEAT TRANSFER DATA
(ONE-HALF INCH CALORIMETER)

Test Point	Enthalpy (Btu/lb)	Press (atms)	\dot{q}_t (cals/sec)	Reynolds Number
1	3,010	0.0313	78.7	105
2	9,300	0.0310	182	49.2
4	6,750	0.0153	104	28.9
5	12,100	0.0280	188	44.1
7	11,600	0.0131	81.0	18.3
8	12,400	0.00720	51.2	10.5
9	11,400	0.00420	17.7	5.20
10	6,880	0.0110	68.0	19.0
11	12,900	0.0206	190	28.3
12	1,020	0.0557	19.8	485
13	836	0.0104	8.10	97.0
14	1,300	0.0127	18.7	58.5
15	1,440	0.0103	58.9	477
17	2,100	0.149	123	522
18	1,980	0.0187	36.1	71.0
19	2,175	0.00780	14.9	26.0
20	2,610	0.150	152	458
21	3,000	0.0630	136	294
22	1,335	0.170	71.1	695
23	1,750	0.0720	63.0	301
24	2,000	0.0787	70.6	300
25	2,030	0.0850	81.8	321

TABLE 4.1
COMPOSITION OF METALS AND ALLOYS

<u>Metal</u>	
Aluminum Alloy 2219 - T852	
	<u>percent</u>
Copper	5.8-6.8
Iron	0.30 (max)
Manganese	0.20-0.40
Silicon	0.20 (max)
Zirconium	0.10-0.25
Zinc	0.10 (max)
Vanadium	0.05-0.15
Titanium	0.02-0.10
Magnesium	0.02 (max)
Aluminum	Remainder (93%)

Stainless Steel 304-A

	<u>percent</u>
Iron	69.0
Chromium	18.0-20.0
Nickel	8.0-11.0
Manganese	2.0
Silicon	0.8

Inconel X-750

	<u>percent</u>
Nickel	70.0 (min)
Chromium	14.0-17.0
Iron	5.0-9.0
Aluminum	0.40-1.00
Titanium	2.25-2.75
Columbium	0.70-1.20
Cobalt	0.20 (max)
Copper	0.50 (max)
Manganese	1.20 (max)
Silicon	0.50 (max)
Carbon	0.08 (max)

<u>Metal</u>	<u>percent</u>
Titanium Alloy A 110-AT (Extra Low Interstitial)	
Titanium	Remainder
Aluminum	4.75-5.75
Tin	2.20-2.80
Hydrogen	0.015 (max)
Iron	0.25 (max)
Oxygen	0.12 (max)
Carbon	0.050 (max)
Nitrogen	0.040 (max)
Boron	0.010 (max)
Others (Each)	0.10 (max)
Others (Total)	0.40 (max)

Aluminum 6061-T-6

	<u>percent</u>
Magnesium	0.8-1.2
Silicon	0.40-0.8
Copper	0.15-0.40
Iron	--- -0.7
Chromium	0.15-0.35
Zinc	0.25 (max)
Titanium	0.15 (max)
Manganese	0.15 (max)
Other Elements (Each)	0.05 (max)
Other Elements (Total)	0.15 (max)
Aluminum	Remainder

Beryllium

	<u>percent</u>
Beryllium Assay	98.0 min
Beryllium Oxide	2.00 max
Iron	0.20 max
Aluminum	0.18 max
Carbon	0.15 max
Magnesium	0.08 max
Silicon	0.12 max
Others (each)	0.04 max

TABLE 4.2
SUMMARY OF TITANIUM TEST POINTS

Test Point	Stagnation Enthalpy (Btu/lb)	Stagnation Press. (Atmospheres)	Altitude (ft)	Simulated Velocity (ft/sec)	Observed Reaction
2	9,000	0.0310	230,000	21,100	Ablation
5	12,400	.0300	240,000	25,000	"
11	12,400	.0208	250,000	25,000	"
17	2,000	.150	150,000	10,000	"
20	2,955	.151	150,000	12,000	"
10	6,000	.01075	250,000	18,000	Oxidation
4	6,500	.0151	240,000	18,000	"
11	11,800	.0208	250,000	25,000	"
15	1,280	.100	150,000	8,000	"
9	12,750	.00445	280,000	25,000	"
21	2,960	.0633	200,000	12,000	"
1	2,720	.0313	200,000	11,250	"
26	2,940	.1005	200,000	12,500	"

TABLE 4.3
SUMMARY OF TITANIUM STEADY STATE DATA

Test Point	Heating Rate (cal/sec)	Calculated Temp(°C)	Measured Temp (°C)
10	65.5	1550	1580
4	104	1760	1700
9	19.5	1070	1040
15	41.6	1350	1210
21	110	1800	1700
1	69.3	1570	1350
26	102	1760	1700

TABLE 4.4
SUMMARY OF TITANIUM OXIDATION DATA

Test Point	Heating Rate Corrected (cal/sec)	Temperature (°C)	Rate (g /sec)	Type
9	17.7	1050	$.0400 \times 10^{-4}$	Linear
15	41.6	1175-1300	$.720 \times 10^{-4}$	Linear
10	55.0	1500-1600	1.20×10^{-4} to 4.00×10^{-5}	Parabolic *
1	69.0	1500-1600	2.00×10^{-4} to 1.77×10^{-4}	Parabolic *
17	92.0	1600	6.40×10^{-4} to 2.71×10^{-4}	Parabolic *
4	95.0	1600	3.40×10^{-4} to 1.71×10^{-4}	Parabolic *
26	102	1600	9.70×10^{-4} to 5.30×10^{-4}	Parabolic *
21	110	1600	8.09×10^{-4} to 3.90×10^{-4}	Parabolic *

* In the case of Parabolic rate data the oxidation rate range as reported represents the range from the initial rate which is the maximal one to the final rate which is the minimal one.

TABLE 4.5
SUMMARY OF TITANIUM ABLATION DATA

Run Number	Test Point	Heating Rate Corrected (cal/sec)	Ablation Time (sec)	\bar{Q}_t (cals)	\bar{Q}_{rad} (cals)	\bar{Q}_m (cals)
262	11	166	10.0	1660	204	1460
385	20	140.5	15.0	2110	505	1600
307	20	129	13.5	1740	505	1240
308	11	160	16.0	2560	937	1620
273	2	177.5	13.0	2310	592	1720
311	2	167	11.2	1870	566	1300
293	5	183	8.8	1620	453	1170
294	5	187	7.1	1330	262	1070
322	17	115	30.8	3540	1300	2240
323	17	115	30.8	3540	1650	1890

\bar{Q}_m Theory = 1450 cals

\bar{Q}_m Experimental (avg) = 1530 ± 284 cals

TABLE 4.6
EFFECT OF OXIDE COAT ON TIME FOR COMPLETE
ABLATION OF TITANIUM SAMPLES

Run Number	Test Point	Heating Rate Corrected (cal/sec)	Sample No.	Oxide Wt. (g)	t_m (sec)
439	27	93.5	Ti 76	0.0000	33.6
			Ti 77(28)	0.0550	> 179.9 *
			Ti 78(25)	0.1270	> 184.9 *
			Ti 79(26)	0.2270	> 180.8 *
441	27	120	Ti 80	0.0000	18.7
			Ti 81(21)	0.0500	24.9
			Ti 82(22)	0.1050	42.9
			Ti 83(29)	0.1960	41.2
385	20	140	Ti 70	0.0000	15.0
			Ti 71	0.0000	15.3
			Ti 69-2	0.0383	16.5
			Ti 67-2	0.1258	44.0
435	20	142	Ti 72	0.0000	10.2
			Ti 73(27)	0.0500	12.5
			Ti 74(24)	0.1260	25.4
			Ti 75(23)	0.2060	25.1

* Samples had not ablated at these times.

TABLE 4.7
SUMMARY OF ALUMINUM TEST POINTS

Test Point	Stagnation Enthalpy (BTU/lb)	Stagnation Press. (Atmospheres)	Simulated Altitude (Ft.)	Simulated Velocity (Ft./sec)	Observed Reaction
9	12,750	0.00445	280,000	25,000	Ablation
10	6,000	.01075	250,000	18,000	"
15	1,280	.100	150,000	8,000	"
12	750	.0560	150,000	6,000	"
13	750	.0100	200,000	6,000	Sublimation
14	1,250	.0125	200,000	8,000	Ablation
18	2,000	.0195	200,000	10,000	"
21	2,960	.0633	200,000	12,000	"
22	1,335	.107	139,000	8,000	"
23	1,750	.0720	174,000	9,500	"
24	2,000	.0787	168,000	10,000	"
25	2,030	.0850	166,000	10,000	"

TABLE 4.8
SUMMARY OF ALUMINUM ABLATION DATA

Run Number	Test Point	Heating Rate Corrected (cal/sec)	Ablation Time (sec)	\bar{Q}_t (cals)	\bar{Q}_{rad} (cals)	\bar{Q}_m (cals)
333	21	122	7.7	943	18.0	925
364 B	25	66.0	16.4	1080	39.0	1040
366	10	59.4	27.5	1630	65.0	1570
364 A	24	56.9	22.0	1250	52.0	1200
363	22	50.0	27.0	1350	63.0	1290
364	23	49.6	27.8	1390	65.0	1325
360	15	44.0	27.0	1190	63.0	1120
359	18	29.4	73.0	2145	171	1970
376	9	15.8	126.6	2000	296	1700
356	14	13.9	228.0	3165	536	2630
362	12	13.8	180.0	2485	422	2060

\bar{Q}_m Theory 770 cals

Table 4.9

SUMMARY OF ALUMINUM ALLOY TEST POINTS

Test Point	Stagnation Enthalpy (Btu/lb)	Stagnation Press. (atmospheres)	Altitude (ft)	Simulated Velocity (ft/sec)	Observed Reaction
9	12,750	0.00445	280,000	25,000	Ablation
10	6,000	.01075	250,000	18,000	"
15	1,280	.100	150,000	8,000	"
12	750	.0560	150,000	6,000	"
13	750	.0100	200,000	6,000	Sublimation
14	1,250	.0125	200,000	8,000	Ablation
18	2,000	.0195	200,000	10,000	"
21	2,960	.0633	200,000	12,000	"
22	1,335	.107	139,000	8,000	"

TABLE 4.10
SUMMARY OF ALUMINUM ALLOY ABLATION DATA

Run Number	Test Point	Heating Rate Corrected (cal/sec)	Ablation Time (sec)	Q_t (cals)	Q_{rad} (cals)	Q_m (cals)
332	21	121	8.0	967	19.0	948
366	10	64.2	32.0	2045	75.0	1970
363	22	44.9	24.5	1100	58.0	1045
361	15	41.7	42.0	1750	99.0	1650
358	18	28.3	87.0	2460	205	2260
377	9	15.8	140.0	2210	330	1880
357	14	15.1	230.0	3475	541	2930
331	12	13.8	215.0	2965	506	2460

TABLE 4.11
SUMMARY OF STAINLESS STEEL TEST POINTS

Test Point	Stagnation Enthalpy (Btu/lb)	Stagnation Press. (atmospheres)	Altitude (ft)	Simulated Velocity (ft/sec)	Observed Reaction
9	12,400	0.00430	280,000	25,000	Sublimation
10	6,500	.0108	250,000	18,000	Oxidation
4	6,500	.0150	240,000	18,000	Oxidation
11	12,400	.0208	250,000	25,000	Ablation
17	2,000	.150	150,000	10,000	(I) * Ablation
2	9,000	.0310	230,000	21,000	Ablation
15	1,250	.100	150,000	8,000	Ablation
20	2,955	.151	150,000	12,000	Ablation
5	12,400	.0300	240,000	25,000	Ablation
21	2,960	.0633	200,000	12,000	(I) * Ablation
26	2,940	.1005	200,000	12,500	(I) * Ablation

* Where the term I refers to incomplete ablation.

TABLE 4.12
SUMMARY OF STAINLESS STEEL STEADY STATE DATA

Test Point	Heating Rate (cal/sec)	Calculated Temp (°C)	Measured Temp (°C)
10	60.0	1480	1375
4	92.6	1680	1600
17	80.5	1560	1350
9	19.5	1050	1000

TABLE 4. 13
SUMMARY OF STAINLESS STEEL ABLATION DATA

Run Number	Test Point	Heating Rate Corrected (cal/sec)	Ablation Time (sec)	\bar{Q}_t (cals)	\bar{Q}_{rad} (cals)	\bar{Q}_m (cals)
221	11	182	18.0	3290	371	2920
222	11	182	14.0	2560	302	2260
264	11	170	18.0	3060	540	2520
265	11	169	14.0	2365	425	1940
276	2	168	14.0	2355	593	1760
291	20	126	32.0	4045	1170	2880
292	20	122	32.0	3905	1320	2585
310	2	131	11.0	1440	400	1040
313	5	175	8.0	1440	382	1060

\bar{Q}_m Theory = 2230 cals

\bar{Q}_m Experimental (avg) = 2200 cal \pm 570 cals

TABLE 4.14
SUMMARY OF STAINLESS STEEL INCOMPLETE ABLATION DATA

Run Number	Test Point	Heating Rate Corrected (cal/sec)	Ablation Time (sec)	\bar{Q}_t (cals)	\bar{Q}_{rad} (cals)	\bar{Q}_m (Inc.) (cals)
321	21	102	145.0	14,800	8,320	6,480
355	21	109	100.0	10,900	5,730	5,170
383	21	113	90.0	10,150	5,160	4,990
322	17	119	126.0	15,000	7,220	7,780
323	17	111	116.0	12,900	6,650	6,250
384	26	99.0	65.0	6,430	2,360	4,070

Theoretical heat needed to melt sample = 2230 cals

TABLE 4.15
EFFECT OF OXIDE COAT ON TIME FOR COMPLETE ABLATION
OF STAINLESS STEEL SAMPLES

<u>Run Number</u>	<u>Test Point</u>	<u>Heating Rate Corrected (cals/sec)</u>	<u>Sample No.</u>	<u>Oxide Type</u>	<u>Oxide Wt. (g)</u>	<u>t_m (secs)</u>
436	20	148	SS 102	none	0.0000	27.5
			SS 103(14)	2	0.0670	25.4
			SS 104(15)	1	0.2010	35.8
			SS 105(13)	1	0.2780	43.5
443	27	115	SS 110	none	0.0000	48.4
			SS 111(16)	2	0.3490	38.8
			SS 112(11)	1	0.3430	82.8
			SS 113(12)	2	0.3170	48.9
440	27	98.6	SS 106	none	0.0000	141.3
			SS 107(19)	2	0.1220	84.4
			SS 108(18)	2	0.2550	50.7
			SS 109(17)	2	0.3270	56.8

Oxide Type (1) Oxide layer is free of ruptures of the initial layer and tenacious in nature.

Oxide Type (2) Oxide layer shows evidence of cracking and spalling.

TABLE 4.16
ABLATION OF STAINLESS STEEL SAMPLES OF CYLINDRICAL
GEOMETRY VS. REGULAR HEMISPHERES

<u>Run Number</u>	<u>Test Point</u>	<u>Sample Shape</u>	<u>Heating Rate Corrected (cals/sec)</u>	<u>t_m (sec)</u>	<u>\bar{Q}_t (cals)</u>	<u>\bar{Q}_{rad} (cals)</u>	<u>\bar{Q}_m (cals)</u>
(High Heating Rate)							
222	11	Hem.	182	14.0	2560	302	2260
421	11	Cyl.	191	21.4	4100	500	3600
292	20	Hem.	122	32.0	3905	1320	2585
434	20	Cyl.	125	32.4	4060	626	3430
\bar{Q}_m Theory = 2230 cals \bar{Q}_m Exp. Hem. = 2200 cals (See Table 4.13) \bar{Q}_m Exp. Cyl. = 3480 cals							
(Low Heating Rate)							
384	26	Hem.	99.0	65.0	6430	2360	4070
423	27	Cyl.	97.2	63.0	6120	2051	4070
\bar{Q}_m Theory = 2230 cals							

TABLE 4.17
 EFFECTS OF SAMPLE POSITION ON ABLATION OF
 STAINLESS STEEL SAMPLES

<u>Run Number</u>	<u>Test Point</u>	<u>Position</u>	<u>Heating Rate Corrected (cal/sec)</u>	<u>t_m (sec)</u>	<u>\bar{Q} (cal)</u>	<u>\bar{Q}_{rad} (cal)</u>	<u>\bar{Q}_m (cal)</u>
421	11	Reg.	191	21.4	4100	500	3600
421	11	1/8" back	191	23.2	4445	500	3945
434	20	Reg.	125	32.4	4060	626	3430
434	20	1/8" back	125	32.4	4060	626	3430
423	27	Reg.	97.2	52.5	5100	1690	3410
423	27	1/8" back	97.2	63.0	6120	2050	4070

\bar{Q}_m Theory = 2230 cal/s

\bar{Q}_m Exp. (Reg.) = 3480 cal/s

\bar{Q}_m Exp. (1/8" back) = 3820 cal/s

TABLE 4.18
SUMMARY OF INCONEL TEST POINTS

Test Point	Stagnation Enthalpy (Btu/lb)	Stagnation Press. (atmospheres)	Altitude (ft)	Simulated Velocity (ft/sec)	Observed Reaction
10	6,500	0.0108	250,000	18,000	Oxidation
4	6,500	.0150	240,000	18,000	Oxidation
17	2,000	.150	150,000	10,000	(I) * Ablation
15	1,250	.100	150,000	8,000	Sublimation
21	2,875	.0359	200,000	12,000	(I) * Ablation
26	2,940	.1005	200,000	12,500	(I) * Ablation
2	9,000	.0310	230,000	21,180	Ablation
18	2,000	.0195	200,000	10,000	Sublimation
8	12,400	.00750	270,000	25,000	Oxidation
9	12,400	.00430	280,000	25,000	Oxidation
20	2,875	.150	150,000	12,000	Ablation
11	12,400	.0208	250,000	25,000	Ablation

* Where the term I refers to incomplete ablation.

TABLE 4.19

SUMMARY OF INCONEL STEADY STATE DATA

Test Point	Heating Rate (cal/sec)	Calculated Temp(°C)	Measured Temp (°C)
10	65.5	1480	1350
15	37.4	1240	1080
18	31.3	1170	1100
9	16.3	957	956
4	95.0	1640	1415
8	48.1	1340	1200

TABLE 4.20
SUMMARY OF INCONEL ABLATION DATA

Run Number	Test Point	Heating Rate Corrected (cals/sec)	Ablation Time (sec)	\bar{Q}_t (cals)	\bar{Q}_{rad} (cals)	\bar{Q}_m (cals)
312	2	171	14.0	2395	453	1940
274	2	167	18.0	3010	667	2340
309	11	176	20.0	3520	976	2540
363	11	180	20.0	3615	976	2640
313	5	178	12.0	2135	726	1410
307	20	139	19.0	2650	702	1950

\bar{Q}_m Theory = 1920 cals

\bar{Q}_m Experimental (avg) = 2170 cals \pm 370 cals

TABLE 4.21
SUMMARY OF INCONEL INCOMPLETE ABLATION DATA

Run Number	Test Point	Heating Rate Corrected (cal/sec)	Ablation Time (sec)	\bar{Q}_t (cals)	\bar{Q}_{rad} (cals)	\bar{Q}_m (inc.) (cals)
322	17	132	60.0	7,920	2165	5755
288	17	121	120.0	14,500	6010	8520
321	21	112	96.0	10,750	1710	9040
383	21	123	77.0	9,500	1600	7900
384	26	109	58.0	6,320	2045	4275

Theoretical heat needed to melt sample = 1920 cals

TABLE 4. 22
EFFECT OF OXIDE COAT ON TIME FOR COMPLETE
ABLATION OF INCONEL SAMPLES

<u>Run Number</u>	<u>Test Point</u>	<u>Heating Rate Corrected (cal/sec)</u>	<u>Sample No.</u>	<u>Oxide Wt. (g)</u>	<u>t_m (sec)</u>
437	20	157	I-X 69	0.0000	30.3
			I-X 70(1)	0.0125	28.4
			I-X 71(3)	0.0135	32.2
			I-X 72(2)	0.0155	30.5
442	27	126	I-X 75	0.0000	55.3
			I-X 76(4)	0.0170	40.0
			I-X 77(6)	0.0120	39.0
			I-X 78(5)	0.0135	39.0

TABLE 4.23
 ABLATION OF INCONEL SAMPLES OF CYLINDRICAL
 SHAPE VS. HEMISPHERICAL SHAPE

<u>Run Number</u>	<u>Test Point</u>	<u>Sample Shape</u>	<u>Heating Rate Corrected (cals/sec)</u>	<u>t_m (sec)</u>	<u>\bar{Q}_t (cals)</u>	<u>\bar{Q}_{rad} (cals)</u>	<u>\bar{Q}_m (cals)</u>
(High Heating Rate)							
363	11	Hem.	180	20.0	3615	976	2640
421	11	Cyl.	193	27.4	5320	1000	4320
307	20	Hem.	139	19.0	2650	702	1950
434	20	Cyl.	135	34.3	4640	645	3995

$$\bar{Q}_m \text{ Theory} = 1920 \text{ cals}$$

$$\bar{Q}_m \text{ Exp. (Hem.)} = 2170 \text{ cals}$$

$$\bar{Q}_m \text{ Exp. (Cyl.)} = 4580 \text{ cals}$$

(Low Heating Rate)

438	27	Hem.	109	57.3	6250	717	5530
438	27	Cyl.	109	51.6	5640	607	5030
423	27	Cyl.	106	65.7	6980	2000	4980

$$\bar{Q}_m \text{ Theory} = 1920 \text{ cals}$$

$$\bar{Q}_m \text{ Exp (Hem.)} = 5530 \text{ cals}$$

$$\bar{Q}_m \text{ Exp (Cyl.)} = 5010 \text{ cals}$$

TABLE 4.24
EFFECTS OF SAMPLE POSITION ON ABLATION OF INCONEL SAMPLES

<u>Run Number</u>	<u>Test Point</u>	<u>Position</u>	<u>Heating Rate Corrected (cals/sec)</u>	<u>t_m (sec)</u>	<u>\bar{Q}_t (cals)</u>	<u>\bar{Q}_{rad} (cals)</u>	<u>\bar{Q}_m (cals)</u>
421	11	Reg.	193	27.4	5320	1000	4320
421	11	1/8" back	193	31.0	6020	1000	5020
434	20	Reg.	135	34.3	4640	645	3995
434	20	1/8" back	135	38.4	5185	792	4390
438	27	Reg.	109	51.6	5640	607	5030
423	27	Reg.	106	65.7	6980	2000	4980
423	27	1/8" back	106	69.0	7330	2160	5170

$$\bar{Q}_m \text{ Theory} = 1920 \text{ cals}$$

$$\bar{Q}_m \text{ (Exp. Reg.)} = 4580 \text{ cals}$$

$$\bar{Q}_m \text{ (Exp. 1/8" back)} = 4860 \text{ cals}$$

TABLE 4.25
SUMMARY OF BERYLLIUM TEST POINTS

Test Point	Stagnation Enthalpy (Btu/lb)	Stagnation Press. (atmospheres)	Simulated Altitude (ft)	Velocity (ft /sec)	Observed Reaction
20	2,795	0.149	150,000	12,000	Ablation
11	10,450	0.0245	250,000	25,000	Ablation
18	2,010	0.0196	200,000	10,000	Oxidation
18 A (29)	4,400	0.0260	225,000	15,000	Oxidation
18 B (30)	3,000	0.0237	220,000	12,000	Oxidation
2	8,850	0.0300	230,000	21,000	Ablation
18 C (N. P)	7,500	0.0282	240,000	19,400	Ablation
21	2,380	0.0610	200,000	12,000	Oxidation

TABLE 4.26
SUMMARY OF BERYLLIUM STEADY STATE DATA

Test Point	Heating Rate Corrected (cal/sec)	Calculated Temp (°C)	Measured Temp (°C)
18A (29)	56.4	1480	1300
21	50.2	1420	1180
18 B (30)	50.0	1425	1130
18	10.15	980	1020

TABLE 4.27
SUMMARY OF BERYLLIUM ABLATION DATA

Test No.	Test Point	Stag. Press. (atms)	Stag. Point Heat Flux (cals/sec)	Heating Rate Corrected (cals/sec)	t_m (sec)	\bar{Q}_{tm} (cals)	\bar{Q}_{rad} (cals)	\bar{Q}_m (cals)
417	11	.0245	154	130	40.8	5340	550	4790
422	11	.0204	184	161	37.1	5985	657	5330
426	2	.0300	173	142	42.0	5990	692	5300
427	2	.0303	170	140	43.0	6020	781	5240
428	2	.0273	149	118	58.0	6875	800	6075
431	--	.0282	146	115	60.8	7010	965	6045
425	11	.0209	197	175	33.7	5910	650	5260
429	2	.0273	144	114	60.0	6880	1140	5640

$$\bar{Q}_m \text{ Theory} = 1755 \text{ cals}$$

$$\bar{Q}_m \text{ Exp.} = 5460 \text{ cals} \pm 660 \text{ cals}$$

416	20	.149	162	72.3	55.5	4010	600	3410
433	20	.1525	167	76.8	33.8	2695	650	2045

$$\bar{Q}_m \text{ Theory} = 1755 \text{ cals}$$

$$\bar{Q}_m \text{ Exp.} = 2730 \text{ cals} \pm 684 \text{ cals}$$

TABLE 4.28

SUMMARY OF BERYLLIUM INITIAL MELT DATA

Test No.	Test Point	Stag. Heat Flux (cals/sec)	Heating Rate Corrected (cals/sec)	Stag. Press. (atms)	t_i (sec)	\bar{Q}_t (cals)	\bar{Q}_{rad} (cals)	\bar{Q}_{mi} (cals)
417	11	154	130	.0245	32.0	4185	567	3620
422	11	184	161	.0204	23.0	3710	285	3425
426	2	173	142	.0300	26.0	3710	392	3330
427	2	170	140	.0303	23.0	3220	241	2990
428	2	149	118	.0273	26.0	3080	284	2800
431	N.P.	146	115	.0282	36.0	4155	546	3510
425	11	197	175	.0209	19.0	3335	253	3080
429	2	144	114	.0273	32.0	3675	440	3235

$$\bar{Q}_{mi} \text{ Theory} = 1530 \text{ cals}$$

$$\bar{Q}_{mi} \text{ Exp.} = 3250 \text{ cals} \pm 222 \text{ cals}$$

416	20	162	72.3	.149	34.0	2460	600	1860
433	20	167	76.8	.1525	26.0	2000	600	1400

$$\bar{Q}_{mi} \text{ Theory} = 1530 \text{ cals}$$

$$\bar{Q}_{mi} \text{ Exp.} = 1630 \text{ cals} \pm 232 \text{ cals}$$

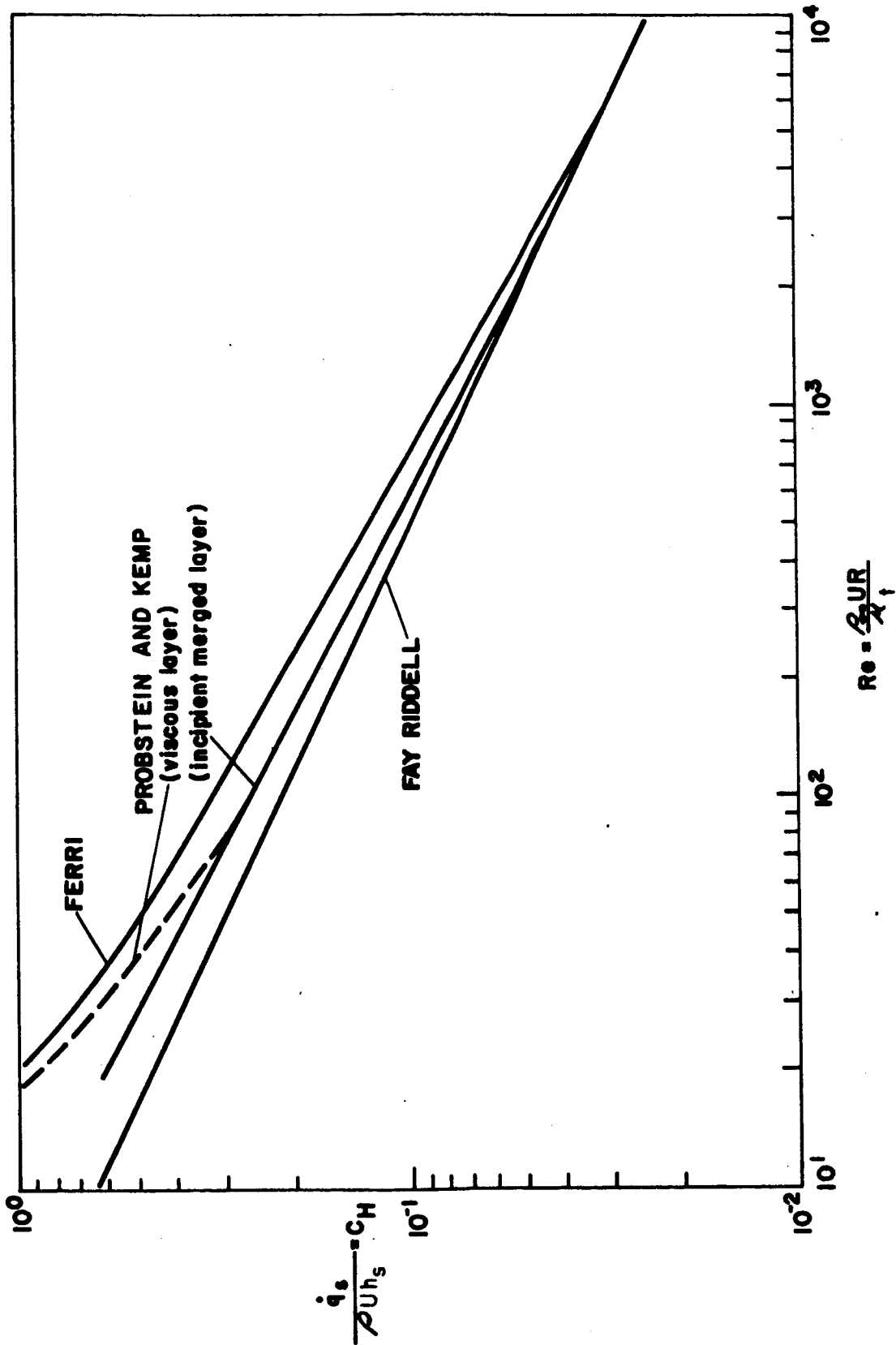


FIGURE 2.1

THEORETICAL STANTON NUMBER AS A FUNCTION OF REYNOLDS NUMBER

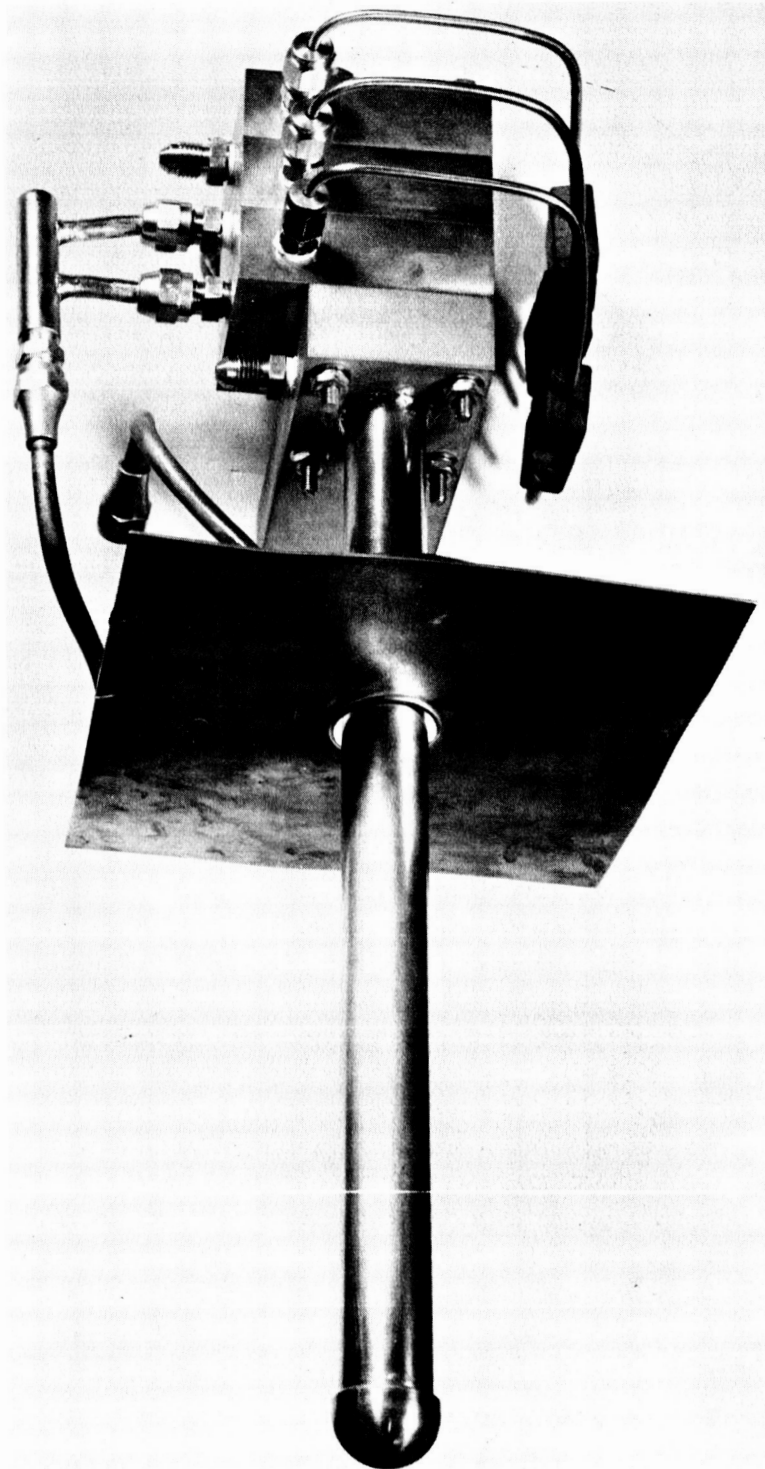


FIGURE 3.1
STAGNATION POINT HEAT FLUX PROBE

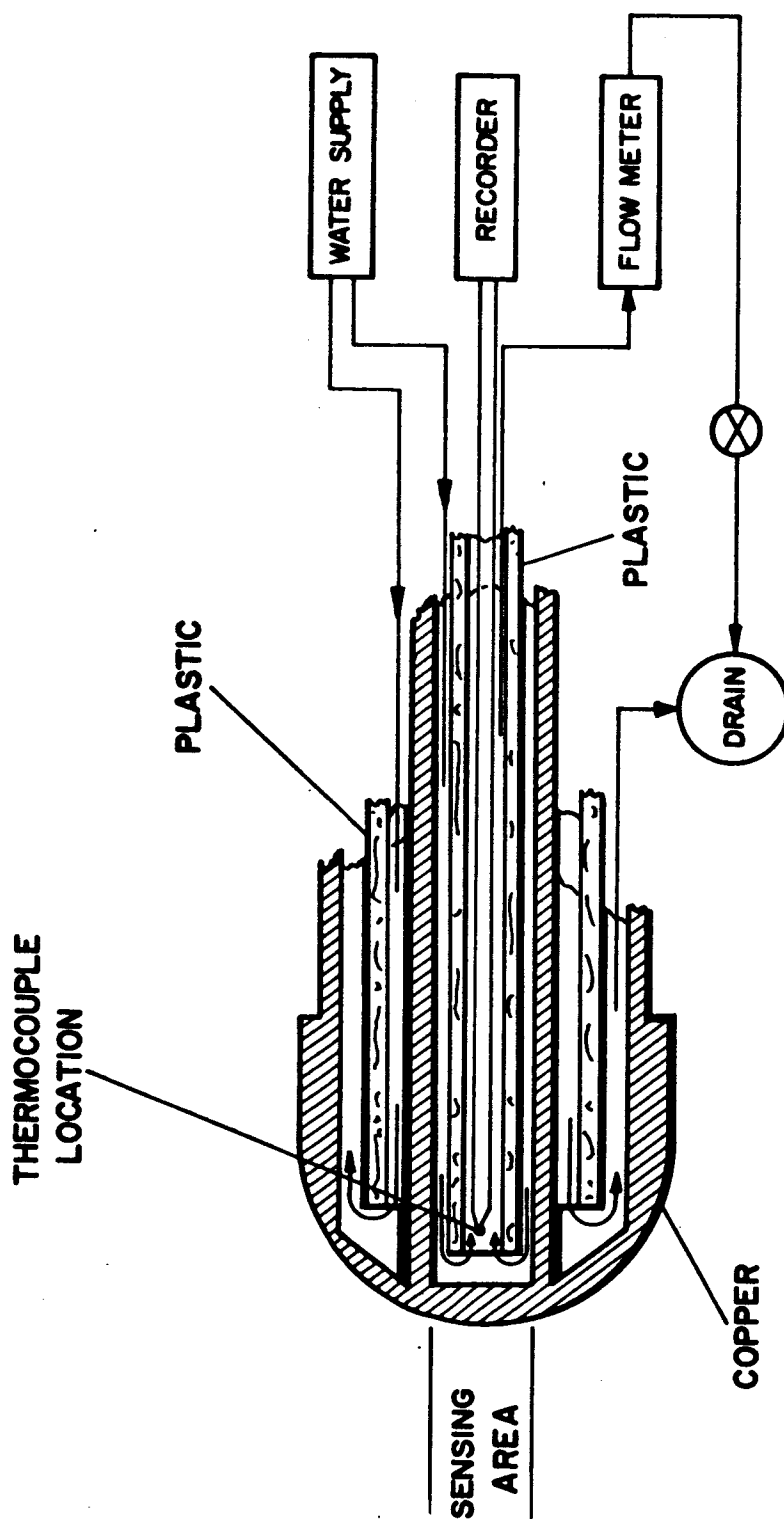


FIGURE 3.2

SCHEMATIC DIAGRAM OF STAGNATION POINT CALORIMETER PROBE

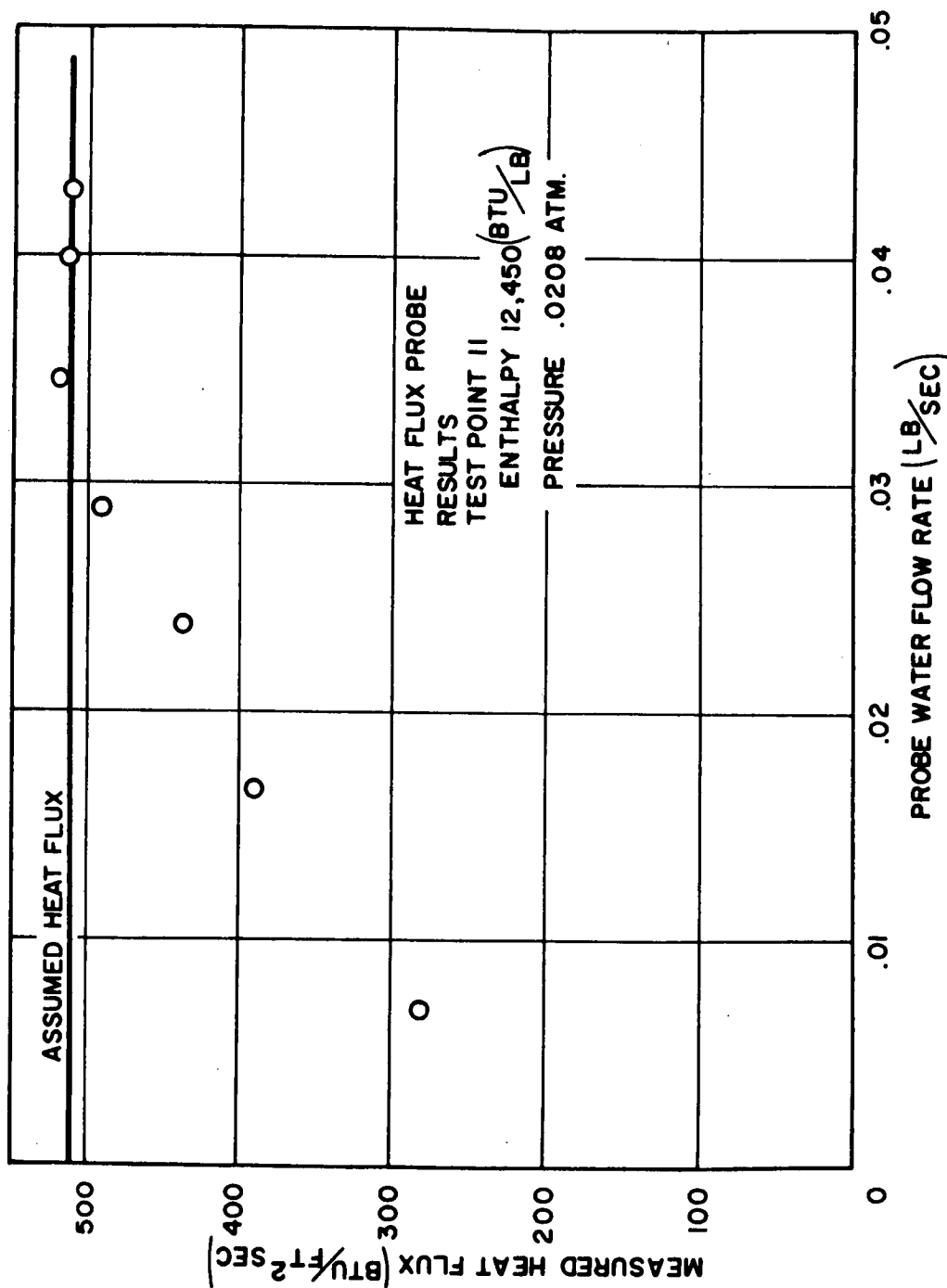


FIGURE 3.3

HEAT FLUX AS FUNCTION OF COOLANT FLOW RATE

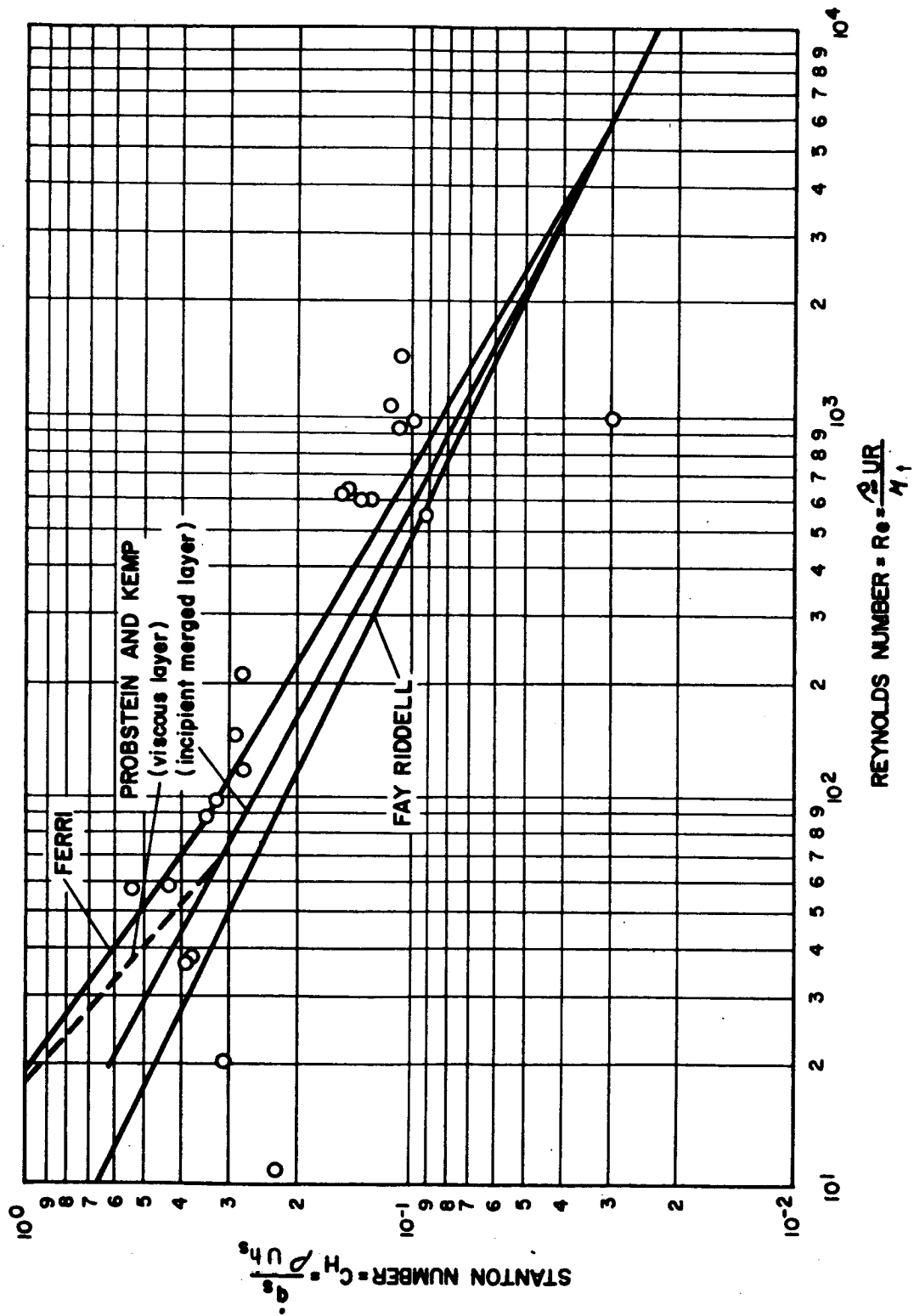


FIGURE 3.4

EXPERIMENTAL AND THEORETICAL STANTON NUMBERS AS FUNCTION OF REYNOLDS NUMBERS

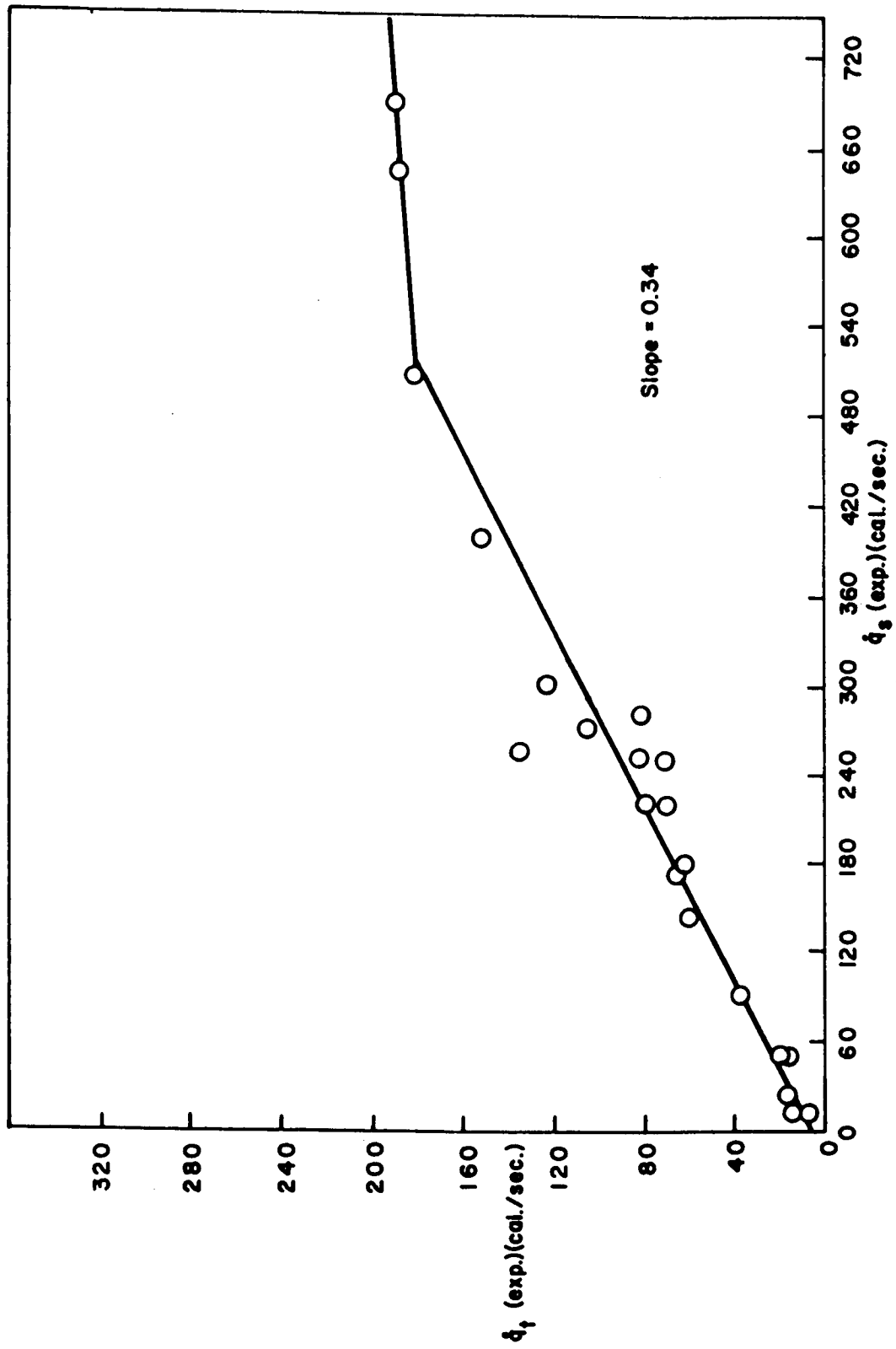


FIGURE 3.5

AVERAGE HEATING RATE AS A FUNCTION OF STAGNATION HEATING RATE

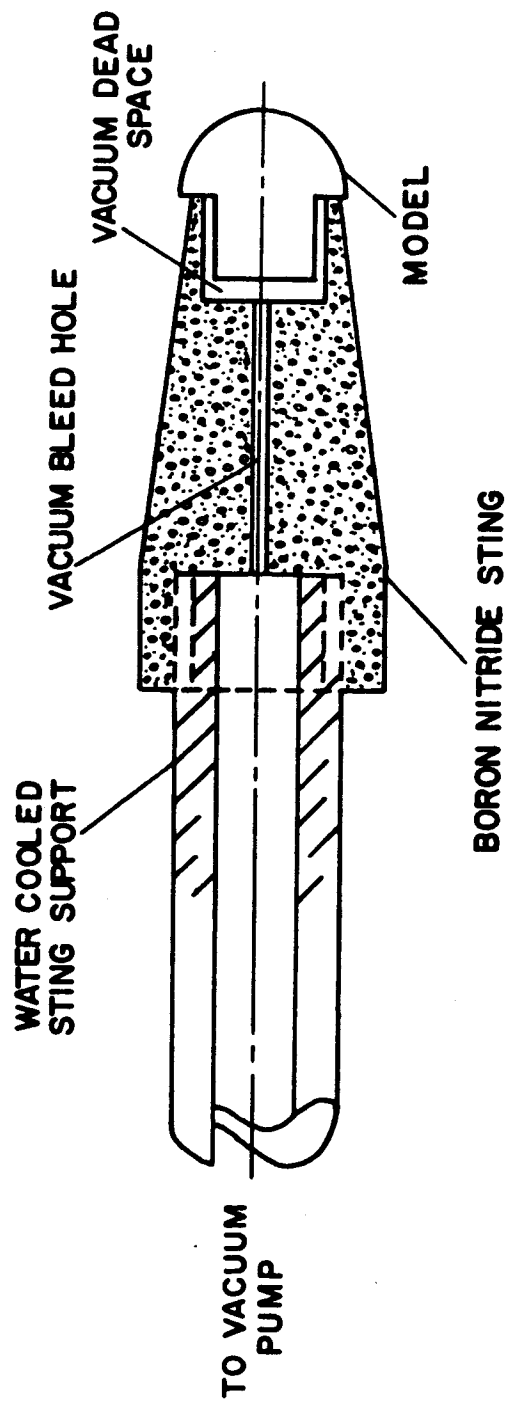


FIGURE 4.1
SUPPORT FOR MODEL IN A PLASMAJET FACILITY

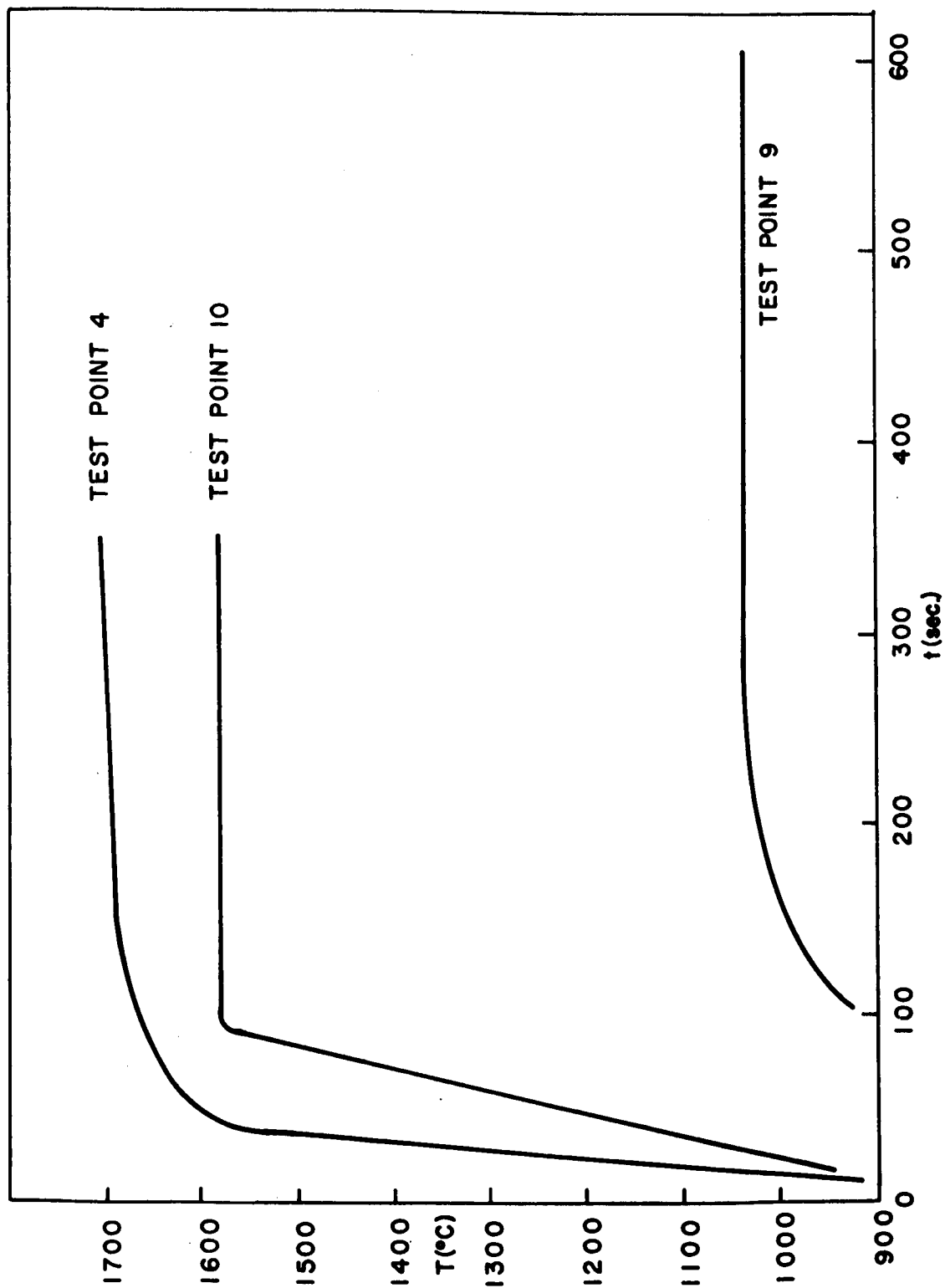


FIGURE 4.2

STEADY STATE TEMPERATURE PROFILES FOR TITANIUM SAMPLES

FIGURE 4.3

TYPICAL LINEAR OXIDATION PLOT FOR TITANIUM AT 1000°C

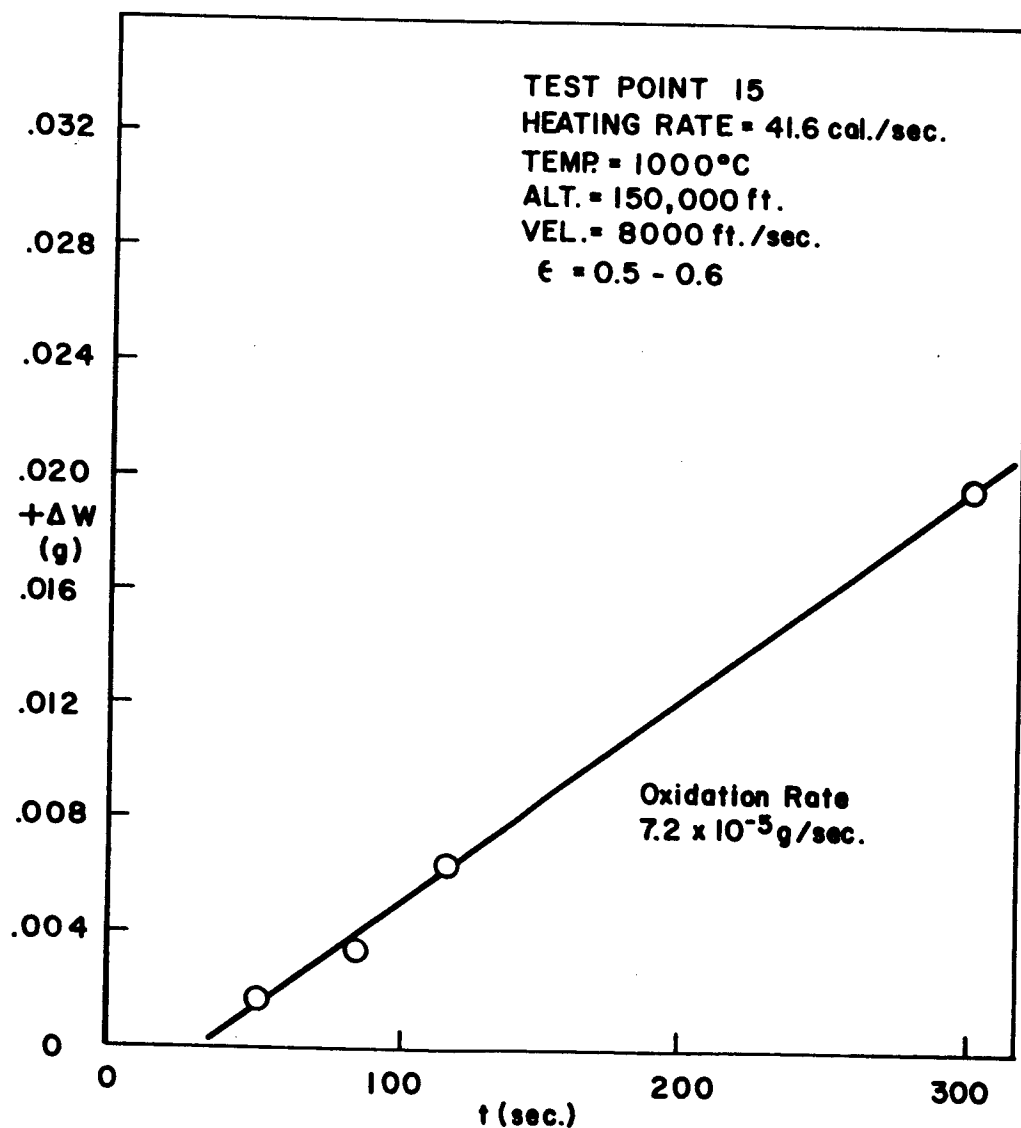


FIGURE 4.4

TYPICAL PARABOLIC OXIDATION PLOT FOR TITANIUM AT 1500°C

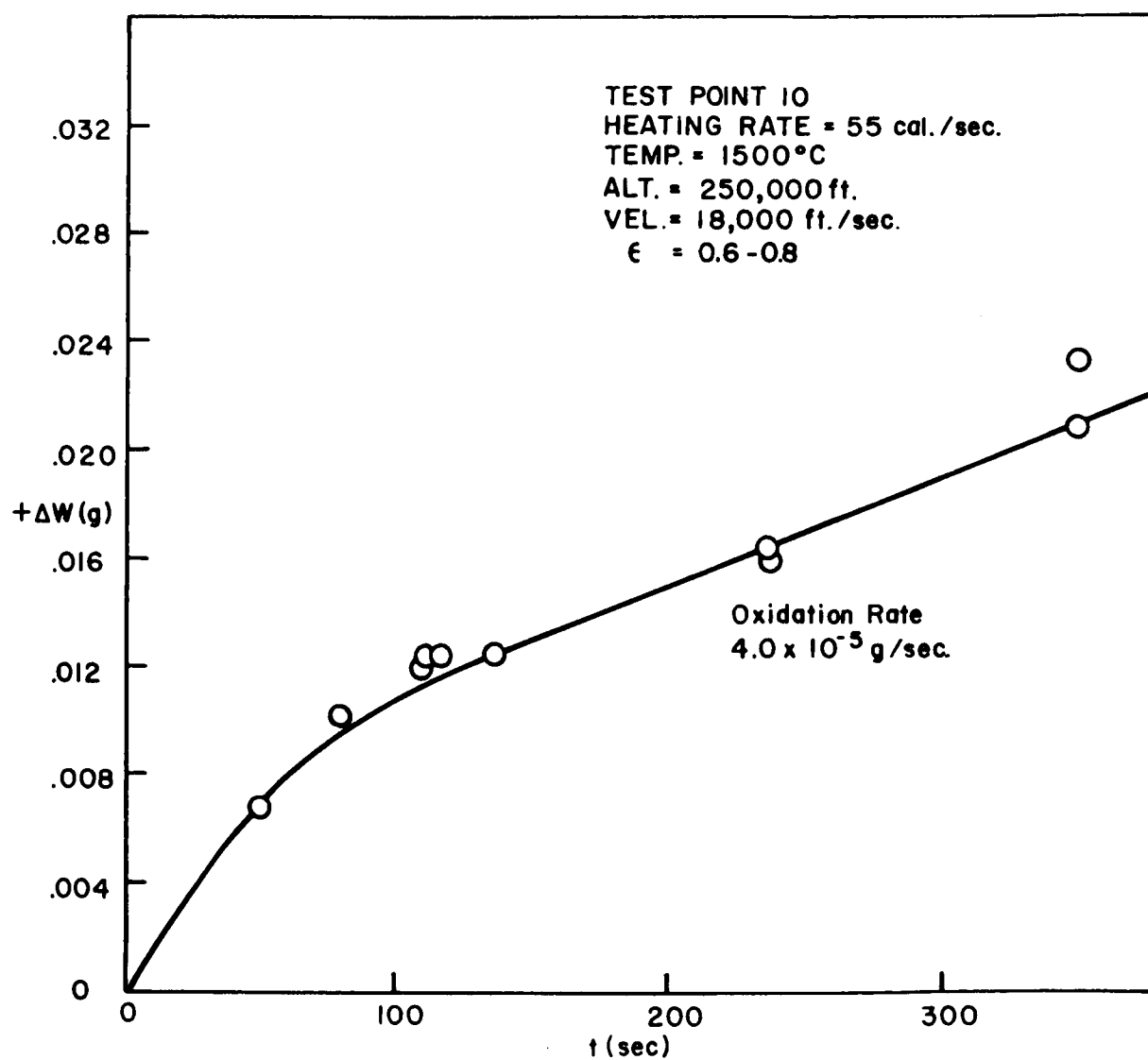


FIGURE 4.5

TYPICAL PARABOLIC OXIDATION PLOT FOR TITANIUM AT 1600°C

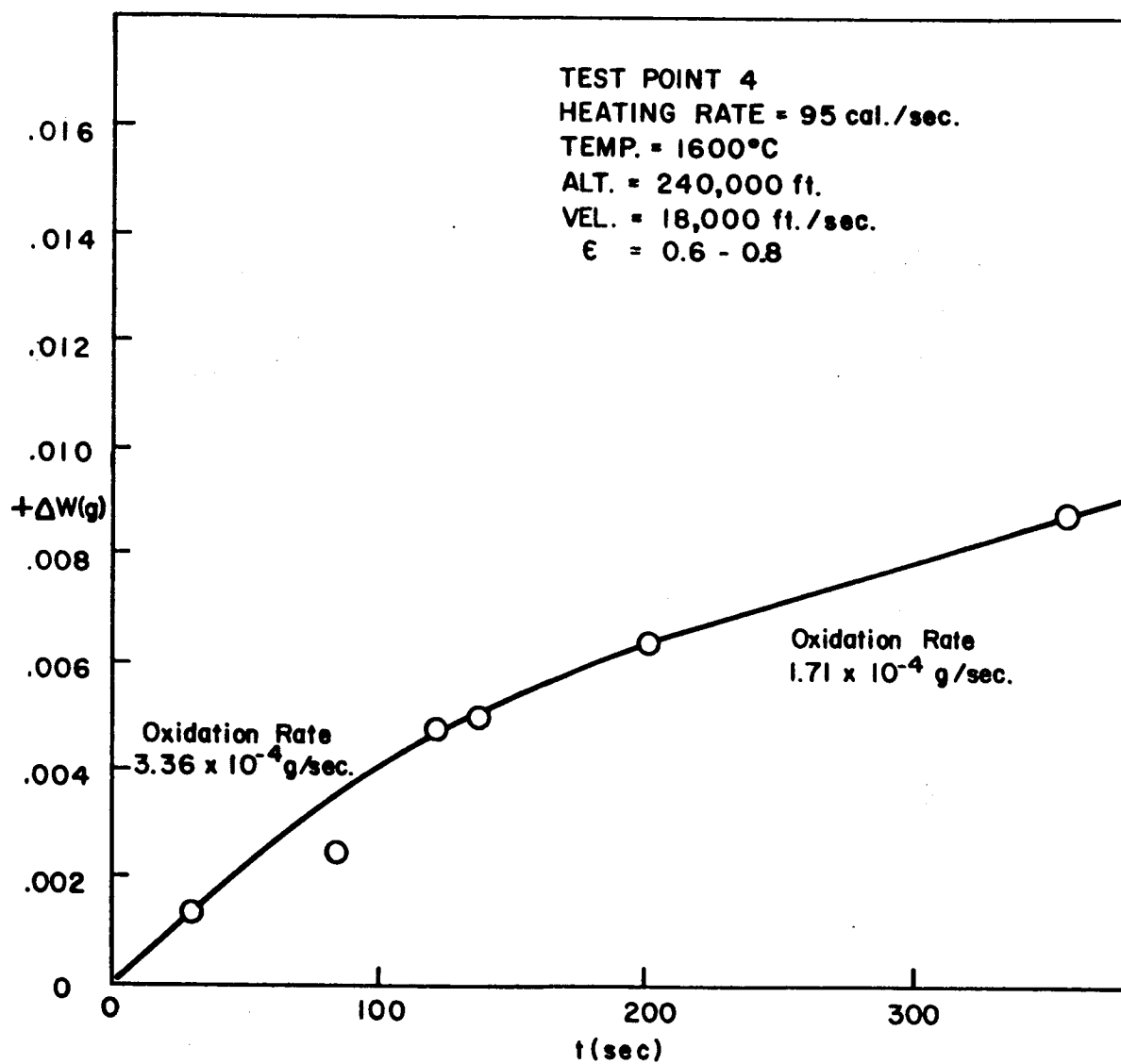


FIGURE 4.6

ABLATION SEQUENCE OF TITANIUM SAMPLES

5.85 sec.



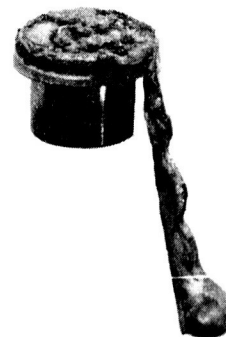
6.75 sec.



7.10 sec.



8.80 sec.



TEST POINT 5

HEATING RATE = 183.4 cal./sec.

ALTITUDE = 240,000 ft.

VELOCITY = 25,000 ft./sec.

FIGURE 4.7

FRONTAL VIEW - TEAR AWAY ABLATION SEQUENCE OF ALUMINUM SAMPLES

18sec.



20 sec.



25 sec.



33 sec.

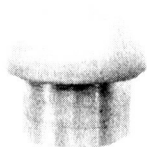


TEST POINT 15
HEATING RATE = 39 cal./sec.
ALTITUDE = 150,000 ft.
VELOCITY = 8000 ft./sec.
PRESSURE = .10 atms.

FIGURE 4.8

LATERAL VIEW - TEAR AWAY ABLATION SEQUENCE OF ALUMINUM SAMPLES

18 sec.



20 sec.



25 sec.



33 sec.



TEST POINT 15
HEATING RATE = 39 cal./sec.
ALTITUDE = 150,000 ft.
VELOCITY = 8000 ft./sec.
PRESSURE = .10 atms.

FIGURE 4.9

PARTICLES FROM TEAR AWAY ABLATION OF ALUMINUM SAMPLES



TEST POINT 15
HEATING RATE = 39 cal./sec.
ALTITUDE = 150,000 ft.
VELOCITY = 8000 ft./sec.
PRESSURE = .10 atms.

FIGURE 4.10

FRONTAL VIEW - FLOWING ABLATION SEQUENCE OF ALUMINUM SAMPLES

50 sec.



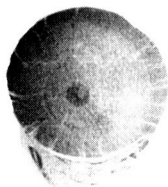
61 sec.



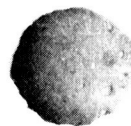
66 sec.



77 sec.



84 sec.



TEST POINT 18

HEATING RATE = 27 cal./sec.

ALTITUDE = 200,000 ft.

VELOCITY = 10,000 ft./sec.

PRESSURE = 0.008 atms.

FIGURE 4.11

LATERAL VIEW - FLOWING ABLATION SEQUENCE OF ALUMINUM SAMPLES

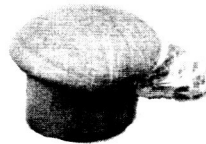
50 sec.



61 sec.



66 sec.



77 sec.



84 sec.



TEST POINT 18

HEATING RATE = 27 cal./sec.

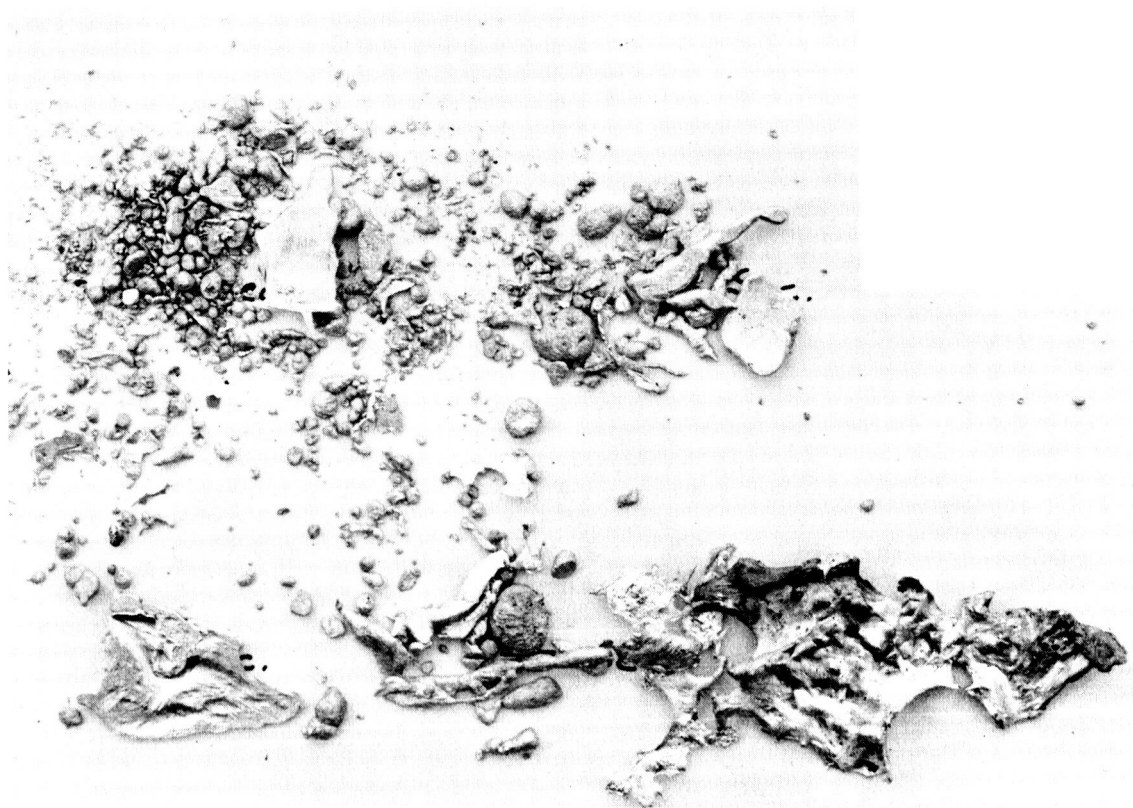
ALTITUDE = 200,000 ft.

VELOCITY = 10,000 ft./sec.

PRESSURE = 0.008 atms.

FIGURE 4. 12

PARTICLES FROM FLOWING ABLATION OF ALUMINUM SAMPLES



TEST POINT 18

HEATING RATE = 27 cal./sec.
ALTITUDE = 200,000 ft.
VELOCITY = 10,000 ft./sec.
PRESSURE = 0.008 atms.

FIGURE 4.13

PLOT OF ALUMINUM ABLATION DATA

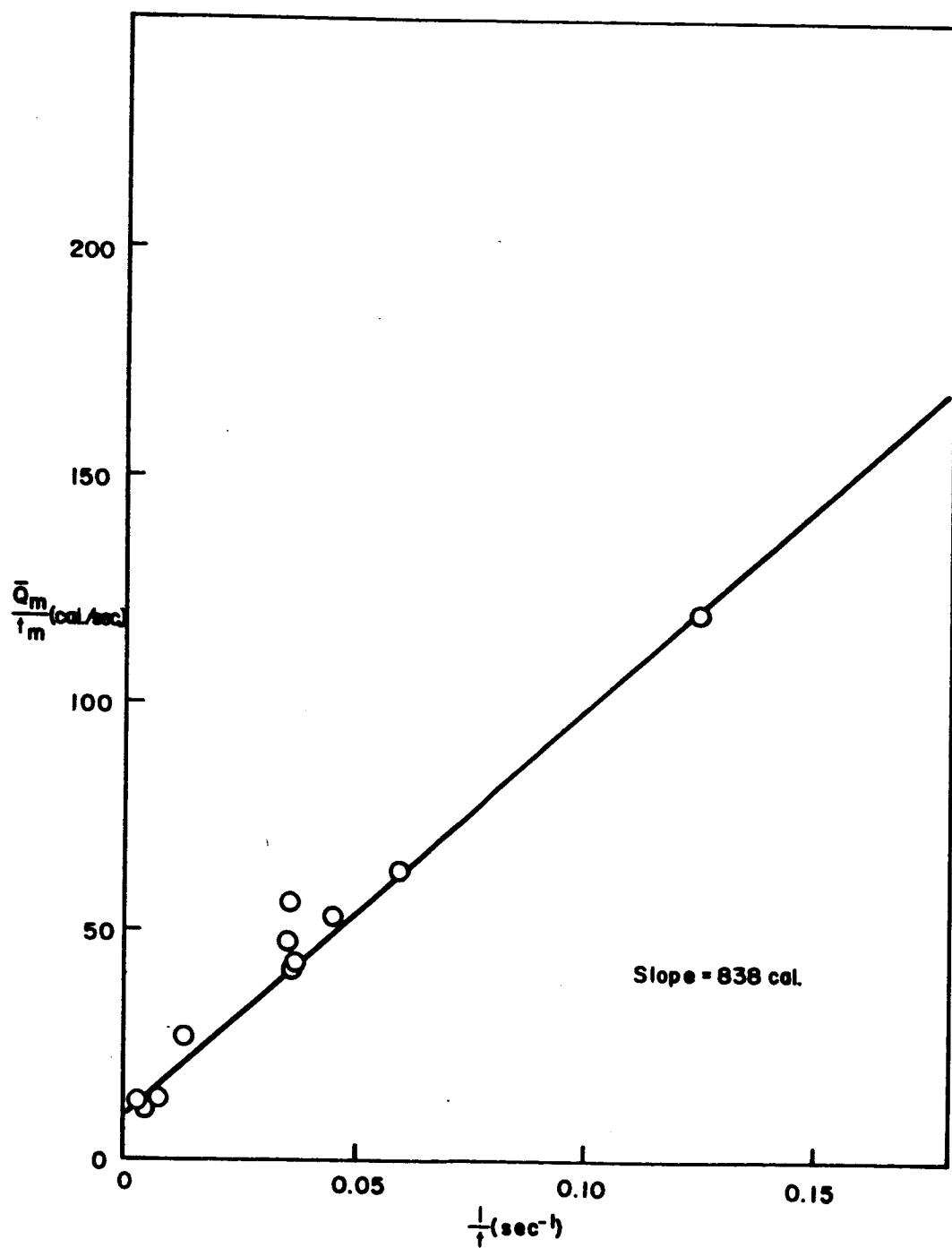


FIGURE 4. 14

PLOT OF ALUMINUM ALLOY ABLATION DATA

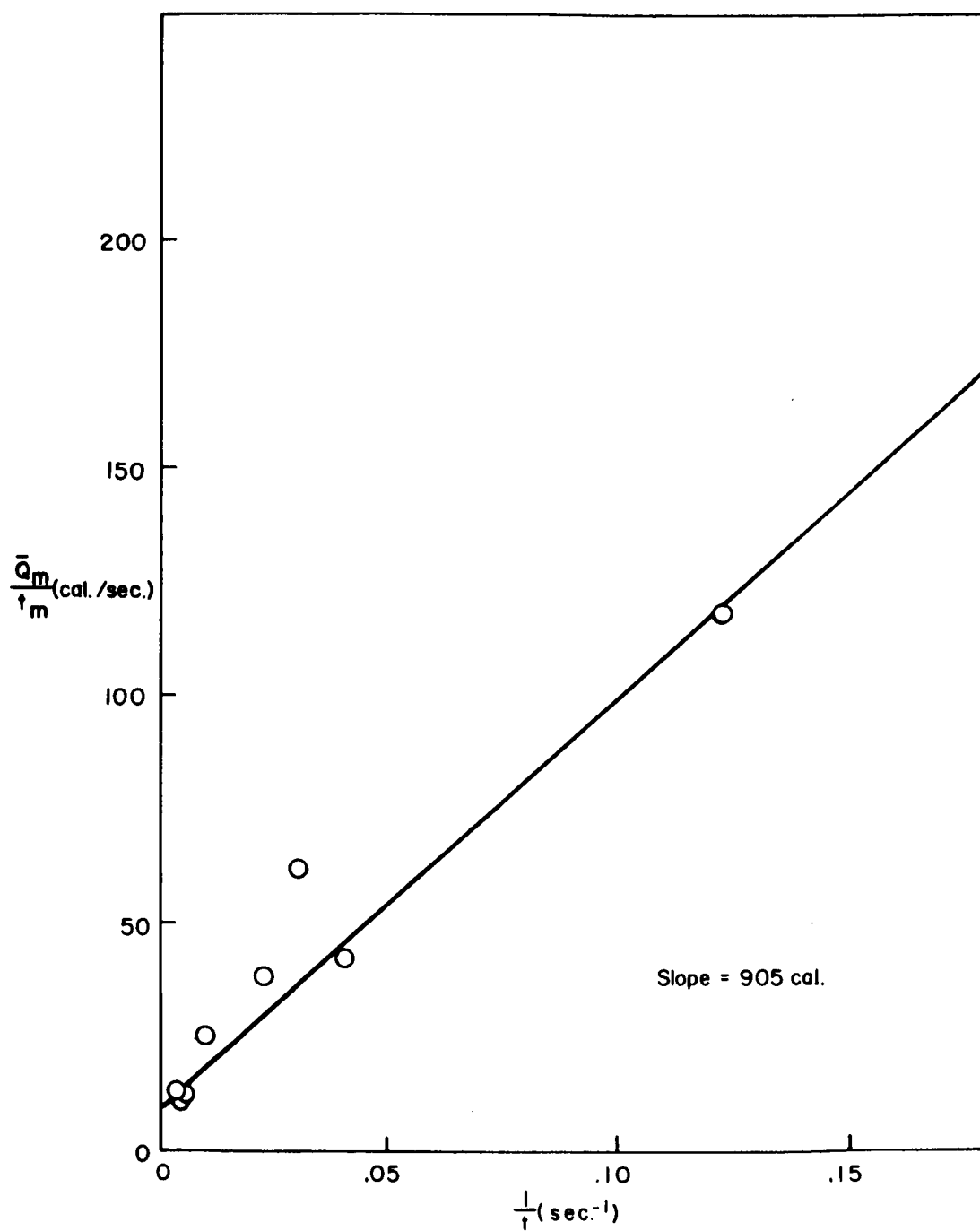


FIGURE 4.15

STEADY STATE TEMPERATURE PROFILES FOR STAINLESS STEEL SAMPLES

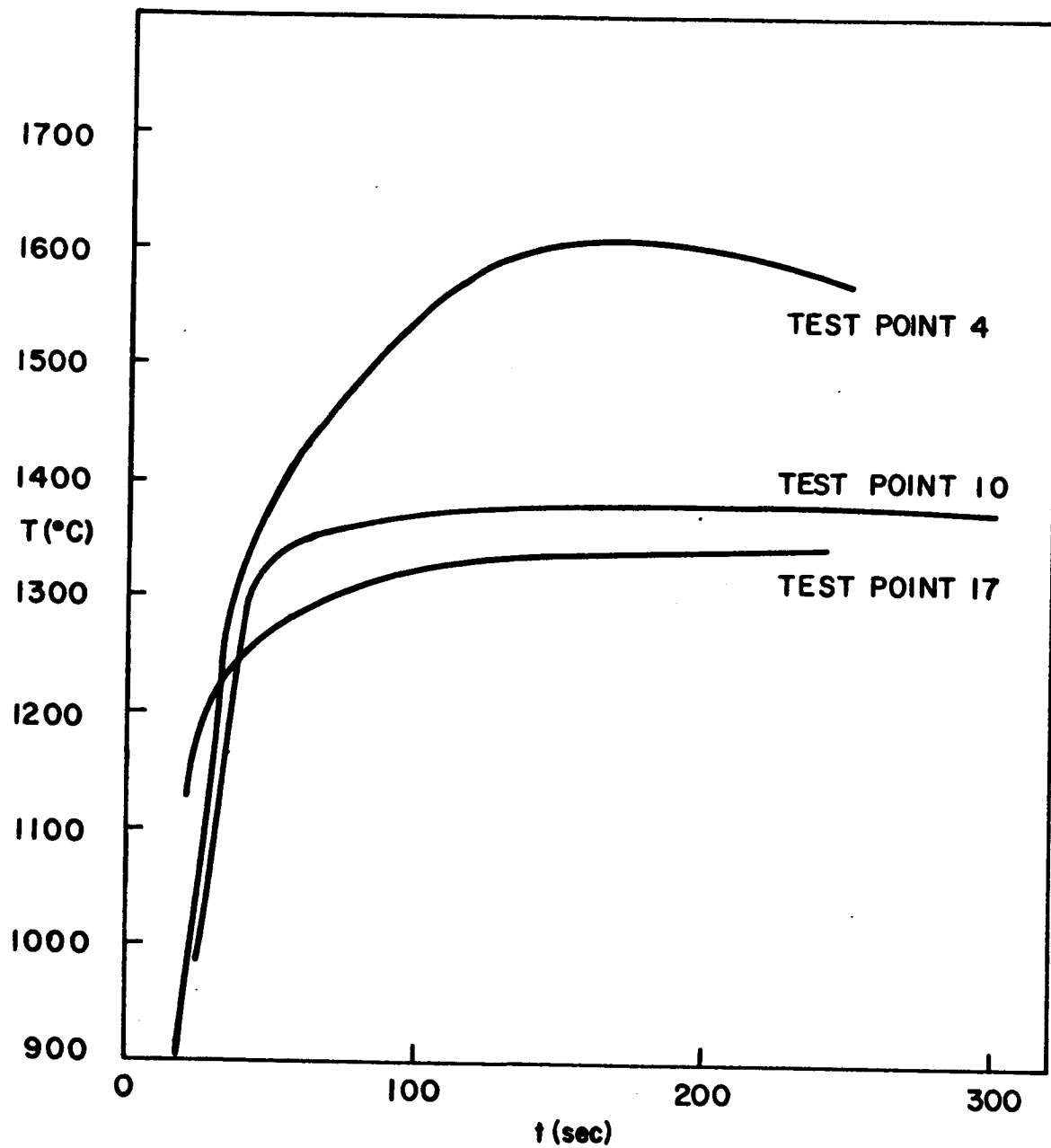


FIGURE 4.16

TYPICAL OXIDATION PLOT FOR STAINLESS STEEL AT 1300°C

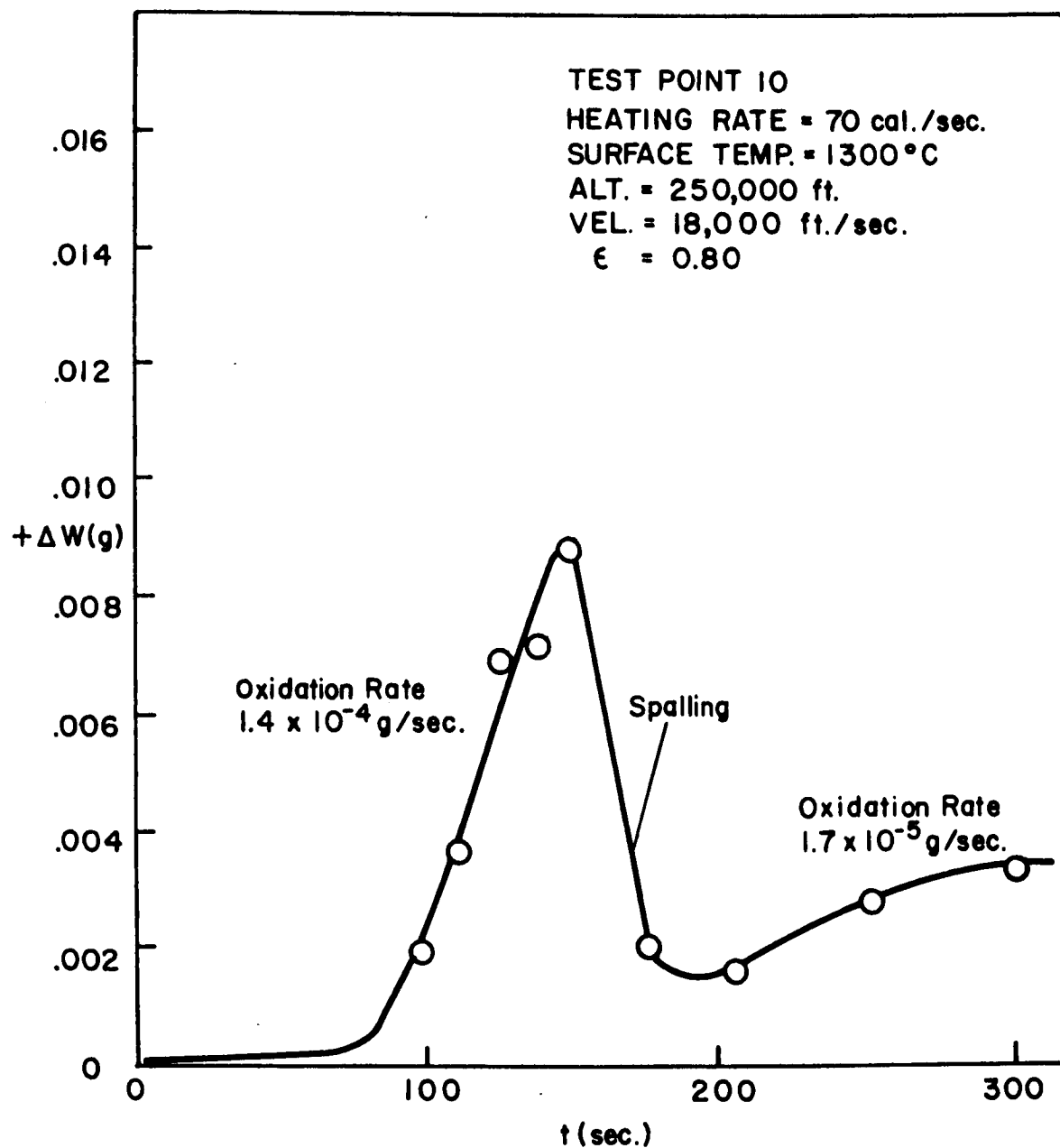


FIGURE 4.17
TYPICAL OXIDATION PLOT FOR STAINLESS STEEL AT 1400°C

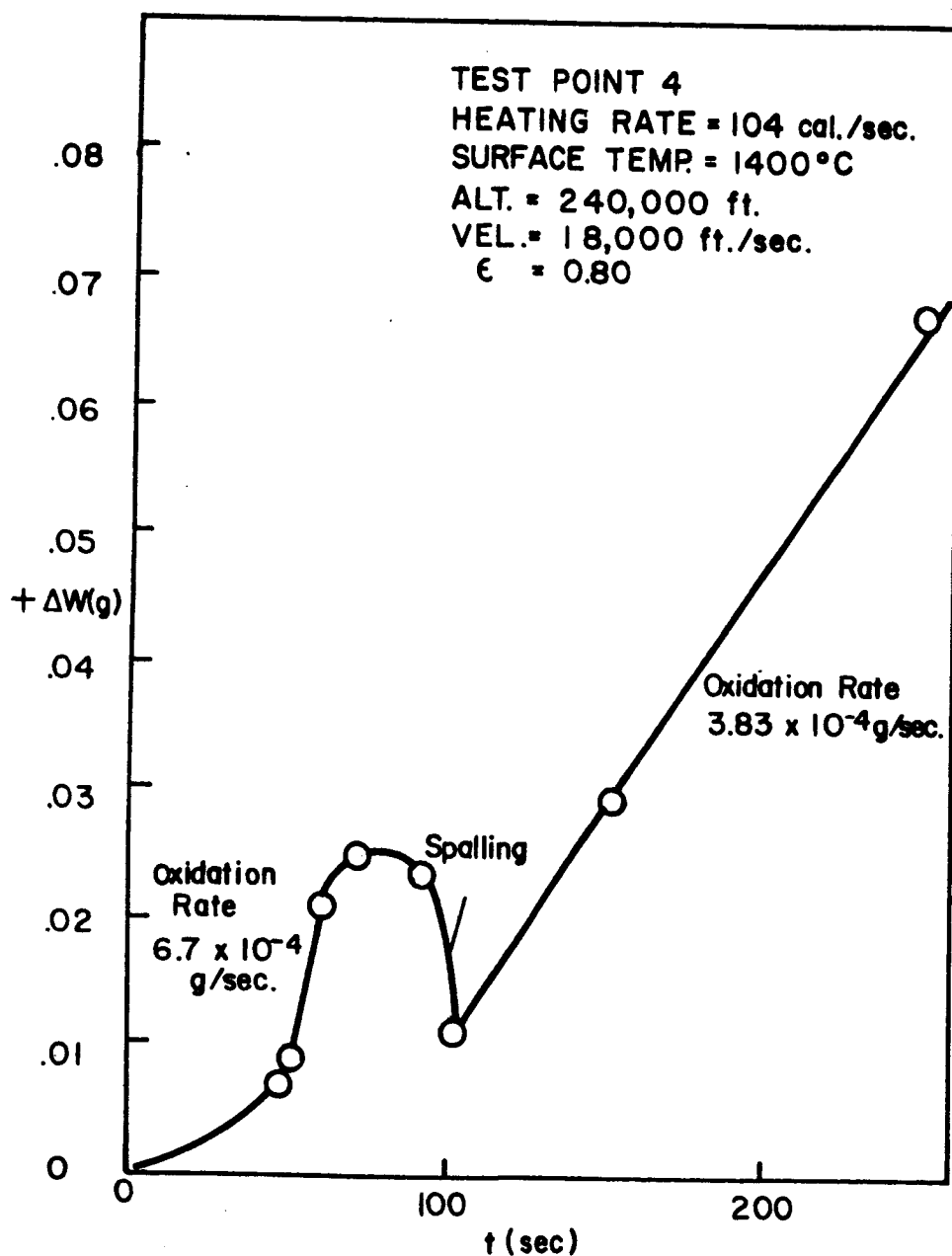
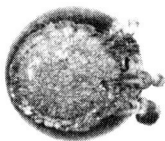


FIGURE 4. 18

FRONTAL VIEW - COMPLETE ABLATION OF STAINLESS STEEL SAMPLES

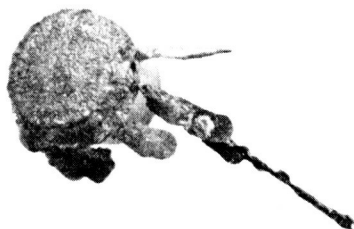
23 sec.



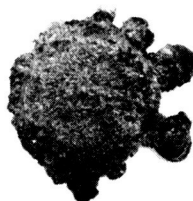
27 sec.



30 sec.



31 sec.



TEST POINT 20

HEATING RATE = 122 cal./sec.

ALTITUDE = 150,000 ft.

VELOCITY = 12,000 ft./sec.

FIGURE 4.19

LATERAL VIEW - COMPLETE ABLATION OF STAINLESS STEEL SAMPLES

23 sec.



27 sec.



30 sec.



31 sec.

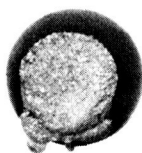


TEST POINT 20
HEATING RATE = 122 cal./sec.
ALTITUDE = 150,000 ft.
VELOCITY = 12,000 ft./sec.

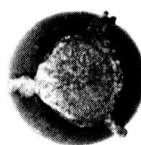
FIGURE 4.20

FRONTAL VIEW - INCOMPLETE ABLATION OF STAINLESS STEEL SAMPLES

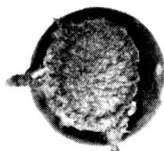
13 sec.



21 sec.



32 sec.



TEST POINT 17

HEATING RATE = 102 cal./sec.
ALTITUDE = 150,000 ft.
VELOCITY = 10,000 ft./sec.

FIGURE 4.21

LATERAL VIEW - INCOMPLETE ABLATION OF STAINLESS STEEL SAMPLES

13 sec.



21 sec.



32 sec.



TEST POINT 17

HEATING RATE = 102 cal./sec.
ALTITUDE = 150,000 ft.
VELOCITY = 10,000 ft./sec.

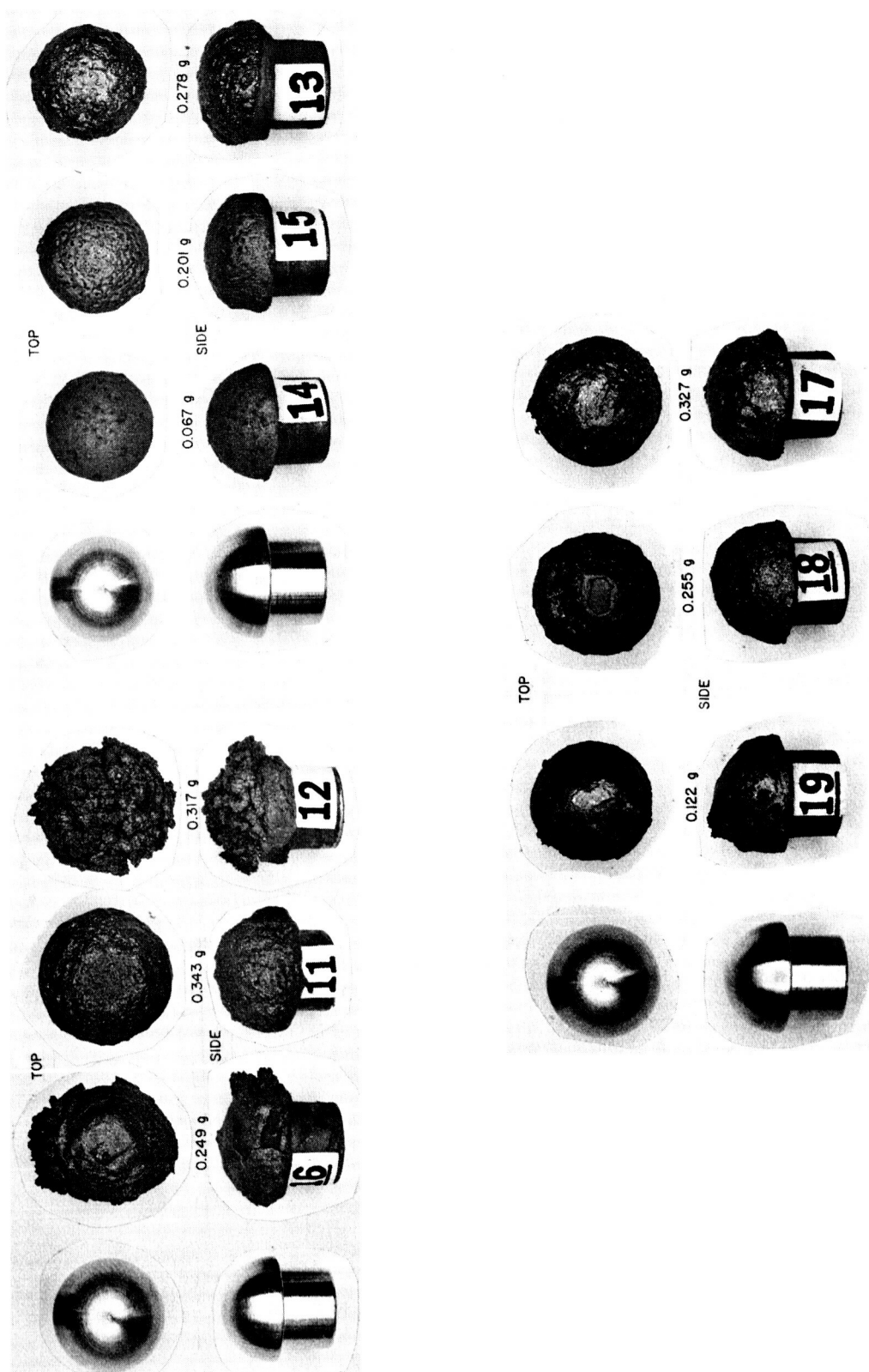
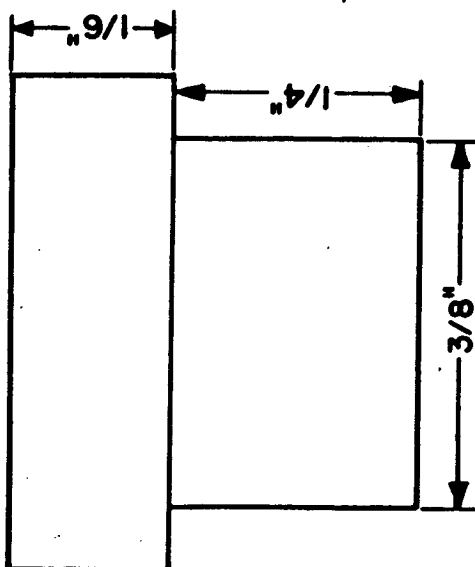


FIGURE 4.22
TYPE OF OXIDES FORMED ON STAINLESS STEEL SAMPLES

1/2" CYLINDER



1/2" HEMISPHERE

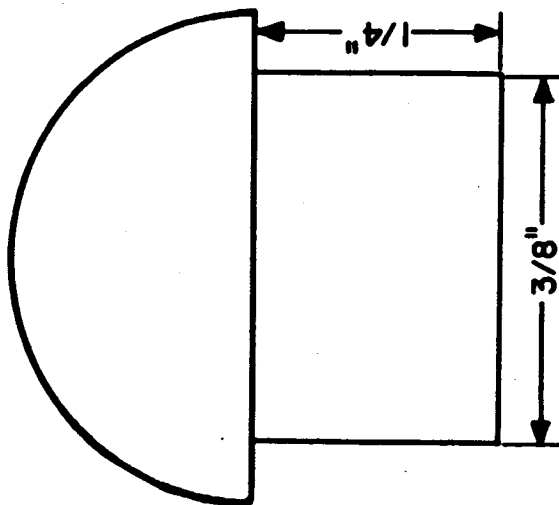


FIGURE 4.23
SCHEMATIC DIAGRAM OF SAMPLES OF VARIABLE GEOMETRY

FIGURE 4.24

STEADY STATE TEMPERATURE PROFILES FOR INCONEL SAMPLES

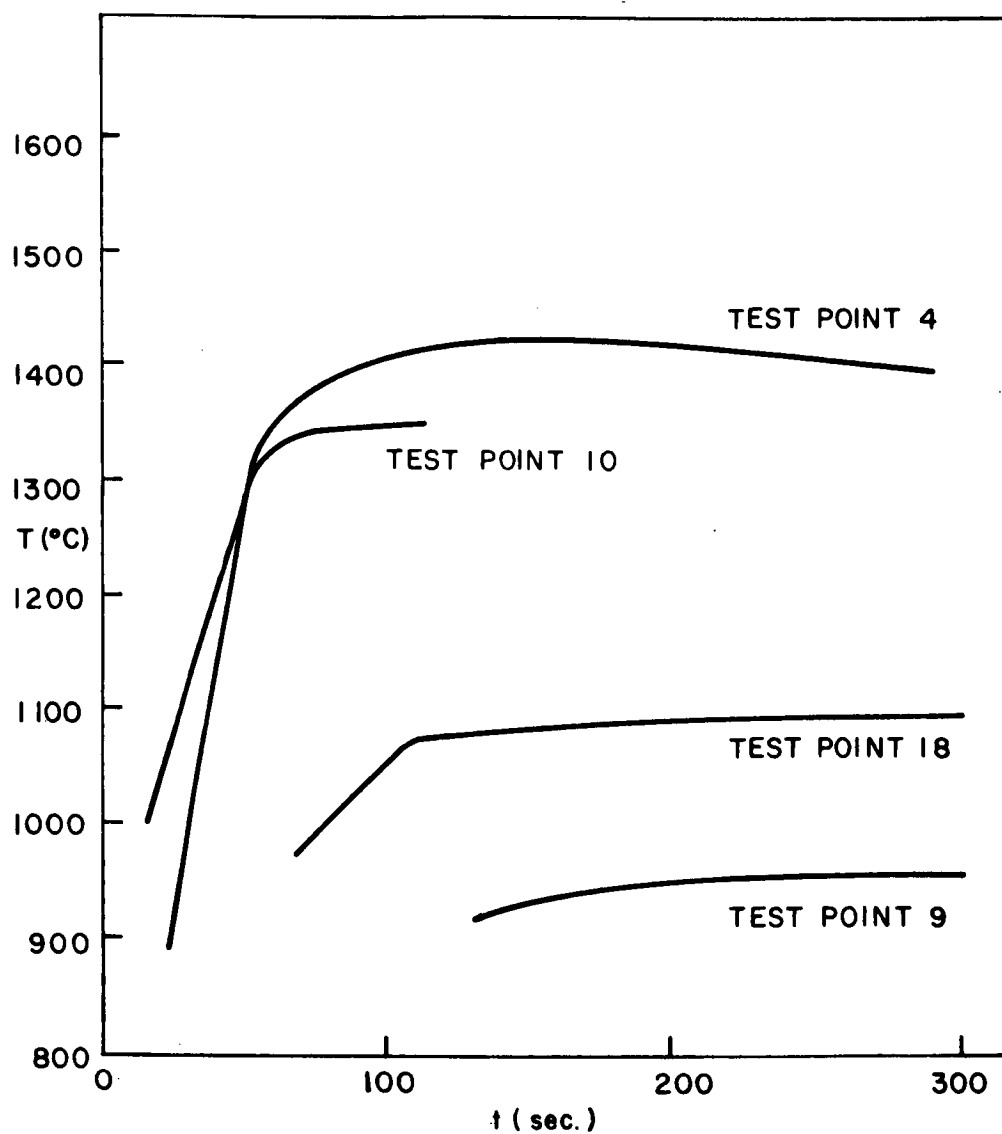


FIGURE 4. 25

TYPICAL OXIDATION PLOT FOR INCONEL AT 1350°C

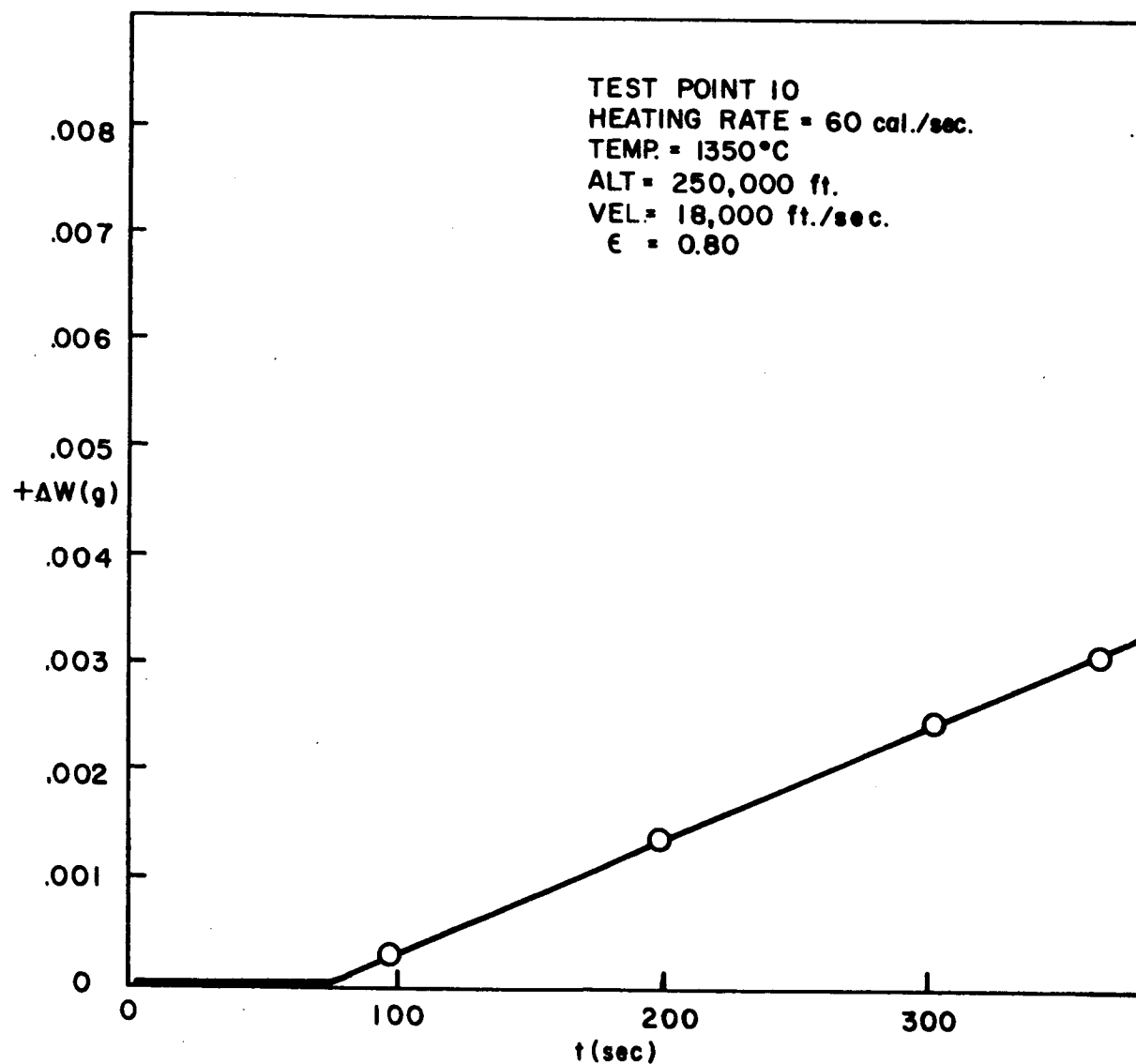
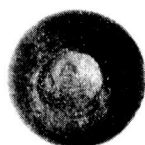


FIGURE 4.26

FRONTAL VIEW - COMPLETE ABLATION OF INCONEL SAMPLES

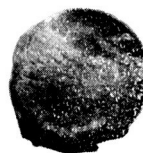
10 sec.



12.3 sec.



14.5 sec.



16 sec.



18.5 sec.



TEST POINT 2

HEATING RATE = 167 cal./sec.

ALTITUDE = 230,000 ft.

VELOCITY = 21,000 ft./sec.

FIGURE 4.27

LATERAL VIEW - COMPLETE ABLATION OF INCONEL SAMPLES

10 sec.



12.3 sec.



14.5 sec.



16 sec.



18.5 sec.



TEST POINT 2

HEATING RATE = 167 cal./sec.

ALTITUDE = 230,000 ft.

VELOCITY = 21,000 ft./sec.

FIGURE 4.28

FRONTAL VIEW - INCOMPLETE ABLATION OF INCONEL SAMPLES

92 sec.



122 sec.



182 sec.



302 sec.



TEST POINT 17
HEATING RATE = 96.3 cal./sec.
ALTITUDE = 150,000 ft.
VELOCITY = 10,000 ft./sec.

FIGURE 4.29

LATERAL VIEW - INCOMPLETE ABLATION OF INCONEL SAMPLES

92 sec.



122 sec.



182 sec.



302 sec.



TEST POINT 17

HEATING RATE = 96.3 cal./sec.

ALTITUDE = 150,000 ft.

VELOCITY = 10,000 ft./sec.

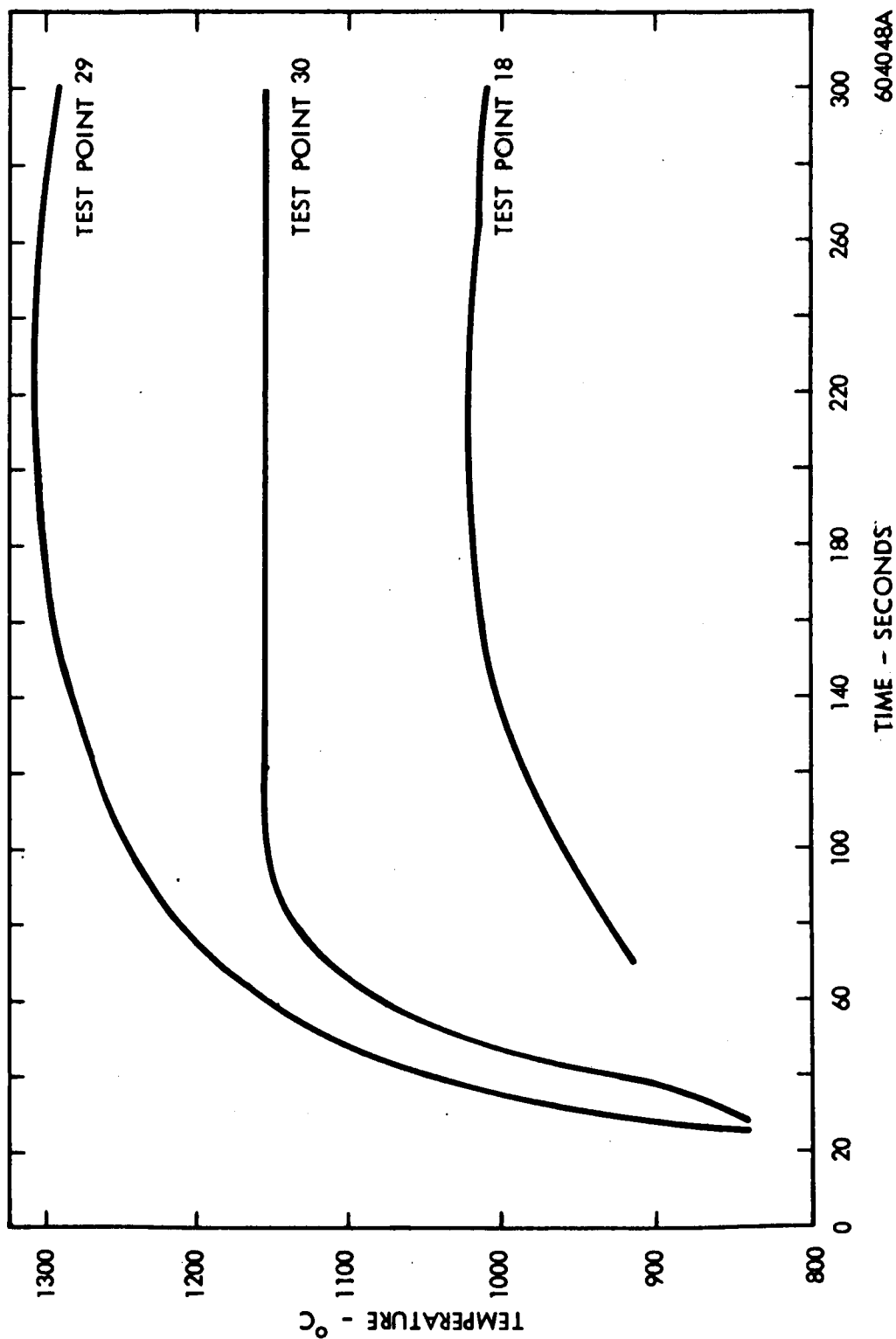


FIGURE 4.30
STEADY STATE TEMPERATURE PROFILE FOR BERYLLIUM SAMPLES

FIGURE 4.31
FRONTAL VIEW-ABLATION SEQUENCE OF BERYLLIUM SAMPLES



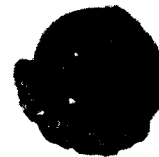
Be I
34.00 sec.



39.65 sec.



44.95 sec.



71.00 sec.

TEST POINT 20
HEATING RATE = 73.2 cal./sec.
ALTITUDE = 150,000 ft.
VELOCITY = 12,000 ft./sec.
PRESSURE = 0.1490 atms.

FIGURE 4.32
LATERAL VIEW-ABLATION SEQUENCE OF BERYLLIUM SAMPLES



Be I
34.00 sec.



39.65 sec.



44.95 sec.



71.00 sec.

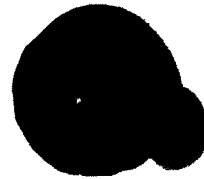
TEST POINT 20

HEATING RATE	= 73.2 cal./sec.
ALTITUDE	= 150,000 ft.
VELOCITY	= 12,000 ft./sec.
PRESSURE	= 0.1490 atms.

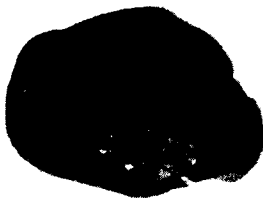
FIGURE 4.33
FRONTAL VIEW-ABLATION SEQUENCE OF BERYLLIUM SAMPLES



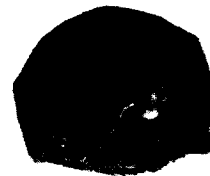
Be 19
18.90 sec.



27.45 sec.



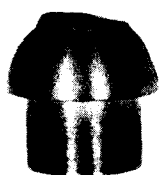
39.30 sec.



40.65 sec.

TEST POINT II
HEATING RATE = 175.3 cal./sec.
ALTITUDE = 250,000 ft.
VELOCITY = 25,000 ft./sec.
PRESSURE = 0.0209 atms.

FIGURE 4.34
LATERAL VIEW-ABLATION SEQUENCE OF BERYLLIUM SAMPLES



Be 19
18.90 sec.



27.45 sec.



39.30 sec.



40.65 sec.

TEST POINT II
HEATING RATE = 175.3 cal./sec.
ALTITUDE = 250,000 ft.
VELOCITY = 25,000 ft./sec.
PRESSURE = 0.0209 atms.

FIGURE 4.35
PLOT OF BERYLLIUM ABLATION DATA

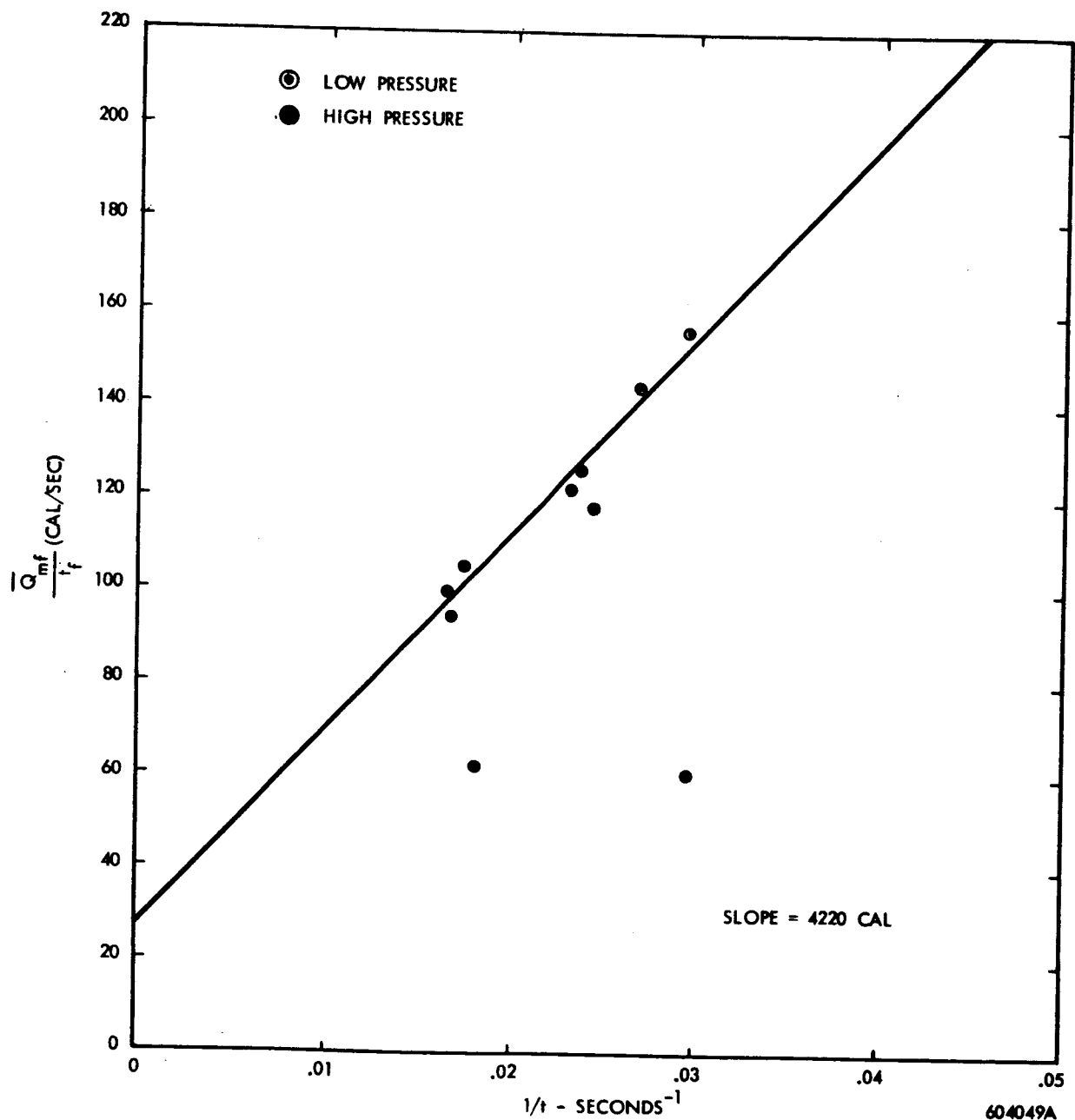


FIGURE 4.36
 PLOT OF INITIAL MELT DATA OF BERYLLIUM SAMPLES

